Title
Experimental Investigation of silicon metal-oxide-semiconductor based triple quantum dot

Author
Pan, Hong

Publication Date
2013

University of California
Los Angeles

Experimental Investigation of Silicon metal-oxide-semiconductor based Triple Quantum Dot

A dissertation submitted in partial satisfaction
of the requirements for the degree
Doctor of Philosophy in Physics

by

Hong Pan

2013

Abstract of the Dissertation

Experimental Investigation of Silicon metal-oxide-semiconductor based Triple Quantum Dot

by

Hong Pan

Doctor of Philosophy in Physics
University of California, Los Angeles, 2013
Professor Hong Wen Jiang, Chair

With the rapid progress in nanofabrication, scientists and researchers are now able to make lateral quantum dots in semiconductor materials. The few electrons confined in these quantum dots provide the possibility of realizing a qubit, the building block of a quantum computer. Tremendous effort has been put in the solid state quantum information field in the last ten years of making single electron spin qubit or singlet triplet qubit based on two electron spin. However, the operation of these types of qubit requires additional engineering by either integrating a microwave loop or an external magnet to creat field difference. This thesis project was inspired by DiVincenzo's proposal of developing qubit based on three electrons controlled by Heisenberg exchange interactions only, which is called "exchange-only" qubit. All the qubit operation can be done in principle via electrical pulses only. We proposed to make the triple quantum device in silicon system. This type of device will have small qubit decoherence, easy integration to industry infrustructure and great chance of scaling up to a real quantum computer. We developed and fabricated the electrostatically defined triple quantum dot (TQD) device in a silicon metal-oxide-oxide structure. We characterized its electrostatic properties using a quantum point contact charge sensing channel nearby. We are be able to obtain the charge stability diagram in the last few elelctron regime that provides the experimental basis of forming a exchange only qubit. We demonstrated the tunability of the TQD by acheiving the quadruple points where all three dots are on resonance. This is the first experimental demonstration of well controlled triple quantum dot device in silicon system. The constant interaction model and the hubbard model for triple quantum dot system are developed to help understand the electrostatic dynamics. Tunnel coupling t_c between quantum dots, which determines the exchange interactions, are extracted using various fitting methods. We implemented the qubit manipulation with three quantum dots in both a linearly and a triangularly arranged geometry. For the first time, we observed coherent oscillation in the Si MOS based triple quantum dot device with oscillation frequency of 2MHz and 7MHz. We suspect the these oscillations are related with spin dynamics in our system. These experimental investigations demonstrate that we have the ability to develop triple quantum dot device for exchange ony qubit and the potential to perform qubit operation in the future.

The dissertation of Hong Pan is approved.

Kang Wang

Karoly Holczer

Stuart Brown

Hong Wen Jiang, Committee Chair

University of California, Los Angeles
2013

For my mother and father

Table of Contents

List of Figures

ACKNOWLEDGMENTS

> *"Thus, when Heaven is about to confer a great office on any man, it first exercises his mind with suffering, and his sinews and bones with toil. It exposes his body to hunger, and subjects him to extreme poverty. It confounds his undertakings. By all these methods it stimulates his minds, hardens his nature, and supplies his incompentencies. "*
>
> -Mencius

It is really a long journey before I can sit down and summarize all my work for the past six years. The past memories suddenly revive and all the feelings: frustration, lost, enjoyment, grateful rush into my mind. I cannot imagine to have this thesis done without the help from all the people I met during my Ph.D. And I cannot express how appreciated I am to these wonderful people.

I still remember the earlier days when I first joined Prof. Hongwen Jiang's lab. I was a typical student with my mind stuffed with equations and principles while all most no hands on experience at all. It was Prof. Jiang who guided me to the world of solid state physics and showed me how fantastic the low dimentional physics is. He is such a great presentor who always comes with a vivid picture when explaining the physics behind. The α and β are no longer coefficient but rather something happening in the real world. His passion and focus of experimental research constantly inspire me especially during the most frusntration period. As a mentor, he not only teaches me how to do scientific research but also shares his understanding and experience about work and life. This is certainly a gift to me for my whole life time. Eventhough I didn't work hard enough and ocassionally behaviored very childish, he always forgave me and encouraged me to walk forward.

And I want to thank him for his unlimit support in instruments, more and more expensive helium, providing a dreaming environment for a low temperature experimental physics students, not to mention his daily "meeting" that stimulats lots of great experimental ideas and pulls me back from the wrong track from time to time. Even though I will work in a completely different field, I will always miss the old days and our afternoon chat about history, development and ”just be oneself”.

I am glad to have Dr. Xiaojie Hao join the lab when I started my thesis research. Without him, the progress of this thesis would be greatly delayed and I probably have to spend another year to accomplish the work I’ve already done. I thank him for being always helpful. ”Ask xiaojie” now becomes the first thing flashes in every labmember’s mind whenever we come across problems. And I enjoy all the stimulating talks with him about silicon quantum dot fabrication, spin qubit physics and developement in quantum information field. In the last two years, we experienced lots of difficult in our research like unknow problems, broken equipment and competetion from other groups. I really appreciate to have him as a senior member and overcome the frustration together.

Part of the research in Chapter 3 is done in collabration with former graduate student Matthew House. Matt is such a nice guy and taught me lots of knowledge about English and American life. He is also a wonderful collabrator. We had a productive summer working on the double dot project and from that time I started to get the feeling of experimental investigation about Si MOS quantum dot. Last I want to thank him for letting me do some unrelevant experiment in his device. Now after fabricationg several hundreds of devices myself, I realize how selflessness and brave he was. I wish him all the best in Australia. Some of the theoretical work in this thesis won’t be accomplished without the help from my collegemate, Dr. Chengjie Wang. Thanks for being patient with my silly questions and providing thorough interpretations. Some work in Chapter 6 is with guidance from Dr. Rusko Ruskov. I thank him for his ”Russian Style” accurate and strict. It was my pleasure to work with two undergraduate students: Guan Zixuan and Gan Tian. We worked together on the constant interaction model and had lots of fun. I wish them all the best.

Other lab members all play important role. Without Dr. Ming Xiao, who developed the fabrication recipe of Si MOS based quantum dot, this thesis would not even exist. And the new comers, Blake and Josh, bring lots of fresh air to the lab. It has really been a nice period in the past six years. It won’t be possible without all the wonderful people in the department. It is so nice to hve hardworking professors say Hi on Sunday Afternoon in the basement of Physics building. All the staff member, Jenny, Vidia, Carol, Craig,Cecile, Ernesto, Sherin and so many others always try to minimize the admistration process and make our life much easier. I thank all of them for their professionalism.

Last, I want to thank my parents for their unlimit support, for their respect of all my choices, for their trust in me, for their being such great person. It is their positive attitude about work, their philosophy about life that encourage me to clime across all the mountains and move forward. Without them, I won't accomplish what I have done. Without them, I won't become the person who I am.

VITA

2006–2007	Research Assistant University of Science and Technology of China Hefei, Anhui, China
2006.07-2006.09	Research Assistant Institute of Physics, Chinese Academy of Sciences Beijing, China
2007	B.S. in Applied Physics University of Science and Technology of China
2008–2013	Teaching Assistant UCLA Department of Physics and Astronomy
2008–2013	Graduate Student Researcher Quantum Physics and Techonology Research Lab UCLA Department of Physics and Astronomy

CHAPTER 1

Introduction

1.1 Quantum Information Processing

Classical information processing relies on bits. Information is stored and processed based on a series of binary digits 0 and 1. One example of a bit is the on and off of a transistor. In quantum information processing the information is carried by a quantum bit or 'qubit'. A qubit is normally a two level quantum system, of which we can write the eigen states as $|0>$ and $|1>$. In contrast to a classical bit, a qubit can not only be$|0>$ and $1>$ but it can also be in a superposition of these two. The possibility of creating superposition states combined with the entanglement of many qubits are what promise to make quantum information processing more efficient than classical information processing. To understand it more directly, one can imagine that for a classical bit, if we apply a calculation of bit 0(1), we will get f(0)(f(1)). However, if we perform same calculation f onto a qubit, we will get $f(|0>)$ and $f(|1>)$ simultaneously. Algorithm utilizing this parallel processing property makes the problem solving much faster than current computers. For multiple qubits this implies that the computation can be simultaneously carried out on all possible input states. The quantum mechanical property of destroying state by measuring leads to the field of quantum cryptography.

The field of quantum computing was first introduced Richard Feynman in 1982 [Fey82]. Several quantum algorithms have been developed since then. One well know example is Shor's Algorithm [Sho96], with which a quantum computer can solve large interger factorization problem which is infeasible for ordinary computer. In 2001, Shor's algorithm was demonstrated by a group at IBM, who factored 15 into 3×5, using an nulcear magnetic resonance (NMR) implementation of a quantum computer with 7 qubits [VSB01]. The last decade has seen a rapid growth in the quantum information processing field. It has gone to a stage of controlling and engineering individual quantum systems to manipulate and store information.

1.2 Semiconductor Lateral Quantum Dot

The chief goal of experimental quantum information science is to identify a system which will serve well as a qubit, a quantum two level system. There are five criteria that any candidate quantum computer implementation must satisfy proposed by D. Divincenzo, Listed as below:

1. Well-defined qubits;
2. Initialization to a pure state;
3. Universal set of quantum gates;
4. Qubit specific measurement;
5. Long coherence times.

Many systems have been proposed to realize a quantum processer and experimental demonstration has caught up quite fast. Among them are systems that find their origin in atomic physics, such as ions in electrostatic traps [CZ95], atoms in optical lattice [BCJ99], cavity quantum electrodynamics systems [THL95] and ensembles of nuclear spin in a molecule dissolved in a liquid [CGK98], and purely quantum optical approaches [KLM]. In the last decade, advances in nanotechnology have made it possible to engineer devices in solid state such as superconducting circuits containing Josephson junctions [MOL99], nuclei of implanted phosphorus in silicon [Kan98] and single electrons confined in lithographically defined [LD98] or self-assembled quantum dots [IAB99], impurities in Si [VYW00] and nitrogen-defects in diamond [JGP04]. Each approach has its own advantages and disadvantages. Some have already demonstrated a high level of control, e.g with nuclear magnetic resonance techniques a quantum algorithm has been realized using 7 qubits. However, the chances of scaling up this system are small. Ion trap experiments have also shown impressive progress, such as the demonstration of error correction [CLS04] and multi-qubit entanglement [HHR05], and efforts are put to make it scalable [HOS]. At this stage, it is hard to say which is system is currently the most advanced. The research at this point is still exploratory and many new ideals are still generated and assessed. Long coherence time, easy manipulation and system scalability are of great concern. In 1998, Loss and Divincenzo proposed the spin qubits of semiconductor quantum dot. Since then, tremendous effort has been put into developing semiconductor quantum dots which have high tunability and scalability. Scientists have made great progress in semiconductor quantum dot qubit in terms of initializaton, manipulation and readout.

When we talk about quantum dot, we must first realize that we live in a three dimensional world (no time space four dimensional at this moment) and electrons are free to move in three dimensional solid. Their movement can be described by a three dimensional wavefunction and their energy can be described in terms of band structures. Technological progress in material growth allowed for confinement of electron in solid such as potential well formed in GaAs/AlGaAs heterostructurs or at the interface of Si/SiO_2. In this case, electrons are only free to move in two dimensions. Thus we call it two dimensional electron gas. The energy of the electron in the confined direction (normally the growth direction) is quantized. When a potential well is constructed that traps electrons in all three dimensions it is know as a quantum dot. The particle energy becomes fully quantized. One kind of quantum dot system is to place metal gates (also called depletion gates) on top of a multilayer heterostructure wafer such as GaAs/AlGaAs, Si/SiGe or Si/SiO_2. These gates will spatially shape the conduction band of the quantum well once voltages are added. This type is called lateral confined quantum dots or electrically defined quantum dots. There are other types of quantum dots which are beyond the scope of this thesis. Lateral quantum dots have the major advantage that they are highly tunable. Since the confinement is provided by gate voltages, by changing these voltages we can change the depth of the potential well, the number of electrons held in the well and the tunneling rates of electrons in and out of the dots. Because of this tunability and scalability, lateral quantum dots have the most promise for realizing a quantum information system.

1.3 Qubit

Even within the context of electrons confined in quantum dots, there are various kinds of ways to define a qubit. All we need is a well defined two level system that can be easily controlled experimentally yet very weakly coupled to the environment. Here we will review a few cases based on both charge and electron spin. Each type of qubit has its own advantage and disadvantages. We will discuss in detail. But before we do that, I want to introduce the Bloch sphere representation that is commonly used in qubit description.

1.3.1 Bloch Sphere

Mathematically, a qubit state which is a superposition of the two basis states $|0>$ and $|1>$, can always be written in the form of $|\psi>=\alpha|0>+\beta|1>.\alpha and \beta$ are complex numbers that satisfy the relation$|\alpha|^2+|\beta|^2=1$. $|0>$ and $|1>$ are an orthonormal basis that spans the qubit subspace. By normalization, we can convert this expression to $|\psi>=sin(\theta/2)|0>+cos(\theta/2)e^{i\phi}|1>$. We can map out this state on a sphere, called the Bloch sphere with $|0>$ and $|1>$ pointing the north and south pole respectively as seen in FIG. 1.1.

The Halmitonian can be expressed in the basis of Pauli Matrices. σ_z determines the rotation of z axis on Bloch sphere, which changes the ϕ. The σ_x will modify θ. The qubit evolution is governed by Schrodinger equation

$$i\hbar\frac{\partial}{\partial t}\psi(r,t) = H\psi(r,t)$$

.

1.3.2 Charge qubit

A charge qubit can be understood with two qubit states crosspond to two different positions of a charge particle.This is normally realized in a coupled double quantum dot system. Two potential wells are physically close to each other with a tunable potential barrier between them. At certian barrier height, one electron can tunnel between the two dots. The voltages controlling the chemical potentials of the two dots are tuned such that the energy levels for one electron residing in either dot are equal to each other. The eigen states of the system will become the symmetric (ground) and antisymmetric (excited) superposition of the single particle wave function. The two base states of the qubit are then defined as the symmetric and antisymmetric states. The energy between the two qubit states is determined by the tunnel coupling or the barrier height between the double dot.

Ref. [HFC03] first demonstrated coherent oscillation in a GaAs double quantum dot system by adding fast pulse to transport ohmic contact and recording the corresponding current as a function of pulse duration. The oscillation frequency is 2.3GHz and the decoherent time T_2^* is 1ns. However, this readout scheme requires strong coupling between quantum dot and reservoir which limits the coherence of the qubit. Ref.[PJM04] manipulated a single electron in a fully tunable single electron GaAs double quantum dot using microwave excitation. Microwaves in resonance with energy gap between ground and excited states drive transition between charge state of $(0,1)$ and $(1,0)$. The difference in charge occupation is measured by a nearby noninvasive quantum point contact (QPC) charge sensing channel. From the measurement results, they concluded $T_1 = 16ns$ and a estimated lower boundary for T_2^* of 400ps for the single charge qubit. Later, Ref. [PPL10] applied fast pulse to the depletion gates to drive the qubit rotation. The oscillation was also read out by a QPC charge detector. They measured a maximum coherence time of $\sim$ 7ns at the charge degeneracy point.

Even though charge qubit suffers from strong decoherence due to the coupling between qubit and fluctuation in local electromagnetic fields from photons and phonones in the lattice, it still serves as a useful test bed for quantum coherent behavior in quantum dots. Furthurmore, developing a quantitative decription of charge coherence will help understanding quantum coherence in charge noise environment which is critical for the quantum dot approach to quantum information processing.

1.3.3 Loss Divencenzo Qubit

Besides charge, it is natural to think of two spin levels of an electron as a qubit. In 1998, Daniel Loss and DiVicenzo began the field of spin qubits in semiconductor quantum dots, where they described the Loss-DiVicenzo (LD) qubit. They proposed creating a quantum bit using the spin of an electron confined in a semiconductor quantum dot, where the basis state $|0>$ and $|1>$ were the spin up and down state. Control of these qubits could be achieved through electron spin resonance (ESR). A large magnetic field B_0 splits $|0>$ and $|1>$, and a small oscillating magnetic field perpendicular to B_0 drives rotations. The two qubit gates come from the exchange interaction brought on by tunneling between quantum dots, which when combined with the single qubit ESR rotations allows for universal set of one- and two- qubit gates.

Experimental attempt to form LD qubit began with Elzerman and Hanson [EHB, HBV05], where they demonstrated single shot readout of a LD qubit by observing a spin dependent tunnelling rate to the leads of the quantum dot with relaxation time T1$\cong$ .85ms. ESR control of a single LD qubit is completed with a stripline fabricated on top of a double dot structure [KBT06]. The minimum Rabi period is measured to be 108ns. Later, the authors showed a spin echo sequence with a coherence time of T2 $\sim$ 500ns [KNV08]. Ref. [NSL11] demonstrate the two qubit gate and entanglement with single shot readouts

This type of qubit requires a large magnetic field to generate sufficient energy gap between electron spin up and down state. Also, a microwave strip line is needed to transmit microwave to the dot. This increases device fabrication difficulty. None of the work in this thesis is directly related with this qubit. However, the resonant qubit protocol which we will discuss later basedon triple dot is similar to the ESR qubit control. Furthur more, Ref. [TPO10] has made a triple quantum dot structure with a micromagnet lay on top for the purpose of developing a three LD qubit device. This is another interesting direction for the triple quantum dot device.

1.3.4 Singlet-triplet Qubit

Singlet-triplet (ST) qubits are the most widely studied spin qubit in the last several years pioneered by the theoretical work [Lev02] and followed by [TPJ07]. This qubit is formed from the symmetric $|T_0(1,1)>= 1/\sqrt{2}(|\uparrow\downarrow> +|\downarrow\uparrow>)$, and anti-symmetric $|S>= (|\uparrow\downarrow> -|\downarrow\uparrow>)$, combination of spins of two electrons confined in two neighboring quantum dots system. The exchange energy is defined as the energy difference between singlet state and triplet state. Due to the tunnel coupling between the double dots, wave function of $|S(1,1)>$ and $|S(2,0)>$ overlap and create a gap between the mixed singlet state and triplet state at detuning $\epsilon = 0$. Here, detuning is defined as the energy difference between level of S(1,1) and S(2,0). In a Bloch sphere representation, seen in Fig. 1.2, $|S>$ is pointing north pole, while$|T_0>$ point south pole. The exchange interaction will drive rotations around the $S-T_0$ axis. To realize a qubit rotation, the exchange itself is not enough. Ref. [TPJ07, PJT05] used the nuclear Overhaser field difference across the double dot ΔB_z which is on xy plane in bloch sphere to provide the σ_x rotation. The qubit is initialized in (2,0) electron configuration with a ground state $|S(2,0)>$. A tunnel coupling allows electrons transfer from a 2,0 configuration to 1,1. Deep into 1,1 regime, exchange is negligibly small and the system is controlled by the hyperfine interaction. The ground states of the system are $|\uparrow\downarrow>$ and $|\downarrow\uparrow>$ lie on the xy plane. The S(1,1) will evolves into one of these two states. The system is then pulsed quickly to places where exchange interaction is much stronger than overhauser field. The state will rotate around z axis in the xy plane. After certain time, the state is quickly pulse to deep (1,1) configuration and then adibatically pulse back to (2, 0). After manipulation, electron state can be either $|S(1,1)>$ or $|T_0(1,1)>$. Due to conservation of total spin and the Pauli exclusion principles, S(1,1) state can tunnel back to S(2,0), while T(1,1) state is unable to do so. This charge configuration difference provides means to read out the spin state.

The cohrence time in this system is defined as how long a separate (1,1) state can maintian its phase information. This is done by preparing a S(2,0) state and pulsed deep into (1,1) regime. The random fluctuation in nuclear field will cause the state to dephase. And when the system is pulsed back to (2,0) state, the difference will be detected.

The coherent manipulation of singlet triplet qubit was first demonstrated by Ref. [PJT05], where the rotation period due to the exchange interaction was demonstrated to be as small as 700ps, while dephasing time T_2^* was found to be around 10ns. Following spin echo experiment shows a coherence time of 1.2us. The coherence time is mainly limited by the random fluctuation of nuclear field that surrounding the electrons confined in quantum dots. This motivates people to work on system with much less nuclei such as Silicon. Recently, it is demonstrated in a Si/SiGe heterostructure double quanutm dot, the dephasing time T_2^* is around 360ns [MBH12]. However, both [PJT05, MBH12] rely on random nuclear overhauser field difference across the double dot to realize single qubit rotation while the overhauser field is hard to control. To achieve fast rotation, a micromagnet is proposed to give an controlled magnetic field gradient ΔB . [POT07, POT08, OPT10]. However, this will complicate device fabrication.

1.3.5 Exchange-only Qubit

In both LD and ST qubits, a temporally or spatially varying magnetic field was required to provide two fast coherent rotation axes. This makes both device fabrication and experimental control techniques challenging. Reference [DBK00] proposed forming a qubit out of three electron spins using the Heisenberg interaction alone. For a three electron system, only considering the exchange interaction between electrons, the eight eigen states are divided into two groups with total spin S=3/2 and 1/2. Here the halmitonian is $H = \sum J_{ij} S_i \cdot S_j$, i,j=1,2,3. J_{ij} is the exchange energy between electron spin i and j. When we trap these three electrons in three neighboring quanutm dots with one electron per dot, the above argument is still valid. As we discussed before, the depletion gates which defined quantum dots can tune the chemical potential level and the tunnel coupling between dots. Thus the exchange energy $J_{i,j}$ is a function of tunnel coupling and relative chemical potential between dots where electron i and j are confined. The energy levels for three electron spin confined in three dots in the presense of a $300mT$ magnetic field is shown in FIG. 1.3 (b). We see the four quadruplet states split due to the magnetic field. For simplcity, we only plot one group of $S = 1/2$ state with $S_z = -1/2$, shown as the blue and magneta lines.

Within the subgroup of $S = 1/2$, $S_z = -1/2$, qubit can be encoded into two states with same $S_z = -1/2$. One choice of encoding a qubit can be $|0>=|S>|\uparrow>$, $|1>=\sqrt(2/3)|T_+>|\downarrow> - \sqrt(1/3)|T_0>|\uparrow>$. Here the $|S>, |T_+>$, and$|T_0>$ are all states for right two electrons. We can map the system onto a bloch sphere, seen in FIG. 1.3 (b). We consider three dots linearly arranged, thus exchange interaction between first dot and third dot is negligible. We name J_l as the exchange interaction between dot 1 and 2, while J_r for dot 2 and 3. If we define a bloch sphere based on $|0>$ and $|1>$, J_l and J_r will sit symmetrically in the X0Z plane, 120° away from each other. Using classic Euler-angle construction, J_l and J_r are sufficient to provide a single qubit rotation. The exchange can be tuned very large using fast electrical pulses sending to certain depletion gates thus the rotation can be very fast. In Chapter 6, we will describe the details of the practical qubit operation protocols based on this proposal and show simulation results. The advantage of this exhange-only qubit is that we no longer need a mangetic field gradient in the system. And the qubit rotation can be fast for a proper tuned the exchange energy.

The experimental attempts began with the development of an electrostatically defined triple quanutm dot device in GaAs heterostructure [GKG09, LTD10]. The tunability of the triple quantum dot was shown by tuning the three dots level on resonance both in charge sensing signal and transport [GGK10]. The initialization of a three electron qubit was demonstrated in Ref. [LTD10]. Continuing this work, Ref.[MBT13a] utilized a new triple dot depletion gates layout in which three dots are arranged in series and almost zero exchange interaction between the first and third dot. They demonstrated initialization, complete electrical control, and single-shot readout of an exchange-only spin qubit. They demonstrated 75 qubit rotations in 2ns. They also use a maximum-likelihood estimator method to quantify the decoherence, leakage out of the qubit state space, and measurement fidelity.

Recently, Ref [TSM13] introduced, the resonant exchange only qubit, a modification of the original Divicenzo proposal. The qubit rotation is done via Rabi-nutation using gate controlled exchange both for the static longitudinal field and the oscillatory transverse field. The large exchange field suppresses leakage from the qubit space. This proposal was successfully demonstrated experimentally by Ref [MBT13b].

Most of the theorectical work on the decoherence and dephasing in an exchange only system has been focused on hyperfine interaction, charge noise and phonon interaction. Ref. [Lad12] analyzed the effects of hyperfine interactions on coherent control experiments in triple quantum dots. Based on his proposals, the nuclear field difference between neighboring dots σ_l and σ_r can be extracted from hyperfine decay of Rabi oscillations and dephasing experiments. However, this work does not yield much information about charge noise. Ref.[MD] gaves more information.

Ref. [GGK12] took a different approach to coherent manipulation of three electron spins that uses adiabatic passage through nuclear mediated transitions, which is called Landau-Zener transition, similar to work done in the double dot system with an $|S>=|T_+>$ qubit [PLG10]

The success of exchange only qubit based on GaAs heterostructure greatly motivates us to start our journey in silicon with the hope that less nuclear spin provides longer coherence time. This is the original motivation of this thesis.

1.4 Relaxation, Decoherence, Dephasing

In last section, we have discussed a few types of qubit based on solid state laterl quantum dots. These qubit can be viewed as two level systems (TLS). To realize quantum computation, a unitary operation is applied to an array of these TLS. However, the TLS is normally weakly coupled to the environment. And the weak interaction will cause decoherence of the qubit states. Fortunately, it has been shown theoretically that if the decoherence is small enough compared to the rate at which qubit operations can be performed, it is possible to impletement quatum error correction codes that will allow the quantum state to be maintained indefinitely [BDS96, KLV00]. The ratio between gate time and decoherence time needs to be smaller than $10^{-3} \sim 10^{-6}$, which is current quantum error correction limit. Thus understanding the decoherence mechanism of a given system is extremely important for realization of quantum computer.

As discussed before, information can be coded into superposition of state $|0>$ and $|1>$ in forms of $|\psi>=\alpha|0>+\beta|1>$. If the system is completely isolated from the environment, the state will evolve as $|\psi>->e^{i\phi}|\psi>$. However, in reality, there are always coupling between our qubit and the environment. In solid state system, one would imagine hyperfine interactions, spin-orbital couplings, electron-phonon interactions, etc. Some of these interactions involve either emission or absorption of energy which resulting in a change of relative amplitude of $|0>$ and $1>$. The time scale related with this process if called T_1 or lifetime of the qubit.

The second type of interaction is phase noise. Phase noise can be understood as the system losing phase coherence between the two computational basis state$|0>$ and $1>$ but does not change the relative population between them. Phase noise can be separated into two groups, dephasing and decoherence. Dephasing is a measure of how rapidly an ensemble of qubits lose phase information, and is described by the timescale T_2^*. Dephasing occurs when members of the ensemble experience different conditions, such as local magnetic or electric environments, which causes the members to evolve under lightly different Hamiltonians, resulting in a distribution of phase across the ensemble. Decoherence is a measure of how rapidly an individual qubit lose its phase information. This information can be lost due to entanglement with the environment, or classical noise. The timescale is normally called T_2. Dephasing can be mitigated by clever qubit manipulation using dynamical decoupling techniques, which cancel out static or slow variations in the Hamiltonians across the ensemble, restoring coherence. One example is the Hahn Echo [Hah50]. $T_2 > T_2^*$ while $T_1 > 2T_2$.

Relaxation, decoherence and dephasing is of great concern when people look for suitable system for quantum computing. In this thesis, we will discuss silicon based spin qubit. Ref. [HSS] gives a very good review about decoehence, dephasing for spin based solid state quantum computers. Beyond general description, there is another practical source of decoherence that we want to emphasize is the charge noise. Ref.[CHS09] dicussed specifically about a quantum dot device near a Si/SiO_2 interface, where the presence of defects such as Pb centers are inevitable and the oxide is well known as source of charge noise. When spins are coupled via exchange interaction, they can be adversely affected by charge noise because exchange is coulombic in nature. This is independent from the normal nuclear hyperfine interaction.

1.5 Dissertation Outline

This dissertation is proposed with the goal of fabricating and characterizing a tunable triple quantum dot on silicon MOSFET with the possibility of demonstrating coherent manipulation of an exchange only qubit. Chapter 2 mainly describes the fabrication procedure and experimental set up. Chapter 3 discusses various experimental techniques used to characterize the charging and spin information of both a silicon MOSFET based double quantum dot and triple quantum dot. In Chapter 4, we first develop the constant interaction model to simulate the charge stability diagram of a triple quantum dot and reveal its tri-dimensional nature. We then extend the model into Hubbard model where we include the interdot tunnel coupling. This model allows us to study the quantum effect in the charge stability diagram at first order approximation. Chapter 5 presents the first experimental demonstration of a triple quantum dot based on Si-MOSFET. We shows the tunability and controllability of the device by tuning the system into quadruple points (QP) where the three dots are on resonance. The experimental results are reproduced using hubband model calculation. In Chapter 6, we review the physics of a half filled triple quantum dot (three electrons) in terms of Heisenberg interaction model. We implement the Divencenzo proposal of exchange only qubit based on linear arranged triple quantum dot with neighboring exchange interaction. We then calculate a more generalized triangular shaple triple dot in the frame of Hubbard model. In Chapter 7, we will discuss various fast pulse techniques used to detect spin and charge information in a triple quantum dot. We report interesting fast oscillations probably induced by spin dynamics. In last chapter, we summarize our work and give a future outlook.

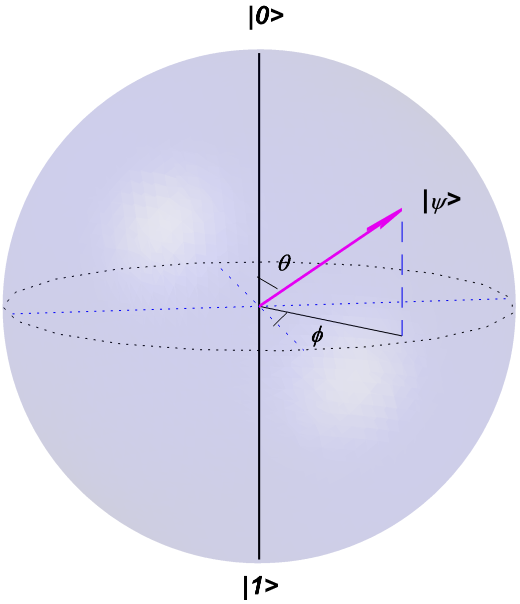

Figure 1.1: Bloch sphere representation based on two level $|0>$ and $|1>$, arbitrary state $|\psi >= sin(\theta/2)|0> + cos(\theta/2)e^{i\phi}|1>$ mapping on Bloch sphere

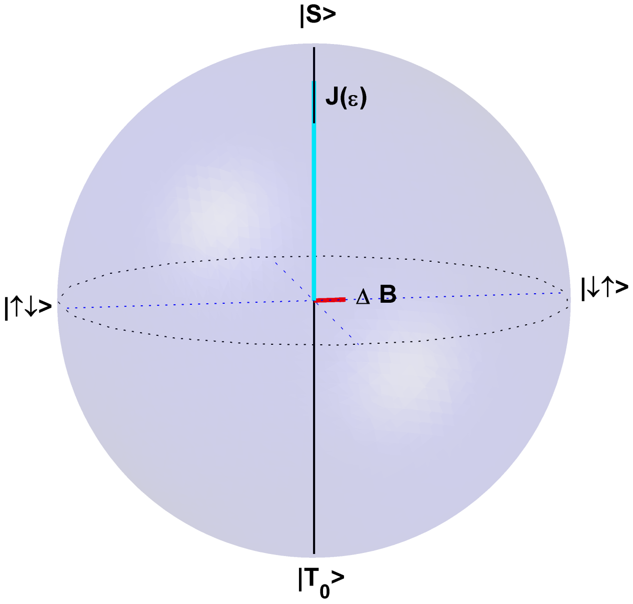

Figure 1.2: Bloch sphere representation based on two electron spin singlet triplet states $|S>$ and $|T_0(1,1)>$, the exchange $J(\epsilon)$ is along the z axis, while the nuclear Overhasuer field difference across the two dot in z direction ΔB provides the rotation on x axis

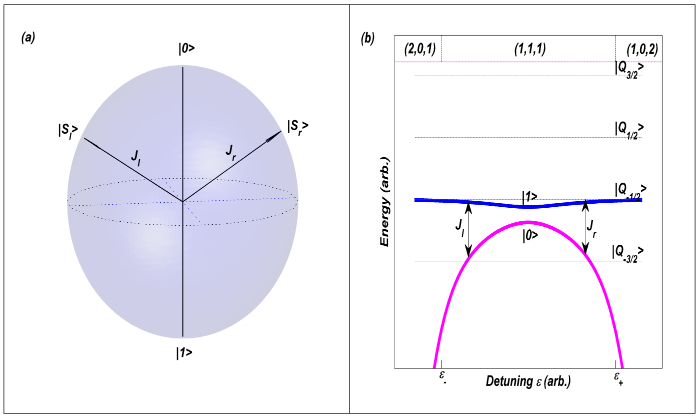

Figure 1.3: (a) Bloch sphere representation for exchange only qubit. Two states $|0>$ and $|1>$ are defined shown in (b). Two rotation axis J_l and J_r is 120 degree away.(b) Energy levels for three electrons confined in three quantum dots arranged in series. Detuning ϵ represents the relative energy difference between electron energy levels in charge configuration (2,0,1) and (1,0,2).(N_1,N_2,N_3) indicates electron number in each dot.

CHAPTER 2

Si MOS based triple quantum dot device fabrication and experimental set up

2.1 Si based quantum dot device

As we discussed in the previous chapter, solid state quantum dots are believed to be a promising candidate for scalable quantum computing. We already named a few types of qubits in last chapter that use electron confined in quantum dots. Two important parameters that describe the coupling between the qubit to the environment are T_1 and T_2^*. In well studied GaAs heterostructure based quantum dot devices, T_2^* is measured to be around 10ns mainly due to the contact hyperfine interaction between electron spin in quantum dot and the local nuclear spin bath. In light of this, the advantages of silicon are clear. It has small spin orbital coupling, no piezoelectric electron-phonon coupling and weak (which can be reduced furthur through isotope purification) hyperfine coupling. Thus electron spins are predicted to have excellent quantum coherence properties in Si systems. In a recent experiment of undoped Si/SiGe system, T_2^* is measured to be 360ns. In Si MOS based double quantum dot, T_2^* is estimated to have a lower boundary of 100ns basd on the linewidth of electron spin resonance signal. Both these results are at least ten times longer than GaAs system which makes Silicon a natural next step for solid state quantum computing.

Silicon based lateral quantum dot devices have been realized in several different subsystems, such as Si/SiGe heterostructure [STR09, BEC11], which uses similar fabrication procedure as GaAs/AlGaAs heterostructure system. Some groups studied the silicon-metal-oxide based system. Ref [TNY10] uses the similar gate stack geometry as we do here at

UCLA except they use polysilicon instead of metal as the material for depletion gates. Ref. [LZH09, LLY11] use more complex $Al - Al_2O_3 - Al$ stack to define single or double quantum dot in which the dot lithographical size is much smaller. Donor type quantum dot device is also widely used in which phosporus dopant is implanted into silicon metal oxide with an single electron transistor fabricated nearby [MPZ]. The detailed information about development and progress in silicon quantum electronics can be found in Ref. [ZDM13]. Our lab works specifically on Si metal-oxide-semiconductor (MOS) based structures. This type of device has easy integration into current industry infrastructures. In the past five years, M. Xiao and House successfully fabricated stable single and double lateral quantum dot[XHJ10, HPX11]. This work is a continuation of their work.

2.2 Device operation mechanism and fabrication process

2.2.1 Si-MOS based quantum dot device operation principle

We first want to discuss Si MOS based quantum dot device operation principle. For simplicity, we consider a single quantum dot. FIG.2.1 (a) shows the cross section view of the a typical Si-MOS based lateral quantum dot device.

We start with a commercially grown p doped Si/SiO_2 wafer. The silicon dioxide is 50nm thick. On top of the SiO_2 lies the depletion gates which are normally metal gates defined by e beam lithography. The top control gate is separated from the depletion gates by 100nm thick aluminum oxide. The Al_2O_3 is grown by atomic layer deposition. A detail fabrication recipe can be found in the supplementary material. When one adds positive voltage to the top gate, after the threshold voltage, one layer of two dimensional electron gas starts to accumulate at the interface of Si/SiO_2 as in MOSFET. If voltage bias is added through one ohmic contact, current will be collected at the other ohmic contact. Then negative voltages are added to the depletion gates. This repels the electrons underneath the gates resulting in a potential well in designated area, marked by the black dash line. FIG.2.1 (b) gives a better three dimensional view. For simplicity, the top gate and Al_2O_3 are not shown.

The black polygon on the top surface depicts a typical single dot depletion gates layout. With negative voltages on them, the gray shadow at the Si/SiO_2 marked the places where electrons can stay. This circlular area is called the quantum dot. Due to strong confinement, the energy level inside the quantum dot is discrete. By adjusting certain depletion gate voltage, one can control the chemical potential of electrons inside the quantum dot thus control the electron tunneling in and out of the dot. By changing the depletion gates layout, one can realize single quantum dot, double or more quantum dots. These potential wells are purely electrically defined and can in principle be calculated by considering the gate voltages, layout and thickness of silicon dioxide. FIG. 2.2 shows the calculation result for a circular arranged triple quantum dot. The inset shows the SEM image of the depletion gates layout. The colorbar of the main diagram shows the electric field strength magnitude with red the highest and blue the lowest. The calculation only shows the electrical potential at the surface of SiO_2. Three potential minima are realized for electrons seen as the three blue dots. The real potential at Si/SiO_2 is similar to this result. More precise result has to include self consistent calculation considering the electron distribution inside the quantum dot and the interface charge trap [BEC11].

The electron movement inside the dot can be detected directly by measuring current through the quantum dot. This is usually called transport measurement. In this case, only when the Fermi level of the reservoir matches the chemical potential of the dot, can electrons tunnel through the dot from the source to the drain. In the case of a double dot or triple dot, the energy levels in each dot need to align in order to make the electrons tunnel through. Another type of detecting method is called charge sensing. A quantum point contact (QPC) channel is fabricated nearby the quantum dot. The movement of electron on the quantum dot side will change the local electrical field sensed by the nearby QPC channel. The signal strength is normally 1% of the total current. The QPC channel is usually called noninvasive sensing since it does not directly interact with quantum dot.

2.2.2 Triple quantum dot device fabrication

Now we comes to the most important part during device fabrication process, design of the depletion gates layout. Undergraduate quantum mechanics teaches us that for a simple one dimensional quantum well with infinite barrier height, the particles trapped inside has discrete energy levels $E_n = (nh)^2/8mL^2$, where n is the level number. The energy space is proportional to $1/mL^2$. The large effective electron mass of Si, $0.19m_e$ in the direction of Si/SiO_2 interface, which is nearly three times larger than that in GaAs , $0.067m_e$, leads to shrink of energy spacing. In order to maintain large energy spacing, we need to decrease the size of the dot, reducing the depeletion gates confinement area.

Lateral double quantum dot depletion gates layout is very mature in terms of layout design. Several groups started studying GaAs heterostructure based triple quantum dots a few years ago. Ref. [LTD10, SGG07] take the circular approach while Ref. [GKG09] present in their study that the circular structure tends to stabilize in double dot configuration. They developed a new patter which is a modification of double dots with modifications.

As we stated in the first paragraph, silicon has different effective mass than in GaAs. Additionally, GaAs has much high mobility while Si/SiO_2 suffers more from charge impurity and interface traps. Taken all of this into account and bearing in mind the limit of e beam lithography, we started developing triple quantum dots with different depletion gate layouts. FIG.2.3 shows several structures we have tested.

The first design FIG. 2.3 (a) is a natural expansion of a common double dot design except we have two vertical gates (T) instead of one in double dot [GKG09]. However, due to the limitation of e-beam lithography line width in house, the dot size cannot be decreased too much. We found that the dot is too large to form three well defined quantum dot. Additionally, the near by quantum point contact channel is weakly affected by the electron movement inside the quantum dot. This design was quickly abandoned and modified to the second one FIG. 2.3 (b). The dots are much smaller and the charge sensing channel are completely separated from the transport channel. The slot between the dot and QPC channel increase the sensitivity. However, we realized in experiment that there are some disadvantages to this design. It is difficult to resolve some of the fine features in this design when doing e-beam lithography. The three dots requires very fine tuning of depleting gates voltage. Another problem we found later in experiment is that the space left for QPC channel is tight. This design normally results in large double quantum dot QPC channel and most sensitively point does not sit exactly at the slot. Meantime, we tried the design FIG. 2.3 (c), which was adopted by a Harvard group [LTD10] and it turned out to be very robust. Almost all the device we tested in He3 Fridge give similar charge stability diagram and this design offers lots of tunability. There is a small slot between the QPC channel and the quantum dots. The space left for charge sensing channel is large compared to other layout so that the current through the QPC channel is mainly controlled by the junction between Q gate and the slot. As you seen from the diagram, each gate is assigned a name based on its function. Three dots are designed to be in the position where the pink dots are drawn. The BL,BR gate are supposed to control the tunneling barrier between reservoir and the quantum dot. L, R, QL, QR gates are mainly used to tune the chemical potential of the three dots. QL and QR also change the slot barrier between the dots and QPC. TL, TR are designed to control the tunnel coupling between neighboring dots. T gate is extremely strong and normally is grounded. In Chapter 4, we will discuss in detail about the tunability of device based on this design.

As discussed earlier, the quantum dot lithography size needs to be substantially smaller than those of GaAs in order to reach last few electron configuration. However, we didnt find extreme difference in dot properties in terms of charging energy of the dot due to different dot dimensions. The charging energy we found in our devices in last few elecron is around $3 \sim 5$ meV while those reported in Si/SiGe herterostructure based quantum dot is around $6 \sim 8$ meV [BEC11]. Thus we keep the original double dot dimensions used by Ming Xiao and Matthew House [XHJ10, HPX11]. In the case of this circular triple dot design, I use 220nm as the radius, L_r.

During the process of optimizing the circular trip dot design, we found the following dimensions which matter most in determining the device quality. They are marked by red, green and yellow lines in FIG. 2.4. Their length is defined as L_b, L_r and L_s respectively.

The red line, L_b, controls the tunnel barrier between reservoir and quantum dot. The green line, L_t, determines the tunnel barrier between neighboring dots. The yellow line, L_s, controls the field line transmission from the dot to the nearby QPC channel. Since silicon has much less mean free path than gallium arsenide, around 30nm. Often the tunnel barrier between reservoir and dots tends to be much higher than the barrier between neighboring dots thus we can not tune the quantum dots to last few electron regime. After testing different devices, we found that $1.1 > L_b/L_r > 1$ gives better chance for the quantum dot to go to last few electron regime. In our device, all the depletion gates are covered by the top gate. The vertical electrical field is screened by the top gate, thus the slot is very necessary to increase to sensitivity of the charge sensing channel. However, if the slot is too open, then one needs to apply more negative voltage to gates QL and QR which in fact change the chemical potential of the middle dot. The empirical value for$L_s/L_r = .4$, which means in the case of a 220 radius circular design, the slot should be around 95nms. One also needs to keep in mind the actual line width of $30 \sim 50$ nm.

2.3 Device screening process

2.3.1 Device screening

Once the device is mounted on the chip holder, it is ready to be tested. Cooling fridges to base temperature requires lots of time and effort. It is better to pick out the best devices at 4.2K. In our lab, we normally screen devices at different temperature stages. At 77K, leakage current can be detected if there is any. Once the device is turned on, the transport and QPC channel current will decrease if negative voltages are added to certain depletion gates. This help us rule out most of the bad devices with bad contacts and unresponsive gates. At 4.2K, the turn on curves for both transport and charge sensing channel are recorded. The conductance of charge sensing channel is normally around 1.5nA/125uV while the conductance is around 100pA/125uV. Normally, either transport current or charge sensing channel current is recored as a function of depletion gates voltage. The current normally goes to zero with moderate negative voltage on the depletion gate. However, this kind of one dimensional scan cannot tell much about the quantum dot itself. Later, we found that a 2D scan of transport current will reveal most of the information need about a device. FIG. 2.5(a) shows a very organized transport diagram with large biasing triangle at 4.2K by scanning V_L and V_R. FIG. 2.5(b) shows the charge sensing diagram from the same device at 300mK. We've tested more than ten devices for comparison and found out that devices with organized two dimensional transport diagram also show good charge stability diagram at low temperature. For those device with bad 2D scan transport diagram at 4.2K, the stability diagram also do not look good at 300mK. This two dimensional scan at 4.2K helps us pick out deivces of better quality.

2.3.2 Bias cooling

When we consider Si-MOSFET, we normally treat silicon dioxide as an perfect insulator. However, in reality, the silicon dioxide and the oxide-silicon interface are never completely ideal. There can be mobile ionic charges, electrons and holes trapped in the oxide layer. Fabrication process such as e-beam lithography and e-gun evaporation can also introduced fixed oxide charges near the oxide-silicon interface and charges trapped at the so-called surface states at the oxide-silicon interface. Details about the charges in silicon dioxide and interface can be found in Ref. [TN]. Electrons and holes can make transitions from the crystalline states near the oxide-silicon interface to the surface states, and vice versa. These fixed charge and interface traps will inevitably affect the device performance especially for the quantum dot device which is only few hundred nanometers in diameter.

During multiple cool down tests, we found that the threshold voltage and sometimes depletion gates performance varied with each cool down attempt. Ref. [PGK02] adopted the bias cool down technique when they tried to studied the metal insulator transition of two dimensional electron gas in Si-MOSFET inversion layer. They cooled the Si-MOSFET from room temperature to 4.2K with top gate biased at different positive voltages V^{cool}. According to them, V^{cool} determines the depth of the confining potential well and, simultaneously, the number of interface traps below the Fermi level. At low temperatures, as top gate voltage is varied, the potential well remains almost unchanged and memorizes an imprint of the disorder formed during its cooling down. The temperature dependences of the 2DEG resistance carry a strong imprint of individuality of the quenched disorder determined by V^{cool}.

This motivated us to study our quantum dot device behavior using this bias cooling technique. We started with testing a quantum point contact device with multiple contacts. Each time during the cool down, a specific top gate voltages is maintained from room temperature to 4.2K. When the device is completely 4.2K, the top gate is ramped down to zero. And normal I-V curve is recorded between different contacts. FIG. 2.6 shows the device layout and bias cooling study result.

FIG. 2.6 (a) schematically illustrates the top view of the quantum point contact device layout. For this device, there are only two depletion gates, shown as the blue bars, which define a 300nm junction. We call this device a quantum point contact device. Several ohmic contacts are made, marked by the red dots. Current measured between low left two contacts are just normal FET measurement while the current marked by I_{QPC} records the current through the quantum point contact junction. The junction is only 300nm wide which mimic the real barrier width in a quantum dot device. FIG. (b) shows the turn on curve records I_{FET} for the same ohmic contacts at different bias cool down. The threshold voltage increases almost linearly with positive bias voltage. The effect is more pronounced for I_{QPC} , seen in FIG. 2.6 (c). This confirms that the bias cool down does affect the charge impurity or interface traps distribution thus change the threshold voltage. A naive way to understand is that at room temperature, when positive voltage is added to the top gate, charge impurity or traps inside the oxide are either filled or emptied due to the electric field across the silicon dioxide. When cooled to 4.2K, the thermal excitation is too small to make any change. According to the positive shift, it is concluded that the positive charge impurities are filled at room temperature. More experiments showed that this memory effect is reversable when device is warmed to room temperature and repeatable when cooled with same bias at different time. This helps us while transferring device between different cryostats without worrying about device properties changing too much .

Negative bias voltage cool down seems to not have much effect on threshold voltage. Ref. [FGB06] used negative bias while cool down when study sodium doped silicon MOSFET. -4V is added to the top gate for 10mins at $65 \circ C$ to let the mobile ion drift back to Al-SiO_2 interface. Thus the mobile ion will not affect the electron transport at Si-SiO_2 interface. Interface traps are crucial to low temperature operation of MOSFET and quantum dot devices. The alternate capture and emission of carriers at an individual defect site generate discrete switching in the device resistance-referred to as a random telegraph signal (RTS). The origin of interface traps can be different. Recently, one set of devices showed strong fluctuation in current at 4.2K. By using the negative bias cooling procedure, we found the current fluctuation was greatly suppressed. We suspect this suppression is related with fiiling of interface traps. However, the origin of this traps are still unknown.

2.3.3 Cryostat set up and wiring

In order to detect single electron dynamics inside quantum dot out of the 2DEG reservoir, the electron temperature should be well below 1K. At 1.5K, we can still see some signature of electron tunneling events. However, the signal to noise ratio is poor. All of our devices go through a first stage screening done in a Oxford top loading He3 fridge. The top loading fridge provides the flexibitiy of changing devices in very short time. Changing the device and recooling the fridge can be done within 4 hours. The base temperature is around 300mK and a full condensation can maintian the fridge at base temperature for 24 hours. It is also equipped with one coax line which allows transmission of RF signal up to 20GHz. Some charge qubit experiments can be performed at this temperature. The detailed structure and operation manual for this He3 fridge can be found in [Xia04]. The characterization experiment of triple quantum dot discussed in Chapter 4 is done in this He3 frige. There are two drawbacks of this fridge. One is the base temperature, 300mk, which corresponds to $25\mu eV$ which is larger than the interdot tunnel coupling desired to perform fast qubit manipulation experiment. Second is the cooling period. We need to condense everyday and the system warms up to 1.3K. This causes our device to which is not good for controlled experiment. Nevertheless, the quick turn over time and simpleness in handling of He3 fridge provide a good stage for screening devices.

The Janis 500 dilution fridge has 500mW cooling power at 100mK and can easily get down to 50mK. FIG. 2.7 shows the main inset of the fridge marked with different temperature stage. The phonons in the semiconductor lattice will have a similar temperature as the base temperature of the refrigerator, but the electron temperature of the 2DEG is always higher. In our measurement, we found it to be around 200mK. There are various reasons for this. First, due to the weak electron-phonon coupling, electrons are cooled mostly via DC wires which are connected to the source/drain contacts. Furthermore, they are very sensitive to radiation or noise in the DC wires. Normally, there are different filtering stages at different temperatures and covering different frequency rangs, Ref. [Kop08]. However, we didn't add filter when we set up the fridge due to the risk of introducing extra electrical complexity. And the 200mk is not detrimental to our experiments. In the future, addition of filters will help us bring down the electron temperature and provide a better experimental environment. We also suspect that the connector which corrects the room temperature BNC cable to conner wires inside the fridge doesn't provide good shielding between DC lines. This might introduce extra noise.

The Dilution fridge is equipped with 32 cooner wires and 4 coax cables for high frequency signal transmission. The cooner wires have an inner conductor and are shielded from outside conducting layer by a insulator. Thus they have a large bandwith. They mostly serve for DC voltage output and current detection. The qubit manipulation experiment requires sending high frequency signals down to the device which is done by the coax cable. We also calibrated the cooner wires transmission and found they have a bandwidth of up to 20MHz. Calibration diagram for both 4 coax cables and coonner wires can be found in supplementary material. To minimize the thermal transmission from the coax cables, we put 30dB attenuator on two of the coax lines inside the fridge below the 1-K pot. However, it did not turn out to be very reliable. Any mismatch at the connection will destroy the signal. Even if the connection is good at room temperature, any thermally induced contraction can change the connection.

2.3.4 Chip holder

The chip hold we first used for the Dilution fridge is shown in close up picture in FIG. 2.7. The device is mounted in the center area using super glue or epoxy and wire bonded to the copper contacts nearby. We modified the holder to the new version 2.8, re-arranged the lead pattern on the plate to avoid wirebonding difficulty. It is difficult to do wirebonding when you have the cooner wires already soldered to the holder for the older one. Later we realized that the copper plate is oxidized easily and is not good for reuse, as can be seen from FIG.2.8. Additionally, there is no sheilding between coax lines and normal DC lines. Crosstalk is potentially large. Even though it does not affect our primary experimental results. It will be helpful to upgrade it. We have recently re designed the chip holder with two considerations in mind. First is to use Ni/Au plating to replace the copper at wire bonding window. Second is to create grounding plate between DC lines to minimize the cross talk. FIG. 2.9 illustrates the CAD diagram and it has been suscessfully made and is ready for future use. This CAD file was made by Joshua Schoenfield. Unfortunately, I missed the opportunity to try it. More advanced designs in the future might be adopted for the purpose of seperating RF grounding and DC grounding such as in Ref. [CR12, BcR12].

Another chip holder design we used is called the "plug in" type, as seen in FIG.2.10 . We mount the socket directly onto the copper board, thus the 16-pin carrier can be directly plugged into the chip holder without transfer device. The drawback of this design is the loss of bandwidth for high frequency signals. We've tested the RF transmision on this plug in type holder and found that it can sustain 2GHz signal without much attenuation.

2.3.5 Measurement electronics and grounding

Low frequency measurements of the device involve electron transport through quantum dot and quantum point contact as a function of source-drain voltage and applied voltages to the depletion gates. The ac measurement is done by the SRS 830 lock-in amplifier while the dc characterization is performed using either SRS 570 low noise Current preamplifer or DLPCA-200 amplifer. One needs to consider the change in DC input impedance of current amplifiers when switching sensitivities. The later one is used in the low frequency (1/f) noise measurement experiment. We use the lock-in DC voltage output as our DC voltage source. We found that the lock-in DC voltage output normally has an offset and the fluctuation is around 1mV. Battery box gives much stable output. A better solution would be a digital to anaglog box which has much lower noise compare to lock in DC output.

We use Tectronix AWG 520 to supply complex pulse sequence. The AWG 520 has a sampling rate of 1GHz and provides two channels which is good for qubit manipulation. The AWG 610 has a higher sampling rate 2.6GHz. However, it only has one channel. The equipment can only store 64GBt data. A network file system is used in our experiments for storing pulse files. The Agilent 81134A pulse generator is used in charge excitation experiments. It can supply fast pulse as short as 150ps with a rising time of 70ps.

To avoid the risk of sudden power outrage, we power all equipments through a Universal power supply (UPS) system. All equipments share the a common ground. One thick wide metal stripline connects the fridge and the copper grounding block to cancel grounding loop.

2.3.6 Bias-Tee

Bias Tees are heavily used in quantum dot characterization and qubit manipulation experiment. The upper bandwidth limit is sufficient in almost all of our experiment. The low boundary matters a lot. The device is very sensitive to any voltage change or line re configuration, thus it is better to choose suitable bias tee to avoid changing line configuration frequently. We have three kinds of bias tee in lab. Picosecond lab model 5546 bias tee has a bandwidth of $3.5KHz \sim 7GHz$ and it is good nuclear based coherent manipulation. The miniCircuit bias tee works at $100khz \sim 2.8Ghz$. The Anritsu K251 bias tee has a bandwidth of $50KHz \sim 40GHz$. Another peice of useful equipment is the summing amplifier manufactured by Stanford Research System which has an upper bandwidth of 1MHz.

2.3.7 Device mounting

Our device has more complex structure than GaAs quantum dots. The depletion gates are covered by a top gate with one layer of Al_2O_3 sandwiched between them. This capacitive coupling between the top gate and the depletion gates will inevitably influence any fast pulse or RF signal applied to the depletion gates. In FIG. 2.11, the blue curve shows a 100mV and 300ps pulse going through a 500nm wide Al depletion gate with top gate float. The pulse shape doesn't change much except the amplitude is attenuated. However, if the top gate is grounded, the pulse shape deteries badly as seen as the red curve. To minimizing this effect, a surface mount film resistor is added between the top gate and chip holder contact. These surface mounted film resistors is small in size and its resistance doesn't change even at very low temperature. FIG. 2.11 shows the result for film resistors with different resistance. We found that the 100KΩ gives the least pulse shape deterioration. The magnitude of resistance depends on the thickness of Al_2O_3 layer and the area of the top gate. These resistors can be purchased from DigiKeys.

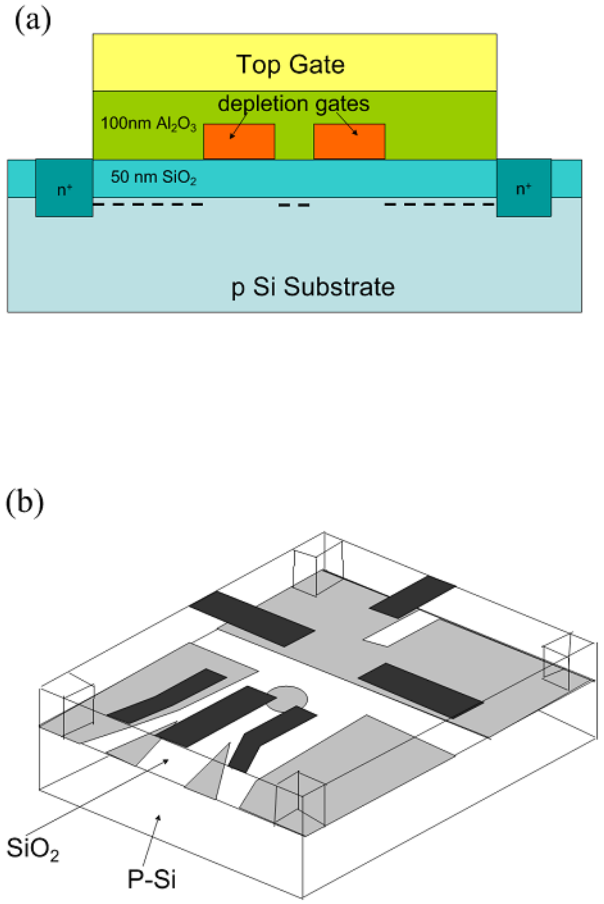

Figure 2.1: (a) Cross section view of a typical Si-MOS based lateral quantum dot device. (b) Three dimensional view of depletion gates layout and electric field at the interface of Si/SiO_2. The Al_2O_3 and top gate layout are removed for clarification. Only SiO_2/Si layer is shown. The black polygons on top of SiO_2 are depletion gates. The picture shown is a typical single dot. When negative voltages are added onto depletion gates, the resulting electric field will form a circular potential well seen as gray dot in the middle. Electrons can be trapped inside. The white regime at the interface are energy barriers for electrons. Large gray areas are the two dimensioanl electron reservoir which are connected to ohmic contacts.

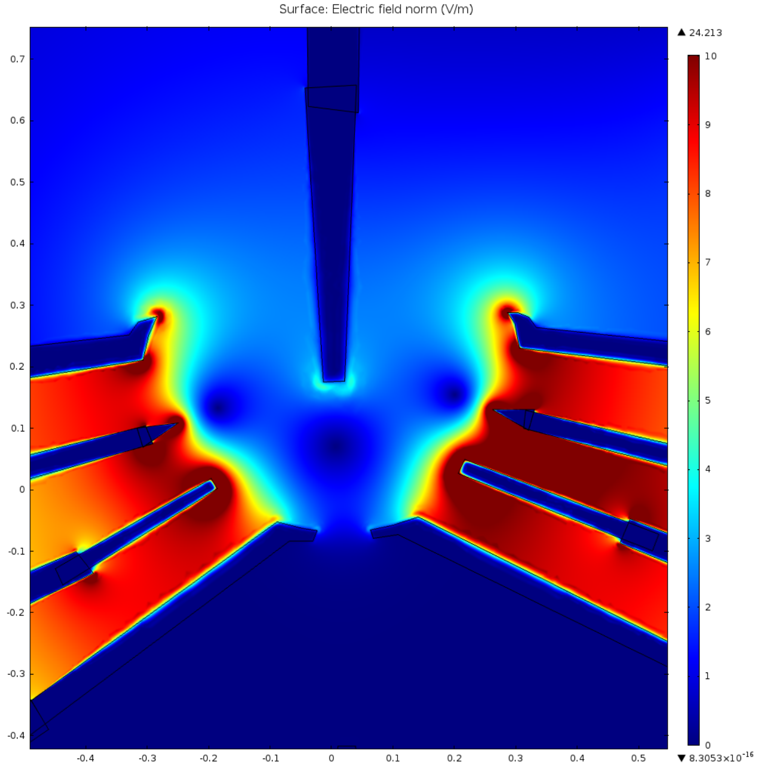

Figure 2.2: Comsol calculation of electrostatic field distribution of a circular triple quantum dot. Color bar illustrate the field strength distribution with red the highest and blue the lowest. The blue polygons are the depletion gates. The three blue field minima define the quantum dot locations.

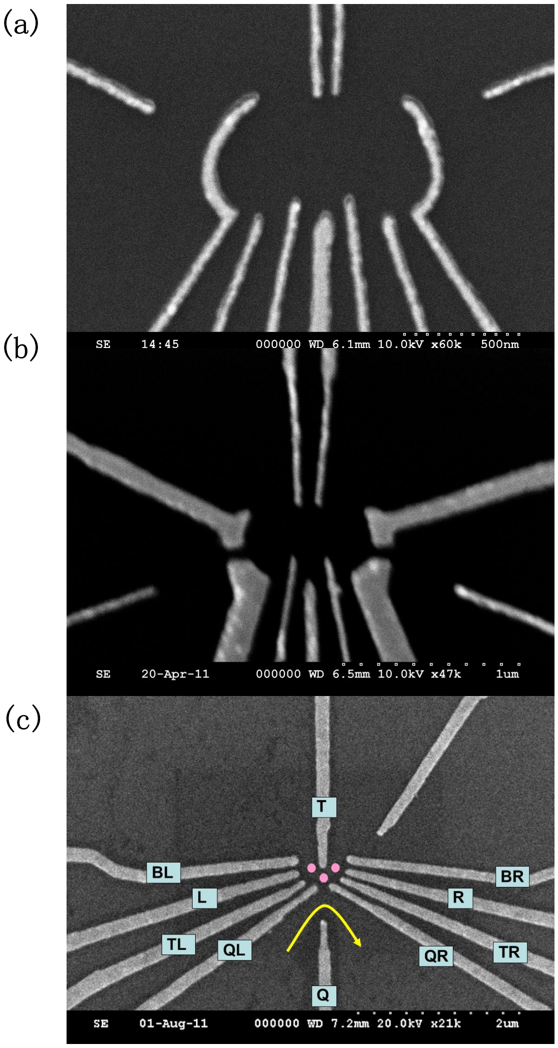

Figure 2.3: SEM image of triple quantum dot depletion gate layout. (a) Expansion of a common double quantm dot layout with two QPC channel integrated on either side. (b) Updated version of (a) with QPC channel completely separated from transport channel. (c) Design with three dots arranged in a circle and the QPC channel sitting nearby.

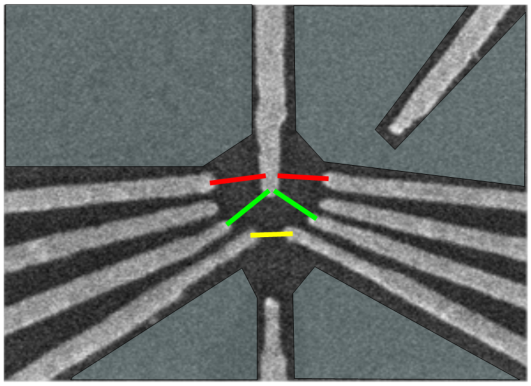

Figure 2.4: Zoom in of FIG. 2.3(c). The trasparent area is the two dimensional electron gas reservoir. Red lines mark the tunnel barrier between reservoir and dot. Green line marks the tunnel barrier between neighboring dots. Yellow line marks the size of the slot between dots and QPC channel

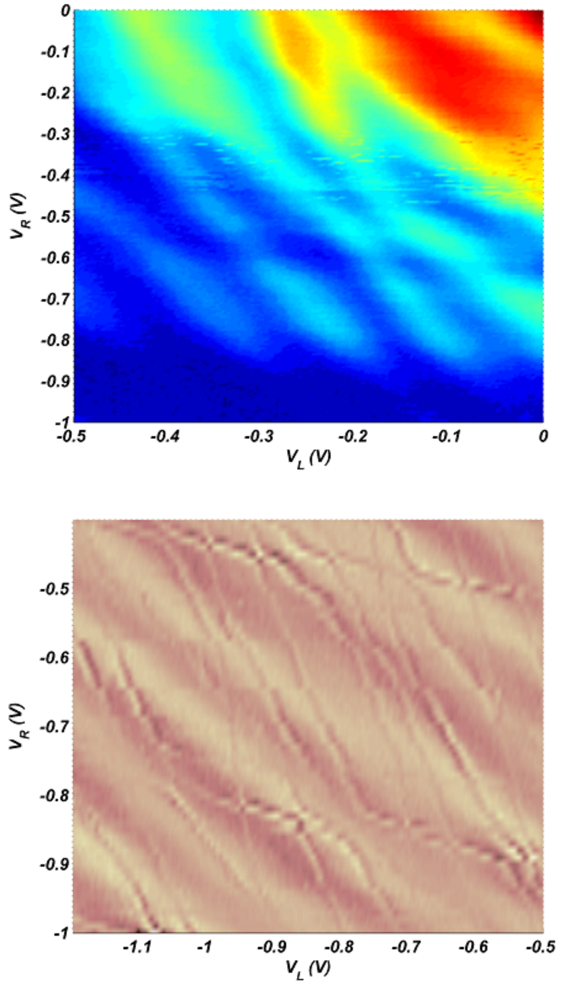

Figure 2.5: Device screening comparison at different temperatures. (a) Transport diagram through the quantum dot at 4.2K with large biasing triangle. (b) Charge sensing stability diagram at 300mK with organized charge sensing signal.

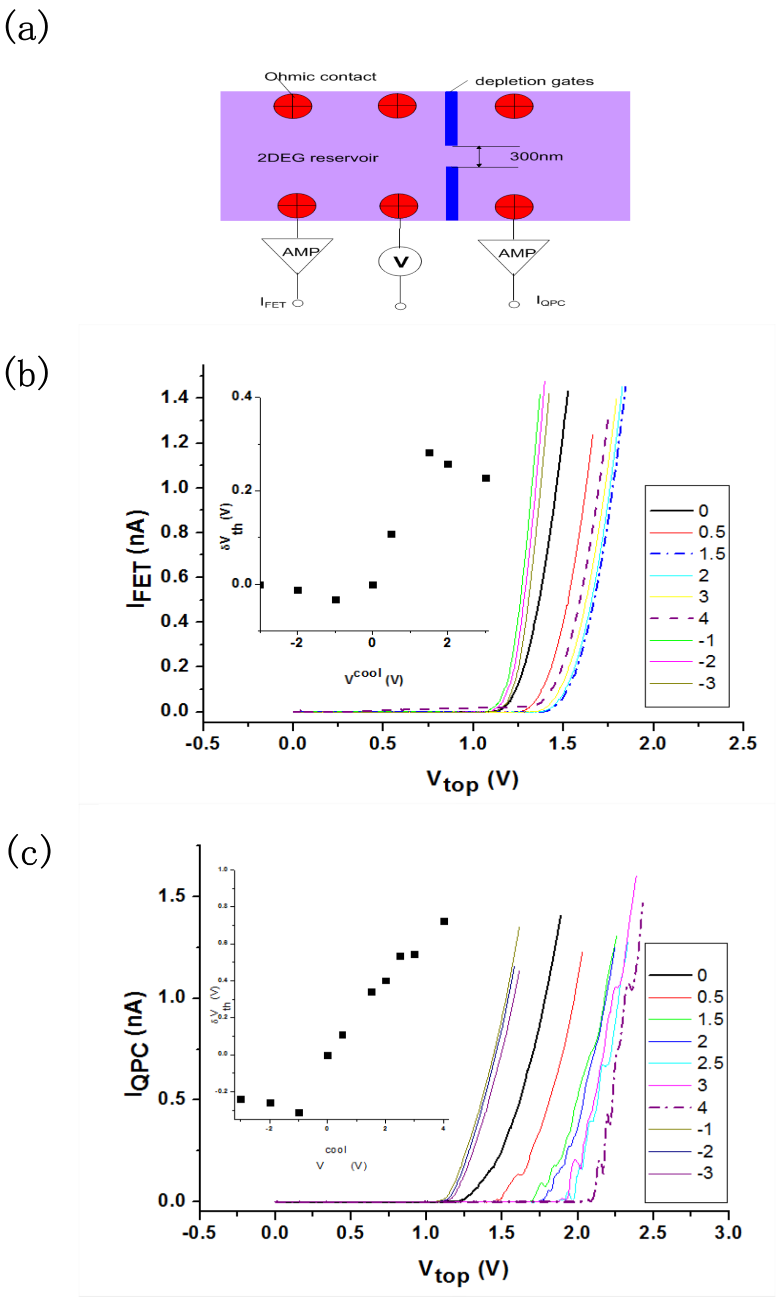

Figure 2.6: Bias cool down effect on device threshold voltage and turn on curve. (a) Schematic layout of device used for bias cooling study. The violet rectangular signifies the two dimensional electron gas reservior. The red crosses are the ohmic contacts. The two blue bars are depletion gates that forms a 300nm jucntion. The current between low left two ohmic contacts measuring the normal FET behavior while the current between low right two contacts measuring the quantum point contact channel. (b) The turn on curve for the normal FET under different bias cooling conditions, the inset shows the threshold voltage change with different bias cooling voltage; (c) The turn on curve across the quantum point contact under different cooling bias, the inset shows threshold voltage change which is larger than for normal FET.

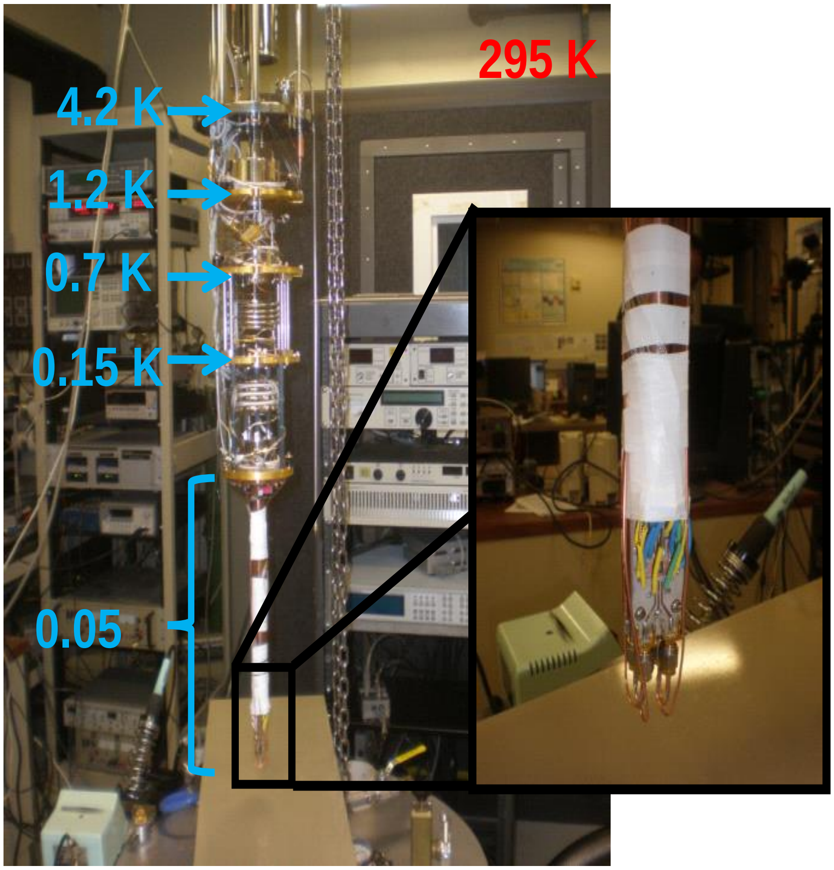

Figure 2.7: Janis 500 Dilution Fridge inset. Temperatures at different stages are marked. The zoom in picture shows the fridge tail with chip holder at the end.

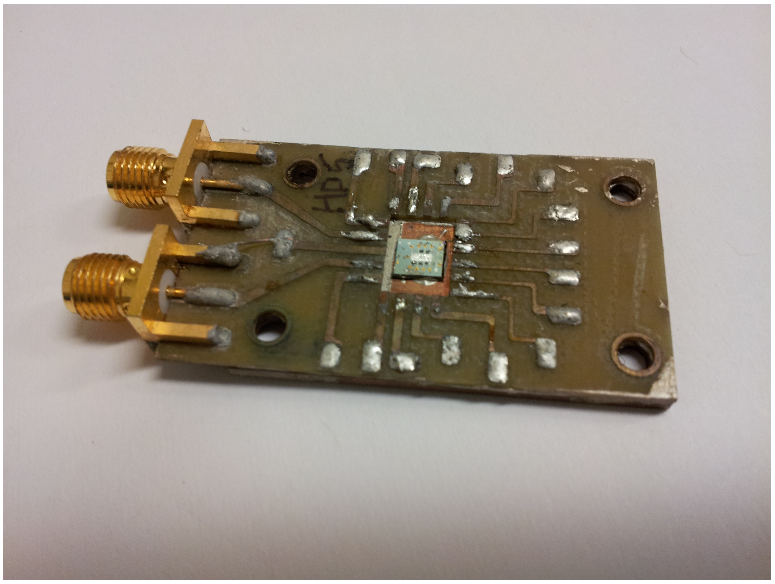

Figure 2.8: Chipholder with real device mounted, the data from Chapter 7 is was taken using this type of holder.

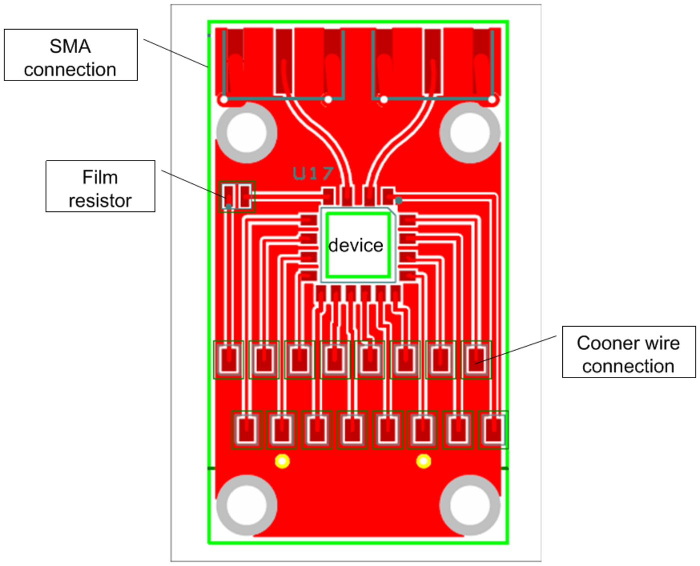

Figure 2.9: Chipholder designed for the purpose of minimizing crosstalk between different voltage transimission lines. The large green frame marks the border of the holder. The inner green rectangle specifies the device mounting area. Area painted with red color are conducting ground panel. The "Film resistor" marks the position for sordering surface mounted film resistor. The upper place is for sordering SMA connectors which are used for high frequency signal transmission.

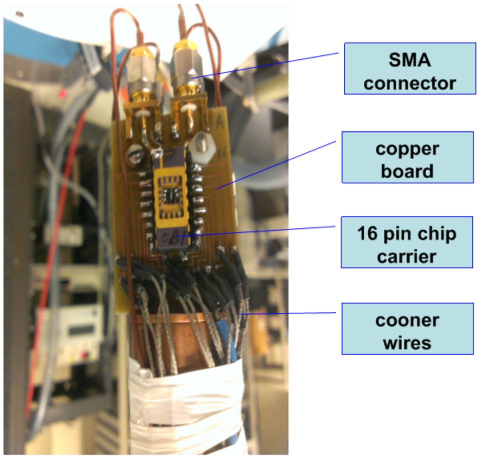

Figure 2.10: "Plug in" chip holder. The socket is directly mounted onto the copper board. The 16 pin carrier can be plugged into the holder directly.

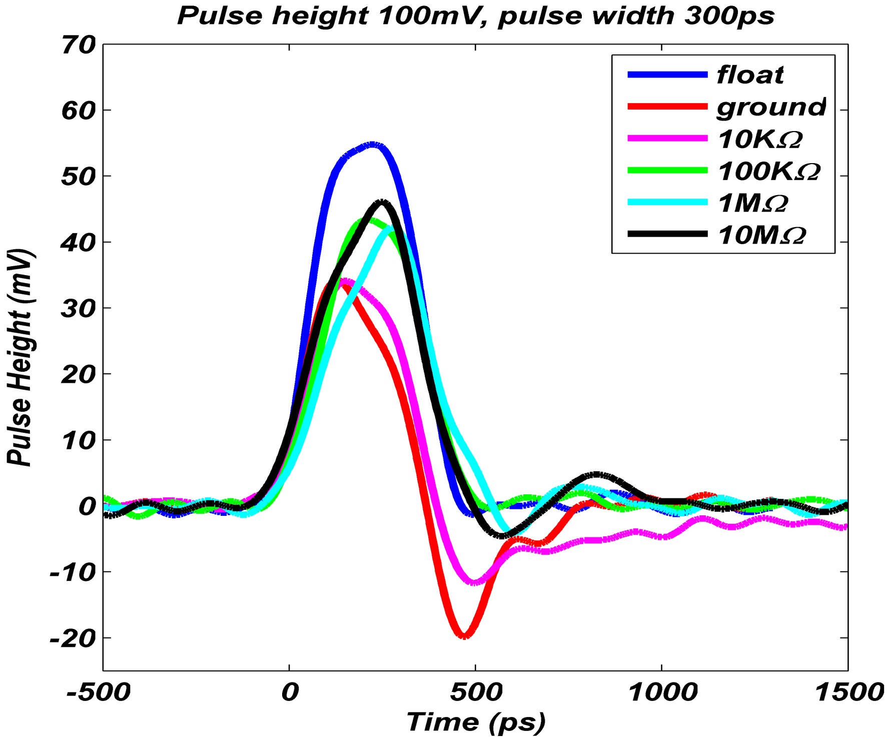

Figure 2.11: Pulse attentuation due to capacitive coupling between depletion gates and the top gate. The blue curves shows the pulse form when top gate is floated. The red curve shows a strong dip at the pulse down edge when top gate is grounded. The green curve, with 100kΩ surface film resistor between the top gate and the ground, has almost no shape deterioration.

CHAPTER 3

Characterization of Si MOS based quantum dot system

In this chapter, we will discuss various methods of characterizing Si MOS based quantum dot devices. I will first review the charge sensing method and present the experimental results from a double quantum dot device (MGH07A12). I will focus on extracting gate coupling strength, level arm α, and interdot tunnel coupling, t_c. This experiment is in collaboration with M. G. House [Hou12]. Then I will present transport and charge sensing measurement results on a triple quantum dot device (HD5) focusing on the magnetic field dependence. Last, I will briefly discuss the effective electron temperature extraction.

3.1 Charge Sensing and stability diagram

3.1.1 Device and measurement set up

Experiments discussed in this section is performed on a Si MOS based double quantum dot device. The device depletion gate layout is presented in FIG. 3.1. The dash circle marked the possible location of two dots. Gate RL and RR are the main plunger gates which tune the chemical potentials of dots while gate U tune the interdot tunnel coupling. Two quantum point contact (QPC) channel defined by gate RL(R), SL(R) and QL(R) serve the purpose of charge sensing. The QPC channel is sensitive to the local electric field change induced by the movement of charge in the quantum dot. This filed lines transmit through the slot (marked by yellow double arrow). The data shown below is collected by the right QPC channel.

In GaAs, the electron mean free path is long thus the electrons travel in the QPC without scattering.The quantum point contact channel can be described by discrete subbands and

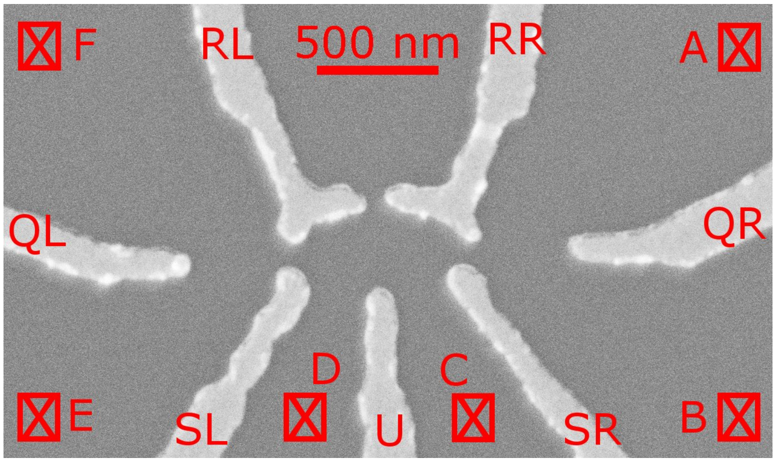

Figure 3.1: SEM image of depletion gate layout of a double quantum dot device. Two dash circles mark the possible locations of a double dot. RL, RR are plunger gate mainly tuning the chemical potential of dot. U change the interdot tunnel coupling. Two QPC channel integrated on both sides of the dot, defined by gate RL(R), SL(R) and QL(R).

exhbits quantized conductance plateaus. The mean free path of electrons at the $Si-SiO_2$ interface is around 30nm thus electrons experience significant scattering when passing through the junction between gate Q, QL and QR. This causes mixing between subbands and results in complicated oscillations in the conductance as a function of a depletion gate voltage. The sensitivity of the channel is determined by the derivative of the conductance. This causes the incontinuity of sensitivity. This problem can be solved by adding feedback loop to the charge sensing channel.

The charge sensing signal in dc current through the QPC is normally only 1 %. This can be easily smeared out by noise. We here use the modulation mode. A small sinusodial excitation, normally $1 \sim 2$mV is added onto one depletion gate. The excitation is normally called modulation. DC bias around 1mV is added to the ohmic contact on one side of the QPC channel, the current from the ohmic contact on the other side goes directly to the SR830 lock in amplifier. The lock-in amplifier will pick out the differential signal. The signal should be similar to numerical derivative of direct current. DC bias added onto QPC

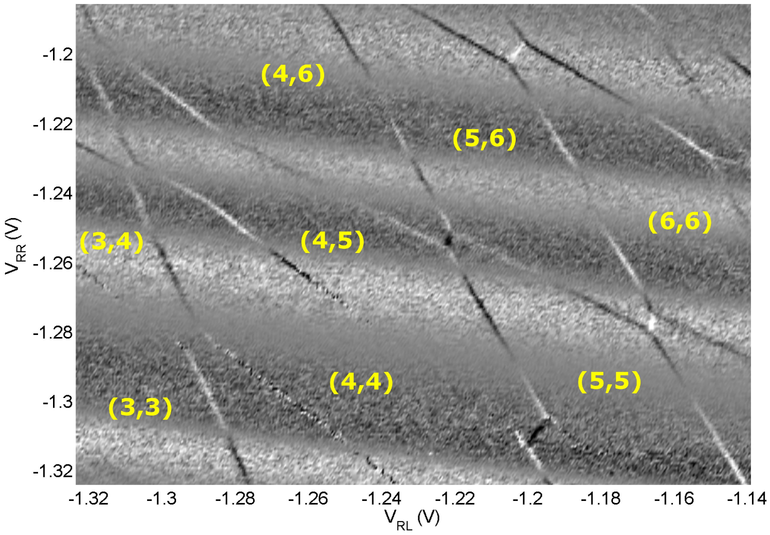

Figure 3.2: Stability diagram of a double quantum dot. Differential charge sensing channel conductance dI_{QPC}/dV_{RL} is recorded as a function of gate voltage V_{RL} and V_{RR}. The yellow numbers (N,M) indicate the possible electron number in left and right dot respectively.

can introduce shot noise. Thus one should be careful with it.

Using this method, we carried out the stability diagram of the double dot with SEM image in FIG. 3.1. The source and drain contacts of the transport channel, D and C, are grounded. The modulation is added onto PL gate to avoid direct impact on current in QPC channel. dI_{QPC}/dV_{RL} is recorded as a function of V_{PL} and V_{PR}. FIG.3.2 shows the result. We see two sets of parallel skinny lines. Those with larger slope are more sentive to the voltage change in V_RL signifing the charging events happened at left dot. The other set of lines describie electron move in/out of the right dot. The yellow number (N,M) describes the possible electron numbers in left and right dot respectively at certain voltage range of V_{RL} and V_{RR}. When charging lines with different slope are about to cross, the mutual capacitance C_m splits the cross points to two points, the triple points we talked before. The short line connecting the two points is called the inter dot transition line. These lines signify one electron shuffling between left and right dot. We will discuss the importance of this line later.

3.1.2 Stability diagram at non euqilibrium situation

When DC bias is added across source and drain contacts D and C, we would expect the triple points expand into biasing triangles in transport current. Similar feature should be seen in the charge stability diagram, [JPM05]. In their paper, the charge sensing signal is direct current measurement. Thus we see different triangle regimes with different colors. Here, we will present similar data using modulation measurement technique.

FIG.3.3 (a) shows the charge stability diagram for the charge transition (5,7) and (6,6) as seen in FIG. 3.2. A source drain bias V_{SD} is applied to contact D while contact C is grounded. FIG. 3.3 (c) and (d) shows the stability biagram under $V_{SD} \pm 0.27mV$. No obvious triangles are seen. If transport is possible at this charge transition, we would see positive biasing triangle if negative dc bias is added to contact D, seen in FIG.3.3(b). For generl purpose, assuming electron number is (M,N) at the low left corner. Inside the biasing triangle, the electron number changes as (M,N)-(M+1,N)-(M,N+1)-(M,N). Electrons normally tunnel very fast between dots. The current is determined by the tunneling rate Γ_L, tunneling between the left dot and D, and Γ_R, tunneling between the right dot and C. The charge sensing signal is a time ensemble averaging result. It gives the average electron number during time T_{lockin}. T_{lockin} is the time constant set by the SRS830 lock in amplifer. Thus the averaging number of electrons we detected inside the biasing triangle area is determined by the most opaque barrier. From FIG. 3.3 (c), we see the extension of left dot charging line disappear for the triangle. We determined Γ_L is very small. Similar analysis applys to FIG. 3.3 (d). FIG. 3.3 (e) and (f) is the same diagram of (c) and (d), except red lines are intentionally drawn to illustrate the bias triangle position.

3.1.3 Extract gate coupling strength: level arm α

One useful information we can get from the stability diagram at non equlibrium situation is to extract the depletion gate coupling strength. The gate coupling strength is determined as the ratio between the change of chemical potential of the dot, $\Delta\mu$, to a change in the gate

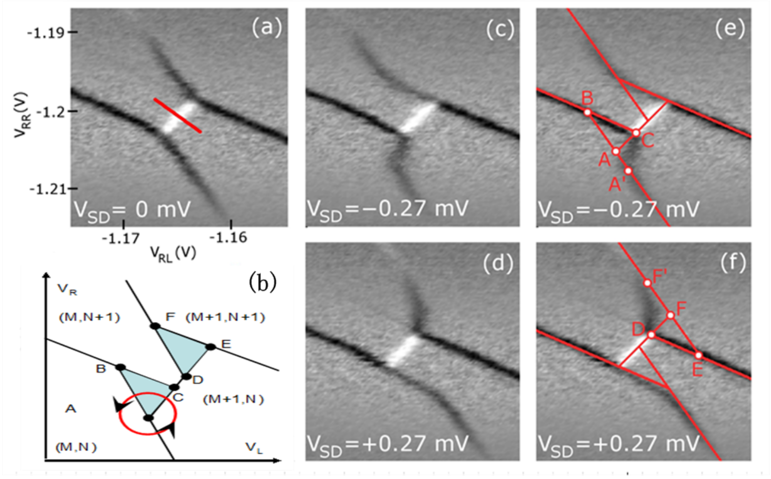

Figure 3.3: Stability diagram of a double quantum dot in a non equilibrium situation. (a) Stability diagram at charge transition (5,7) and (6,6) with $V_{SD} = 0$. (b) Illustration of transport biasing triangle with source drain bias. (c),(d) Stability diagrams at $V_{SD} \pm 0.27mV$. (e),(f) Same diagram as (c),(d) with red lines intentionally drawn for the biasing triangle

voltage ΔV. It is normally called level arm, represented by a quatity α. Knowing α can help us determing the absolute energy scale of the quantum dots.

When V_{SD} is applied, the size of the resulting biasing triangle is determined by the level arm α, [Wiel et al., 2002]. However, in their derivation, only the capacitance from plunger gate to the corresponding dot is considered. [House et al.,] improved the calculation by introducing the cross capacitance. The relation between chemical potential change and relative voltage change is defined as bellow:

$$\begin{pmatrix} \Delta\mu_L \\ \Delta\mu_R \end{pmatrix} = e \begin{pmatrix} \alpha_{LL} & \alpha_{LR} \\ \alpha_{RL} & \alpha_{RR} \end{pmatrix} \begin{pmatrix} \Delta V_L \\ \Delta V_R \end{pmatrix} \tag{3.1}$$

3.1.4 Extract gate coupling strength: level arm α

One useful information we can get from the stability diagram at non equlibrium situation is to extract the depletion gate coupling strength. The gate coupling strength is determined as

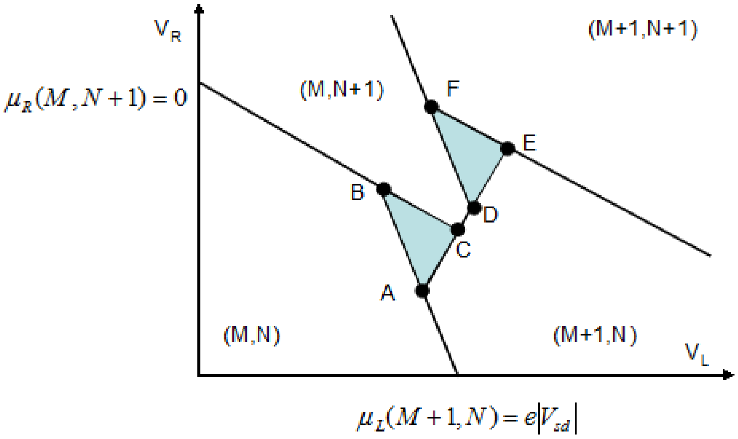

Figure 3.4: Illustration of biasing triangle for double dot with source drain bias V_{SD} present.

the ratio between the change of chemical potential of the dot, $\Delta\mu$, to a change in the gate voltage ΔV. It is normally called level arm, represented by a quatity α. Knowing α can help us determing the absolute energy scale of the quantum dots from the stability diagram.

When V_{SD} is applied, the size of the resulting biasing triangle is determined by the level arm α, [WFE03]. However, in their derivation, only the capacitance from plunger gate to the corresponding dot is considered. [HPX11] improved the calculation by introducing the cross capacitance. The relation between chemical potential change and relative voltage change is defined as bellow:

$$\begin{pmatrix} \Delta\mu_L \\ \Delta\mu_R \end{pmatrix} = e \begin{pmatrix} \alpha_{LL} & \alpha_{LR} \\ \alpha_{RL} & \alpha_{RR} \end{pmatrix} \begin{pmatrix} \Delta V_L \\ \Delta V_R \end{pmatrix} \tag{3.2}$$

We assign α_{xy} as the coupling between gate x(L or R) and dot y(L or R). FIG. 3.4 shows a positive biasing triangle. Along line AB, the chemical potential of left dot stays constant, while the chemical potential of right dot changed by $e|V_{SD}|$. This change is contributed by the sum of $\alpha_{LR} \cdot (V_L(B) - V_L(A))$. We can get similar equation for point D and C. Simple matrix calculations tells us the level arm matrix is:

$$\alpha_{LL} = \frac{\Delta V_{R2} V_{SD}}{\Delta V_{L2}\Delta V_{R1} - \Delta V_{L1}\Delta V_{R2}} \tag{3.3}$$

$$\alpha_{LR} = \frac{-\Delta V_{L2} V_{SD}}{\Delta V_{L2}\Delta V_{R1} - \Delta V_{L1}\Delta V_{R2}} \tag{3.4}$$

$$\alpha_{RL} = \frac{(\Delta V_{R2} - \Delta V_{R1}) V_{SD}}{\Delta V_{L2}\Delta V_{R1} - \Delta V_{L1}\Delta V_{R2}} \tag{3.5}$$

$$\alpha_{RR} = \frac{(\Delta V_{L1} - \Delta V_{L2}) V_{SD}}{\Delta V_{L2}\Delta V_{R1} - \Delta V_{L1}\Delta V_{R2}}. \tag{3.6}$$

In the above equations: $\Delta V_{L1} = V_L^{(C)} - V_L^{(A)}$, $\Delta V_{L2} = V_L^{(B)} - V_L^{(A)}$, $\Delta V_{R1} = V_R^{(C)} - V_R^{(A)}$, and $\Delta V_{R2} = V_R^{(B)} - V_R^{(A)}$

3.1.5 Interdot tunnel coupling

Now we want to focus on the interdot transition line. Crossing the interdot transition line, one electron tunnels between dots. If measuring the dc current through the QPC channel, we would expect a step function like change across the interdot transition line. Ref. [DLJ04] developed a model to descibe the physics at this regime. The ground state charge configuration across the interdot transition line can be written as two charge level (M+1,N) and (M, N+1). We define the detuning line as the line vertical to the interdot transition line. Along this detuning line, we define detuning ϵ as the energy difference between the chemical potential of the two charge states (M+1, N) and (M, N+1). The finite height of the potential barrier between the dots gives the tunnel coupling t_c. The tunnel coupling t_c mixed the two single particle state (M+1, N) and (M, N+1).The new ground state and excited states are superpositions of (M+1, N) and (M, N+1) states.They are separated by $\Omega = \sqrt{\epsilon^2 + 4t^2}$. If the QPC current responds linearly to the average excess charge on each dot, the direct sensor conductance for the change of this excess charge is:

$$g_{ls(rs)} = g_{ol(or)} \pm \delta g_{l(r)} \frac{\epsilon}{\Omega} tanh(\frac{\Omega}{2k_B T_e}) + \frac{\partial g_{l(r)}}{\partial \epsilon}\epsilon \tag{3.7}$$

The first term on the right is the background conductance of the QPC. The second term describes the linear response to average excess charge, and the third comes from the capacity coupling from depletion gates to the QPC. This should apply well to our system. In very small detuning range, we assume the last term is very small and set it to zero.

To get tunnel coupling, we first need to know the electron temperature T_e. Here, we can also utilize the interdot signal to extract T_e. When t_c is very small, the second term of 3.8 becomes $\delta g_l(r) tanh(\frac{\epsilon}{2k_BT_e})$.

We studied the transition at (5,7) and (6,6), seen as FIG. 3.3 (a). The tunnel coupling is very weak at this place which can be tell by the sharpness of the charging line transition [WFE03]. We extract the charge sensing signal along the red line, the detuning line. The detuning energy is calculated using the level arm matrix we got in last section. For the double dot device we studied, $\alpha_{LL} = 0.085, \alpha_{LR} = 0.044, \alpha_{RL} = 0.044$ and $\alpha_{RR} = 0.074$. Our raw data is recorded using modulation method, which is the derivative of QPC current. We first integrated the raw data into current. We use a quadruatic function to model the QPC background current, the first term in 3.8. By subtracting the first term, FIG. 3.5 plots the average excess electron number along the detuning line from (5,7) to (6,6). We use the model in equation 3.8 to fit the curve and found the electron temperature to be around 130mK. The red curve in FIG. 3.5 is the fitting curve with 130mK electron temperature.

Then we applied T_e to equation 3.8 and perform the same fitting to other transitions where tunnel coupling is stronger. FIG.3.6 shows the fitting result. The tunnel coupling t_c is extracted to be $60\mu eV$.

A very practicle purpose of extracting tunneling coupling is for qubit manipulation. For exchang-only qubit, the exchange interaction which originates from the tunnel coupling provides the rotating axis on Bloch sphere. It is also important to have the ability of tuning tunnel coupling as seen in Ref.**??**. Unfortunately, we will not be able to collect valuable data on this double device. We suspect it is due to the dot geometry. The gate U mainly adjusts the overall chemical potential of both dot instead of controlling the interaction between the double dots.

In chapter 4, we will discuss another way to extract interdot tunnel coupling from the

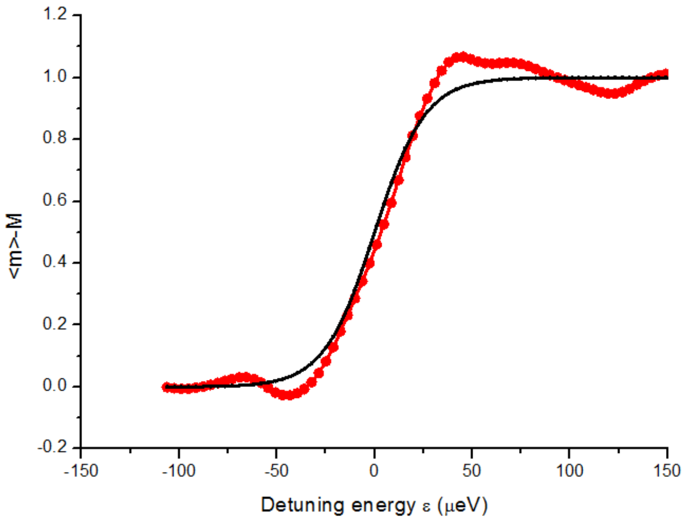

Figure 3.5: The red curve shows the excess charge in the right dot along the detuning line at fridge temperature of 65mK. The electron temperature T_e extracted from the fitting (black line) is 130mK.

curvature of the charging lines near the interdot transition using hubbard model.

Ref. [HST05] studied the field dependence of the anti crossing gap Δ. Δ is defined as the distance between two triple points in energy scale. At zero tunnel coupling. This gap is purely determined by the interdot coulomb repulsion. $\Delta = \sqrt{2}V_{12}$. While in the presence of t_c, $\Delta = V_{12} + 2t_c$. At high field, with the shrink of the wave function, the overlap induced tunnel coupling term will decrease till saturation. The difference between Δ at zero field and high field (2T in the reference) will give the value of tunnel coupling.

3.2 Characterization of a triple quantum dot device

3.2.1 Device fabrication and stability diagram

Similar to double dot device, here we present charge stability diagram for a triple dot device (HD5). The device fabricaiton process and opreation principles are the same as discribed in

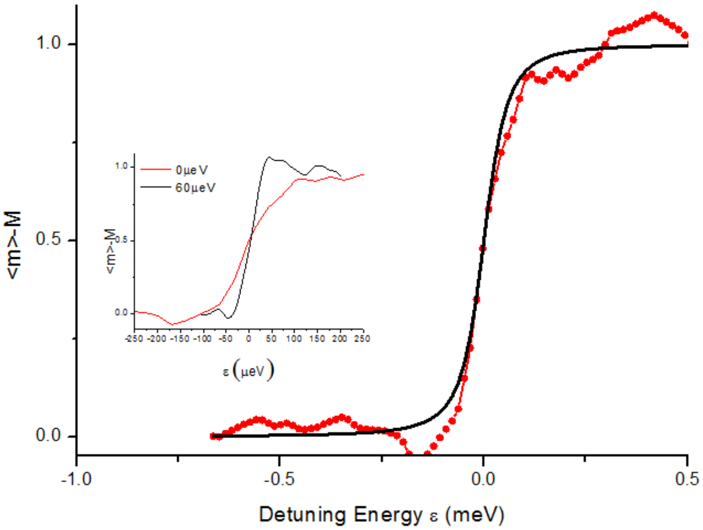

Figure 3.6: The red curve is the average excess electron $< m > -M$ in the left dot along the detuning line. The tunnel coupling $t_c = 60\mu eV$ is extracted by fitting using the black solid line. The inset plots the weak coupling and strong coupling charge transitions together for comparison

Chapter 2. FIG. 3.7 (a) illustrates the cross section view of the device and (b) shows the depletion gates layout for this device. The device was cooled in a He3 Fridge with a base tempreture of 330mK. A DC bias of .5 mV was applied across the charge sensing channel with a small 95HZ sinusoidal signa applied to V_R.The resulting modulated current dI_{qpc}/dV_R was collected by a SR830 lock-in amplifier. All other gates are biased to form appropriate potential for the triple quantum dot. FIG. 3.7 (c) shows the charge stability diagram in the voltage space of V_L and V_R. We identify the charging lines with specific dots by the slope of each line in the stability diagram, which indicates their relative dependence on V_L and V_R. Green and magneta lines are drawn for guidance representing the charging events happening at left and right dot, respectively, while blue lines represents that for the middle dot. The transition from (1,0,2) to (1,1,2) is hardly seen since the tunneling of electrons in/out of middle dot at these places is too slow to detect given the modulatio frequency. We scanned the plunger gate to very negative voltages and did not observe more charging events. The charging energy in each dot is estimated to be 3 $\sim$ 5meV for the last few electrons. We counted the electron numbers (N_A, N_B, N_C) from (0,0,0). The (1,1,1) regime is essential for the realization of exchange only qubit as we discussed in chapter 1. It also provides the possibility of creating the GReeberger-Horne-Zeilinger maximally entangled states, which is important for quantum teleporation. [NKL98].

3.2.2 Transport for triple quantum dot system and cotunneling

We also did transport measurement through a triple dot device. In principle, current can only be resolved when the energy levels in three dots are aligned with the Fermi level of source and drain. These are called the quadruple points. When bias is added across source and drian, things become more complecated due to the tridimensional nature of triple quantum dot. The triangle regime for current transport can be quadrangle. Ref.[BGG13]. presented the transport study at quadruple points (1,1,1),(2,1,1),(2,0,2),(1,1,2).

The transport current has to be larger than the noise floor to be detected. This requires the tunneling rates between dots and reservoir to be high enough. In our system, the noise floor is around 50 $\sim$ 100 fA. The tunneling rate has to be at least MHz. For device HD5, the tunnel barrier between dots and reservoir becomes so high that we were not able to see current in the last few electron regime. However, we observe transport current in another device near the last few electron regime. FIG. 3.8 shows the results. A .5mV bias is added across the source and drain contacts. In stead of the expected quadruple points, we see several pairs of biasing triangle. This is due to the cotunneling effect.

3.3 Field dependence of interdot transition line

In this section, we will explore the magnetic field dependence of the interdot transition line. FIG. 3.3 shows the charge stability diagram in (1,1,1) and (1,0,2) regime. This diagram is collected using modulation charge sensing method. A small sinusodial ac modulation is added onto gate V_R. A .5mV dc bias is added onto the QPC source side. The current from the QPC drain is collected by the lock-in and give the differential result dI_{qpc}/dV_R. We sit at the detuning $\epsilon = 0$ point and sweep the magnetic field in both direction. FIG. 3.3 shows the result. Supprisingly, the modulation current first increases slowly and then saturate in both direction while the field absolute value increase from zero to 100mT. The absolute change of the modulation current is about 1/4. We suspect this change is related with the singlet triplet mixing induced by hyperfine interaction near this regime.

Since the (1,1,1) regime is sufficient large, we believe we can treat the charge transition (1,1,1) to (1,0,2) as double dot (1,1) -(0,2). From the curvature of the charging lines near the interdot transition line, we estimated that the tunnel coupling is much larger than the random nuclear overhauser field. The corresponding energy levels across this interdot charge transition looks as in FIG.3.3. The ground state across the transition is the superposition of singlet S(1,1) and S(0,2) due to tunnel coupling mixing between middle dot and right dot. The triplet T(1,1) is splitted away by $J(\epsilon)$. At detuning $\epsilon = 0$, $J(\epsilon) = t_c$. The magnitude of the differential QPC current at $\epsilon = 0$ is proportional to the tunnel coupling t_c. As the field is increased, the triplet degenaracy is lifted. In silicon, g factor is 2. The new energy spectrum along the detuning is shown in FIG.3.3. The hyperfine interaction mixs the T_- and the singlet state. In Silicon, this mixing is very small due to the natural dedundcy of nuclear spin. Ref.[MBH12] claimed in their measurement, the nuclear fluctuation is only $\sigma_{HF} = 3neV$.Thus the anticrossing gap is around 3neV. And the ground state of the system in (1,1) side is triplet state.

As stated before, the differential QPC current is sensitive to the charge distribution near detuning $\epsilon = 0$ point. The charge distribution across the interdot transtion regime is reflected in the direct QPC current in the following form:

$$g_{ls(rs)} = g_{ol(or)} \pm \delta g_{l(r)} \frac{\epsilon}{\Omega} tanh(\frac{\Omega}{2k_B T_e}) + \frac{\partial g_{l(r)}}{\partial \epsilon} \epsilon \tag{3.8}$$

Thus the modulation current at $\epsilon = 0$ can be calculated by taking derivative of equation 3.8. $(dI_{QPC}/d\epsilon)_{\epsilon=0} = A + \frac{B}{16t_c} tanh(\frac{t_c}{k_B T_e})$. A and B are constant and in our case. B is positive.

Since the charge sensing modulation frequency is very slow, .085 $\sim 1kHz$, the electron will always move adiabatically and stay on the ground state. The charge distribution near the detuning point is different when field is added. Thus dI_{QPC}/dV_R will be different. dI_{QPC}/dV_R shows an increase in our data. We think this is due to the much smaller anticrossing gap from nuclear mixing than the interdot tunnel coupling. The first one is only fiew neV while the interdot coupling can be several μeV .We calculate this two situations with different gap by assuming $t_c = 5\mu eV$ and σ_{HF}=$2neV \times \frac{1}{16t_c} tanh(\frac{t_c}{k_B T_e})$ shows the nuclear mixing is 1.0494 times tunnel coupling. This might explain why we see an increase of dI_{QPC}/dV_R.

In double dot transport experiment, similar effect has been observed [KFE05]. In their strucure, the hyperfine induce leakage current at originally spin blocked regime and the leakage reach maxium when T_- and T_+ energy matches the singlet state. [SJP12] detected similar effect. They perform charge sensing by coupling a radio frequency lumped-element resonantor to a nanowire double dot. The resonator has a resonance frequency of 560.9MHz. In their experiment, the interdot transition signal disappears as field is increased which is opposite from our result. This is because the operation frequency they use is much higher than the energy gap thus the electrons are pulsed non adibatically across $\epsilon = 0$ point. Thus the system has higher probability of keeping the original charge configuration. The interdot transition lines gradually disappear when field is increased.

When field keep increasing, the change in differential current saturate. In principle, it should decrease as the mixing point will move to (2,0) site. However, we don't have data at larger field. We also didn't include the electronic temperature effect. This data was collected in a He3 fridge with base temperature of 300mK which equales to $26\mu eV$. The high effective electron temperature tends to smear out th field effect. The saturation point should be where the T_- cross the singlet at $\epsilon = 0$. From $t_c = g\mu_B B$, we estimated the interdot tunnel coupling t_c to be around $5\mu eV$.

3.4 Measuring effective electron temperature

In some of our experiments, the quantum dot device is cooled in a Dilution Fridge with base temperature of 50 100mK. The device is mounted directed on the chip holder or in a 16pin chip carrier pluged into the chip sorket. The chip holder is mounted at the end of the cold finger. The cold finger is made of copper which attached tightly to the bottom of mixing chamber. It is hard to lower the temperature of the electrons in the two dimensional electron gas of the device and there are several reasons. First it is hard to get a good thermal conduction from the mixing chamber all the way down to the device. Second the noise in the system has to be small enough to prevent heating up the device. Even the lattice tempereature of the device is cold enough, the electrons in the two dimensional gas might still be hot. Thus it is essential to determine the effective electron temperature.

For a quantum dot system which tunnel couples to the source and drain reservoir, we normally can observe coulomb blockade oscillations when the charging energy of the dot is larger than the thermal excitation. The coulomb blockade peak width is determined by the thermal excitation energy and the tunnel coupling between the dot and the reservoir. This thermal excitation is determined by effective electron temperature, which is normally higher than the fridge temperature. One direct way of extract the T_e is to raise the fridge temperatureT_f and record when the coulomb blockade peak starts to broaden. The T_f at which the peak starts to broadern gives a very good estimation of T_e. We have to emphasize that the tunneling between the dot and the reservoir has to be tuned small to minimize broadening induced by the tunnel coupling.

Here we present the result of measurement on Device OB1 cooled in Janis 500 Dilution Fridge. The device SEM structure is the same as shown in chapter 2 as a circular triple quantum dot. We use the QPC channel to extract T_e. We applied a small current 45uV to the source of QPC bias. The current in the drain contact is collected to the SRS570 low noise amplifier and recored by Keithley multimeter. FIG. 3.13(a) shows the coulomb blockade peaks at different fridge temperatures. We choose this peak with small current and far from other peaks to satisfy the requirement of weakly coupled to the 2DEG reservoir. We raise the fridge temperature and see the peak gradually broadens. We can see at $T_e = 250mk$, there is an obvious broadening of the peak. and when fridge temperature keeps increasing, the peak gets larger. This allow us to estimat the electron temperature to be below 250mk, which corresponds to energy $21.7\mu eV$. We also tried to fit the coulomb blockade with guassian function and extracted the full width half maxium. We plot the result as a function of fridge temperature, FIG.3.13 (b). However, it does not follow the normal $3.5kT_e$ relation. Neither did the guassian function fit well. It might be because the QPC channel is more broad compared to normal quantum dot system and it forms a well defined multi quantum dots system thus the coulomb peak is more complicated. None the less, the 250mk upbound is still convincible.

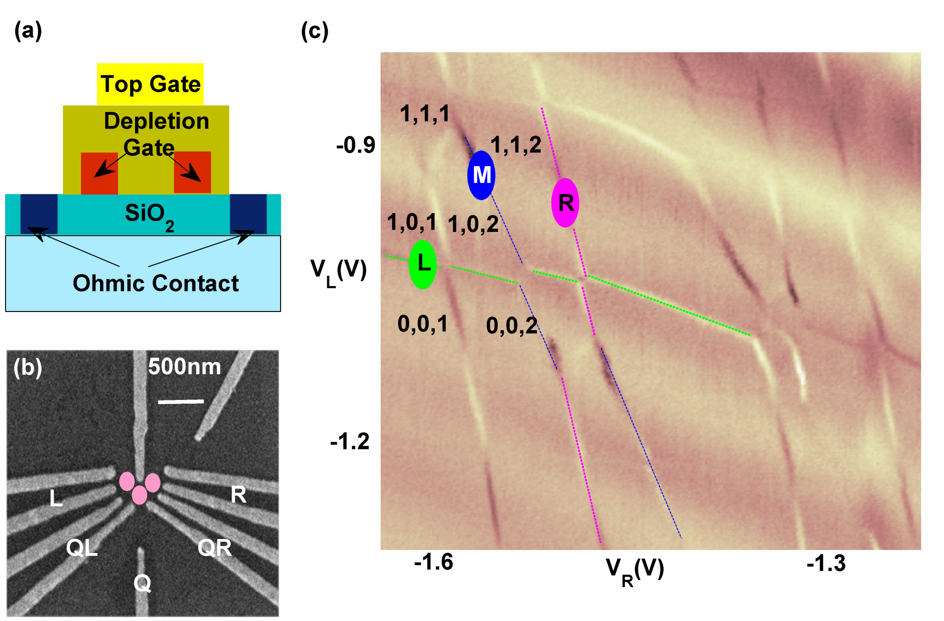

Figure 3.7: (a) Cross-section view of a Si MOS based triple quantum dot device. (b) Scanning electron micrograph of the depletion gate layout of a similar device with pink dots marking the locations of three dots. (c) dI_{qpc}/dV_R measured as a function of V_L and V_R at 330mK. Three sets of parallel lines are visible. Green, magenta, and blue lines are drawn for guidance, corresponding to addition of one more electron into left, right, and middle dot, respectively. The transition from (1,0,2) to (1,1,2) is hardly seen since the tunneling of electrons in and out of mddle dot at these places is too slow to detect given the modulation frequency. Electron number is counted and written in the sequence of left, middle, and right. The (1,1,1) regime is essential for the exchange-only qubit.

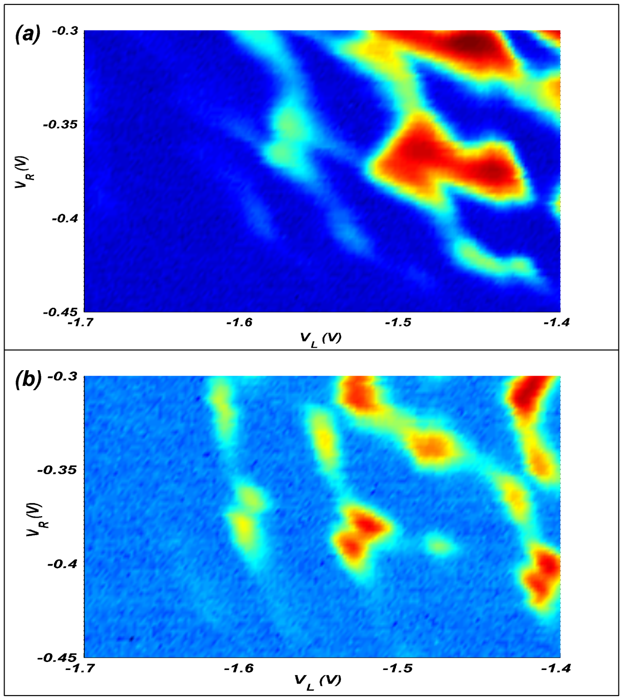

Figure 3.8: Transport diagram: current through a triple quantum dot as a function of plunger gate voltage V_L and V_R when source drain bias is added. The current is plotted in log scale, with red the highest, blue the lowest. (a) Vsd =0.5mV, (b) V_sd=-0.5mV

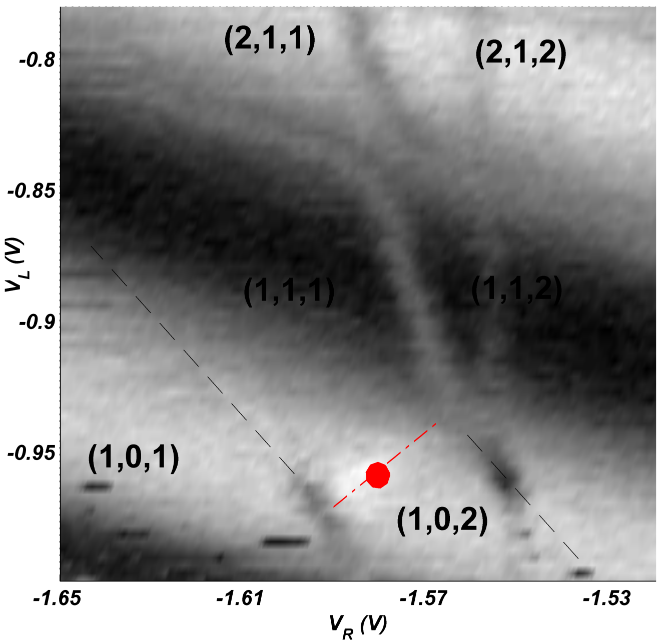

Figure 3.9: Charge stability diagram near transition of (1,1,1) and (1,0,2). The black dash line marks the position of middle dot charge transition line. At this place, the tunnelling rates is too low to be detected by the charge sensing channel. The red dash dot line marks the position of the interdot transition between (1,1,1) and (1,0,2). The red dot is the $\epsilon = 0$ position.

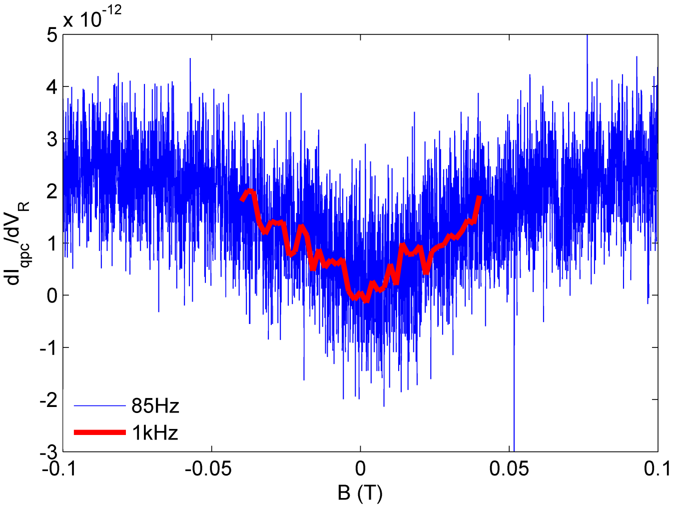

Figure 3.10: dI_{QPC}/dV_R at $\epsilon = 0$ as a function of external magnetic field. Blue curve is data taken at a modulation frequency of 85Hz. The red curve is taken at 1kHz. The red data is subtracted with a constant background to compare with the blue one.

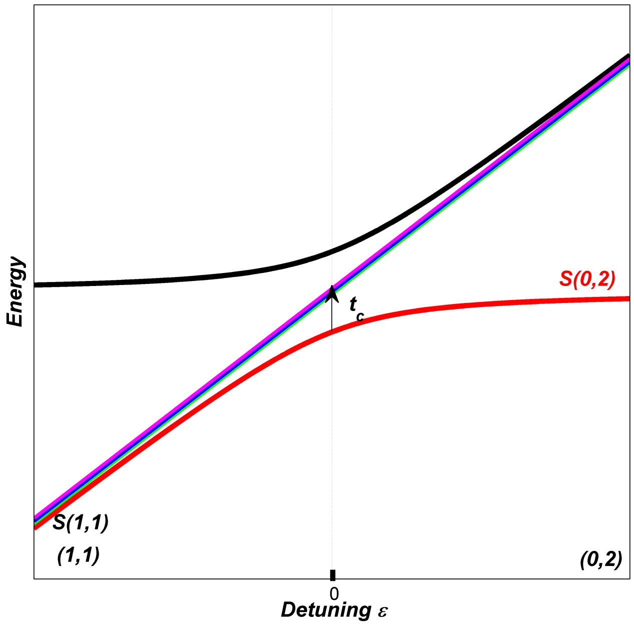

Figure 3.11: Singlet triplet energy levels near the transition between (1,1) and (2,0) as a function of detuning ϵ. S(1,1) mixes with S(2,0) due to the interdot tunnel coupling t_c. The triplet states T(1,1) are three fold degenerate as seen by the straght line.

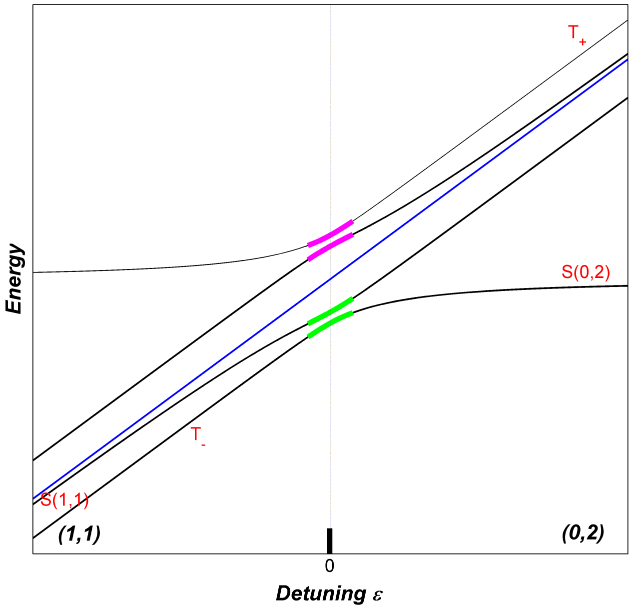

Figure 3.12: Energy spectrum as a function of Detuning ϵ in the presence of an external magnetic field. The triplet state degeneracy is lifted. T_- move downwards and mixed with the signlet state through small hyperfine interaction near detuning $\epsilon = 0$. The new states after mixing are marked by green lines. The same thing happen to T_+, which mix with the excited singlet state, marked by the magneta lines.

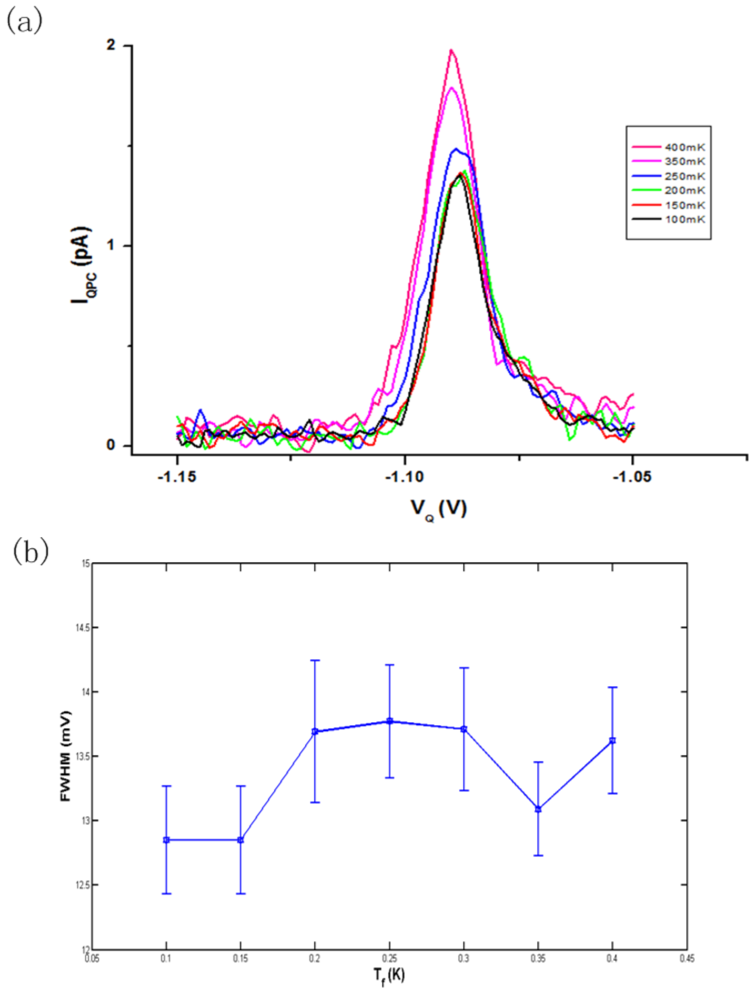

Figure 3.13: (a) Coulomb blockade peak at different fridge temperatures. At 250mK, the peak starts to broaden. The peak height also increases. (b) FWHM dependence on fridge temperature. It does not follow the typical $3.5kT_e$ relation.

CHAPTER 4

Constant interaction model and Hubbard model for double and triple quantum dot

The stability diagram is the most direct way to visualize the equilibrium charge state of a quantum dot system at certian depletion gate voltage configuration. By carefully analyzing the charge stability diagram, not only can we extract the charging energy, interdot coulomb repulsion but also the interdot tunnel coupling strength. In this chapter, we will first use constant interaction model to estabilish the relation between depletion gate voltage and charge configuration for both double and triple quantum dot system. We then extend the pure electrostatic model to hubbard model to include the quantum tunneling term. The well defined hubbard model helps us extract the tunnel coupling between dots. It also helps us understand the charge cofiguration evolution.

4.1 Constant interaction model

4.1.1 Double quantum dot

We first follow Ref. [WFE03] to establish the constant interaction model for a double quantum dot system. The double dot is modeled as a network of tunnel resistors and capacitors as seen in FIG. 4.1 (a). The number of electrons on dot 1(2) is $N_{1(2)}$. Each dot is capacitively coupled to a gate voltage $V_{a(b)}$ trough a capacitor $C_{1a(2b)}$ and to the source (S) or drian (D) contact through a tunnel barrier represented by a tunnel resistor $R_{L(R)}$ and a capacitor $C_{L(R)}$ connected in parallel. The dot are coupled to each other by a tunnel barrier represented by a tunnel resistor R_m and a capacitor C_m in parallel. In generalized case, for a system of N conductors. A capacitance can be defined between each conductor and every other conductor as well as a capacitance from each conductor to ground. The total energy of the system can then be viewed as the sum of total energies stored in the capacitors.

For a double dot system, the charge trapped inside each dot are $Q_1 = -eN_1$ and $Q_2 = -eN_2$ $(e > 0)$. The relation between Q and all exernal voltage can be written as following:

$$\begin{aligned} Q_1 &= C_L(V_1 - V_L) + C_{1a}(V_1 - V_a) + C_m(V_1 - V_2) \\ Q_2 &= C_R(V_2 - V_R) + C_{2b}(V_2 - V_b) + C_m(V_2 - V_1) \end{aligned} \tag{4.1}$$

Let $C_1 = C_L + C_{1a} + C_m$ and $C_2 = C_R + C_{2b} + C_m$, we can get the following:

$$\begin{pmatrix} V_1 \\ V_2 \end{pmatrix} = \frac{1}{C_1C_2 - C_m^2} \begin{pmatrix} C_2 & -C_m \\ -C_m & C_1 \end{pmatrix} \begin{pmatrix} Q_1 + C_LV_L + C_{1a}V_a \\ Q_2 + C_RV_R + C_{2b}V_b \end{pmatrix} \tag{4.2}$$

Then the total energy of the system can be calculated using the following equation:

$$U = \frac{1}{2}\vec{V} \cdot C\vec{V}. \tag{4.3}$$

In the case of equlibrium state, we set $V_L = V_R = 0$. For double dot, the total energy is:

$$\begin{aligned} U(N1, N2) &= \frac{1}{2}N_1^2E_{C1} + \frac{1}{2}N_2^2E_{C2} + N_1N_2E_{Cm} + f(V_a, V_b) \\ f(V_a, V_b) &= \frac{1}{-e}C_{1a}V_a(N_1E_{C1} + N_2E_{Cm}) + C_{2b}V_b(N_1E_{Cm} + N_2E_{C2}) \\ &= +\frac{1}{e^2}\frac{1}{2}C_{1a}^2V_a^2E_{C1} + \frac{1}{2}C_{2b}^2V_b^2E_{C2} + C_{1a}V_aC_{2b}V_bE_{Cm} \end{aligned} \tag{4.4}$$

In the above equation, $E_{C1(2)}$ is the charging energy of the individual dot 1(2), E_{Cm} is the electrostatic coupling energy, which is the change in energy of one dot when an electron is added to the other dot. These energies are in terms of capacitances as follows:

$$E_{C_1} = \frac{e^2}{C_1}(\frac{1}{1 - \frac{C_m^2}{C_1C_2}}), E_{C_2} = \frac{e^2}{C_2}(\frac{1}{1 - \frac{C_m^2}{C_1C_2}}), E_{C_m} = \frac{e^2}{C_m}(\frac{1}{\frac{C_1C_2}{C_m^2} - 1}), \tag{4.5}$$

The electrochemical potential $\mu_1(2)(N_1, N_2)$ is defined as the energy needed to add the $N_1(N_2)th$ electron onto the dot 1(2). Then we have:

$$\begin{aligned}
\mu_1(N_1, N_2) &= U(N_1, N_2) - U(N_1 - 1, N_2) \\
&= (N_1 - \frac{1}{2})E_{C1} + N_2 E_{Cm} - \frac{1}{|e|}(C_{1a}V_a E_{C1} + C_{2b}V_b E_{Cm}) \\
\mu_2(N_1, N_2) &= U(N_1, N_2) - U(N_1, N_2 - 1) \\
&= (N_1 - \frac{1}{2})E_{C2} + N_1 E_{Cm} - \frac{1}{|e|}(C_{2b}V_b E_{C2} + C_{1a}V_a E_{Cm})
\end{aligned} \tag{4.6}$$

At equlibrium condition, we assume the chemical potential of the source and drain to be zero. Thus in the voltage space V_a and V_b, when the chemical potential $\mu_{1(2)}$ equals zero, then one electron can be added onto dot 1(2). FIG. 4.1 (b) shows a simulated result with symmetric capacitance. The honeycomb feature is reproduced. Another way to calculate the stability diagram is to consider the electorn configuration (N_1, N_2) at voltage V_a and V_b which make the total energy $U(N_1, N_2)$ the smallest.

4.1.1.1 Cross capacitance

In the above model, we only consider the capacitance from depletion gate to its designated dot. However, in the real deivce, the change of any depletion gate voltage will inevitablely affect other dot potential. We modify the above model by adding a cross capactance. Thus FIG. 4.1 (a) becomes FIG.4.2.

By including cross capacitance, Eq. 4.1 is modified to:

$$\begin{aligned}
Q_1 &= C_L(V_1 - V_L) + C_{1a}(V_1 - V_a) + C_m(V_1 - V_2) + C_{1b}(V_1 - V_b) \\
Q_2 &= C_R(V_2 - V_R) + C_{2b}(V_2 - V_b) + C_m(V_2 - V_1) + C_{2a}(V_2 - V_a)
\end{aligned} \tag{4.7}$$

We can then replace $C_{1a}V_a$ with $C_{1a}V_a + C_{1b}V_b$ and $C_{2b}V_b$ with $C_{2b}V_b + C_{2a}V_a$ to get the new total energy. Similarly, we plot out the stability diagram considering the cross capacitance. FIG.4.3 shows the stability diagram change as we gradually increase the cross capacitance. From (a)-(b), we turn on the cross capacitance from gate a to dot 2 while from (c)-(d), cross capacitance from gate b to dot 1 is studied. Simulation parameters can be found in the

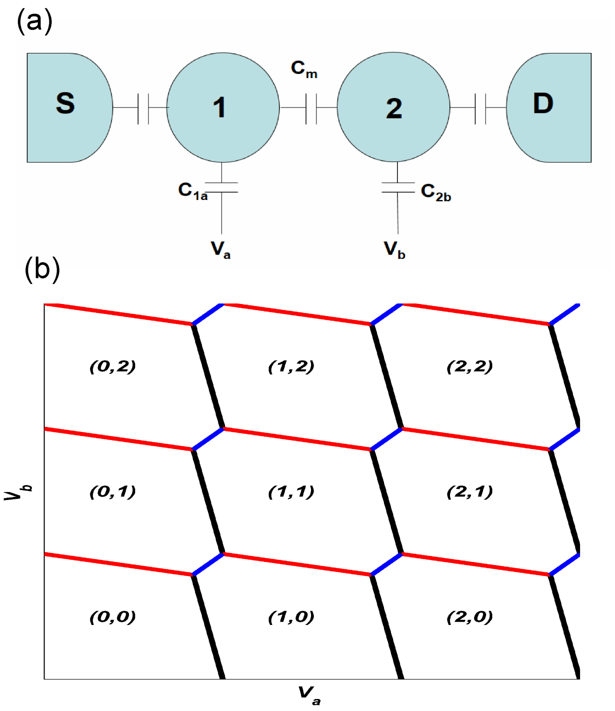

Figure 4.1: (a) Network of tunnel resistors and capacitors representing two quantum dots coupled in series. The different elements are explained in the tex. (b) Calculated stability diagram based on constant interaction model. Honeycomb pattern is clearly seen. The equlibrium charge on each dot in each honeycomb domain is denoted by (N1,N2).

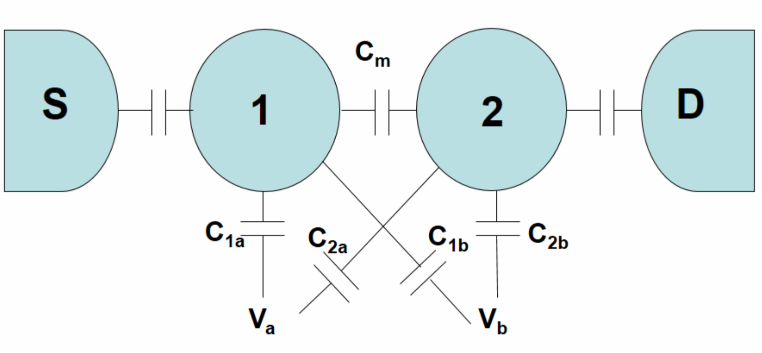

Figure 4.2: Network of tunnel resistors and capacitors representing two quantum dots coupled in series. Cross capacitance C_{1b} and C_{2a} are included

figure caption. The red lines are the charge transition lines with cross capacitance added. The blue dash lines are those without cross capaitance and are plotted for comparison. As can be seen, the cross capacitances greatly change the overal honeycomb diagram shape. And the interdot transition line slope can totally change from positive to negative. This signature can help us identify the cross capacitance from experimental diagram.

4.1.2 3D stability diagram for triple quantum dot

We extended the capacitive model to a triple quantum dot. We develop the model according to the formula in Ref.[SGG07]. Detail equations and algorithm can be found in this paper. The algorithm is similar to the double dot case. We try to find out the electron configuration which has minimum total energy under certain voltage settings. Now we have three dots: 1, 2 and 3 linearly arranged. Pluger gate a, b and c are capacitively coupled to dot 1, 2 and 3 respectively. Coupling between two dots are assigned asC_{12}, C_{23}, and C_{13}. Cross capacitance is also considered. The full characterization needs to be done in three dimensional voltage space since we now have three independent dots. To simplify the explaination, we first fix the middle plunger gate voltage and only scan in two dimesional voltage space. FIG. 4.4 shows a two dimensional simulation result. We can see three sets of parallel charging lines which magnifest the charging evens in each dot. We also see triple points similar to those in double dot. These triple points means the energy level in two dots are on resoance. One intriguing feature is the pentagon. This is due to the triple dot interaction nature. In a three dimensional voltage space, every charging line will become plane and the petagon we see is the projection of the different plane intersection onto a certian 2D plane.

To fully characterize the system, we have to calculate the electron configuration with minimum total energy in a three dimensional voltage space. FIG. 4.4 shows the simulation result with a symmetric capacitance setting. As can be see, the original charging lines evolves into charging planes. At places where three planes intercet each other is called the quadruple points. At this point, four charge configurations have same total energy and electrons or holes can tunnel through the dot. In Chapter 5, we will present experimental oberservation

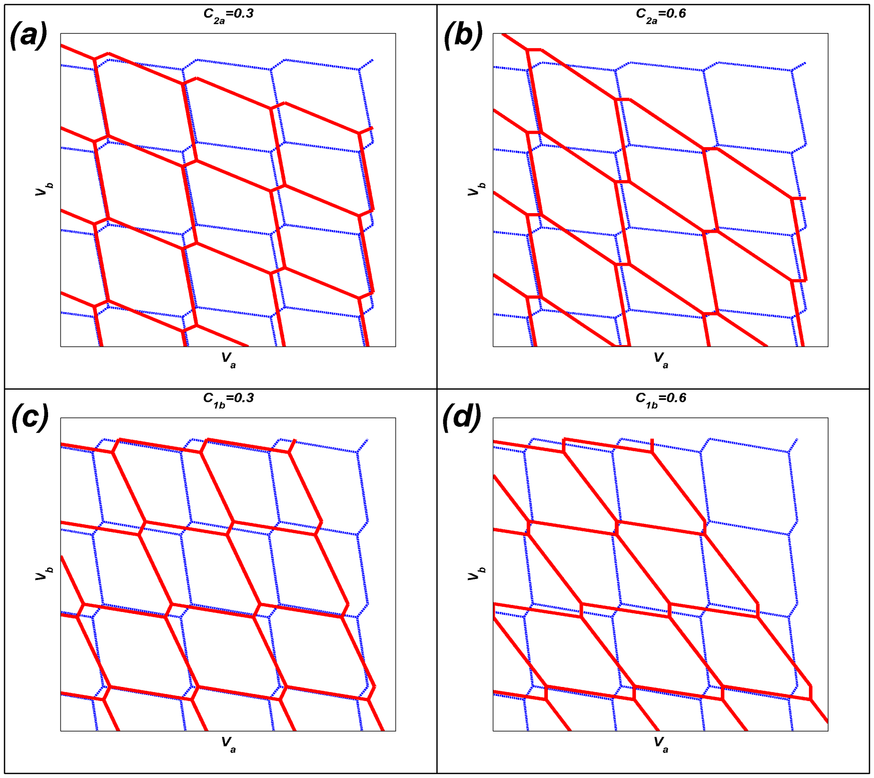

Figure 4.3: Stability diagram calculated using constant interaction model with cross capacitance included. In the simulation, we set $C_{1a} = C_{2b} = 1$, $C_L = C_R = 0.1, C_m = 0.2$. (a)-(b), cross capacitance from depletion gate a to dot 2, $C_{2a} = 0.3$ and 0.6. (c)-(d) cross capacitance from gate b to dot 1. The blue dash honeycomb diagram is with zero cross capacitance.

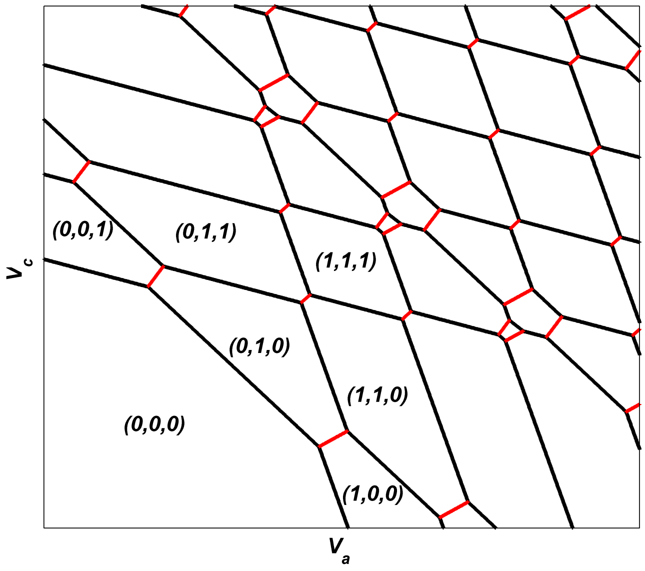

Figure 4.4: Triple dot stability diagram characterized in two dimensional voltage space. The central dot voltage V_b is fixed. Three sets of parallel lines can be seen. A typical pentagon area where three charging lines with different slope starts to cross is seen. Electron number is marked for charge stable regime as (N_1, N_2, N_3)

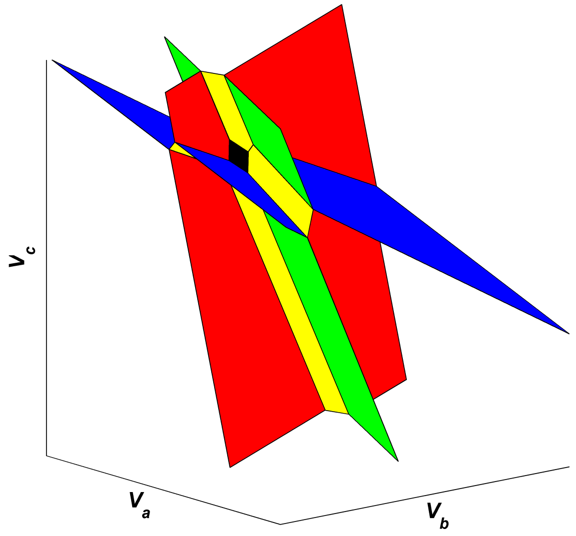

Figure 4.5: Triple dot stability diagram characterized in three dimensional voltage space. Red, green and blue planes are charging planes where by crossing these planes means loading or unloading electron from dot 1, 2 or 3. The yellow planes represents the interdot transition regime. At these planes, neighboring charging configurations share same energy.The small black area is where three planes start to cross. The petagon shape we see on FIG.4.4 is its projection on to plane voltage place of V_a and V_b. Parameters used for this simulation: $C_{1a} = 0.75, C_{1b} = 0.2, C_{1c} = 0.1, C_{2a} = 0.2,$ $C_{2b} = 0.75, C_{2c} = 0.2, C_{3a} = 0.1, C_{3b} = 0.2, C_{3c} = 0.75$ and $C_{12} = C_{23} = 0.5, C_{13} = 0.25$.

of quadruple points. In this figure, for clarity, we only include few planes. If we increase the voltage range, we will see parallel planes similar to the parallel charging lines for double quantum dot.

4.1.2.1 Cross capacitance in triple quantum dot

Similar to double dot, we should consider cross capacitance when simulate triple quantum dot stability diagram. Here, we have in total six cross capacitance. FIG.4.6 shows the corresponding stability diagram shape change. FIG.4.6 (a) use the same parameters as in

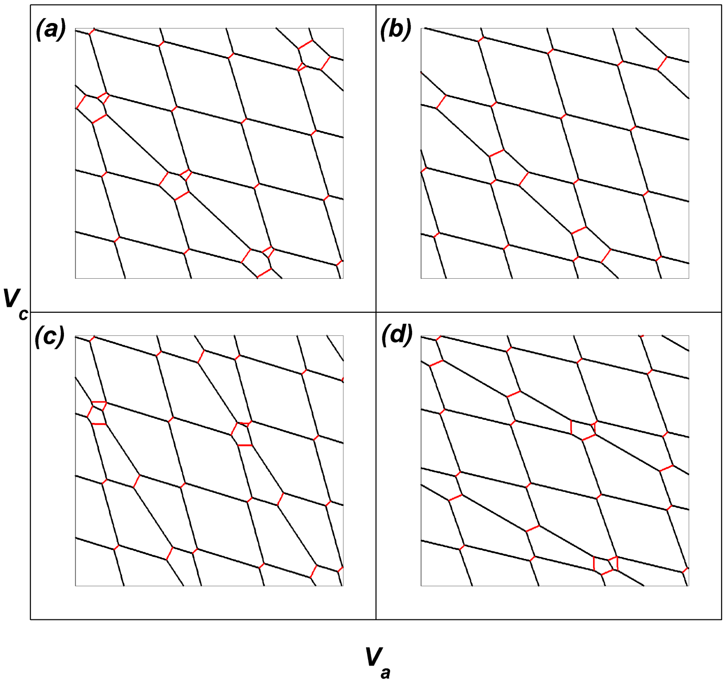

Figure 4.6: Cross capacitance effect on triple dot stability diagram. (a) Same parameter used as in FIG.4.5; (b) $C_{3b} = 0.5$; (c) $C_{2a} = 0.4$; (d) $C_{2c} = 0.4$

FIG.4.5. In FIG.4.6 (b), we set $C_{3b} = 0.5$ which means change plunger gate b also change chemical potential of dot 3. However, we didn't see much change in the diagram. This is due to we are scanning voltage space V_a and V_c with V_b fixed. Thus the change of the middle dot charging plane in three dimension dosn't significantly change its projection. In FIG.4.6 (c) and (d), we set $V_{2a} = 0.4$ and $V_{2c} = 0.4$ respectively, we see the middle dot charging line tilt corrspondingly. This is similar to what we observed in double dot. Cross capacitance dramatically change the stabiltiy diagram shape.

The cross capacitance can be understood as the dots are no longer located at the designated area. This might be due to unexpected charge imurity in device or the" not well lift off" depletion gate which modifies the local potential well profile. The cross capacitance means we lose independent control over quantum dot. By fitting experimental diagram, we can get estimation of cross capacitance magnitude. It help us understand certain phenomena of the device. In Chapter 5, we will discuss the quadruple points tuning of a triple quantum dot device. There, we will show that the large cross capacitance prevents us from observing six quadruple points while we only see two quadruple points.

4.2 Hubbard model for double quantum dot

Overall, the constant interaction model reproduces the stability diagran. However, it has it own limitations. There is no quantum effect included. For the purpose of qubit manipulatioon, understanding the spin dynamics and exchange interaction is crutial. Generalized hubbard model gives the possibility of studying the quantum fluctuation effect on the stability diagram. The hubband model consists of a lattice of 'site', plus a set of electrons that can hop around between neighbouring sites. Each electron has a spin that can point up or down. A site can accommondate zero, one, or two electrons. When electrons are on the same site, they much have oppsite spin to obey the Pauli exclusion principle. Also, two electrons of opposite spin occupying same site will result in charge energy. In the case of a double quantum dot, we can assume the double dot as two sites in the frame of hubbard model. To simplify the situation, we only consider the lowest lying orbital state for each quantum dot. Each quantum dot can have up to two electrons. We will calculate the charge configuration from (0,0) to (2,2). This is also the charge configuration which is important for qubit manipulation. For many electron quantum dot, we can make the assumption of closed shell and only consider the valence electron.

Ref. [YWS11] provided the generalized hubband model hamiltonian:

$$H = H_\mu + H_t + H_U + H_J \tag{4.8}$$

where H_μ is the chemical potential of the system which is a function of the depletion gate voltages. H_t is the hopping term which keeps the electron spin during transfering between dots. H_U has two parts. One is the intradot coulomb repulsion which can also be understand as the charging energy of the dot. Second comes from the interdot coulomb repulsion. The last term H_J includes spin-exchange, pair hopping and occupation-modulated hopping term which is neglected at first level approximation. The simplified hamiltonian looks like below:

$$H = \sum_{ij\sigma}(\mu_i\delta_{ij} + t_{ij})C^{+}_{i\sigma}C_{j\sigma} + \sum_{i} U_i n_{\uparrow i} n_{\downarrow i} + \sum_{i\neq j} V_{ij} n_i n_j; \tag{4.9}$$

To calculate the stability diagram in the voltage space, we need to find out the charge configuration which has the lowest total energy at certainl plunger gate voltage. Most of the parameters can be extracted from the experimental diagram. As long as we know the level arm matrix for the double dot, we can convert any voltage difference in stability diagram into energy. The charging energy of two dots can be read directly from the experimental diagram as the distance between parallel charging lines. The distance between two triple points gives interdot coulomb repulsion $\sqrt{2}U_{12}$. The tunnel coupling cannot be grabbed directly from the experimental diagram. We assume $t : 0 \sim 500\mu eV$. The chemical potential $\mu_i (i = 1, 2)$ is a complex function of applied depletion gate voltage and the geometry of the quantum dot. In our simulation, since the constant interaction model have reproduced the main feature of the charge stability diagram, we assume the chemical potential of the each dot $\mu_i (i = 1, 2)$ is linearly depending on the two pluger gate voltage as follow:

$$\mu_i = \alpha_i V_L + \beta_i V_R + \gamma_i; i = 1, 2; \tag{4.10}$$

In Ref. [YWS11], they compare this linear relation directly with basic constant interaction model and get the following relation:

$$\begin{aligned} \alpha_1 &= (U_2 - U_{12}) * U_1/(U_1 * U_2 - U_{12} * U_{12}); \beta_1 = 1 - \alpha_1 \\ \alpha_2 &= (U_1 - U_{12}) * U_1/(U_1 * U_2 - U_{12} * U_{12}); \beta_2 = 1 - \alpha_2 \end{aligned} \tag{4.11}$$

However, this conclusion is based on the assumption of not considering cross capacitance. We extract α_i and β_i from the slope of the charging lines from the charge stability diagram. $\gamma_i, i = 1, 2$ is half of charging energy $U_i, i = 1, 2$.

The Hamiltonian of the hubbard model is a 16×16 matrix in general. However, it can be block diagonalized according to the total electron number and total spin N, S_Z. Here we just presents the simulation result. We first try to reproduce the stability diagram without the hopping term. FIG.4.7 (a) shows the calculation when cross capacitance is not considered. We set $U_1 = U_2 = 10meV$, $V_{12} = 3meV$, $t = 0$. The diagram resembles the constant interaction calculation result well as expected. The only difference is that now we assgin different charge configuration regime with different color instead of just plotting the charge transition lines. The next step is to study the tunnel coupling effect on the stability diagram. FIG. 4.7 (b)-(f) illustrate the gradual change of stability diagram when tunnel coupling is steadily increased. The charging lines near the anticrossing become curved. Also the color is smoothly changed across the interdot charge transition regime. This means at these voltage settings, the lowest energy state is the superposition of two charge states. We plot out the QPC magnitude along the detuning line across the interdot transition line in FIG.4.8. All the parameters used for this calculation can be found in figure caption.

In Ref. [YWS11]. the author claimed in principle, we can read tunnel coupling directly from the stability diagram given enough resolution. However, from the above simulation, we found that it is impossible. The experimental charging lines are broaden by effective electron temperature. Thus exact extraction can not be done. However, this model should give a good estimation about the range of tunnel coupling. FIG.4.9 (a) gives the experimental double dot stability diagram. Here, we only show one anticrossing. We see charging line between (0,0) and (0,1) is much more tilted than the charging line between (0,0) and (1,0). This means the cross capacitance from V_a to right dot is not negligible. The white lines are the charge transition line while the black line represents the interdot transition line. We can see near the anticrossing, the white charging line become curved which signified the interdot tunnel coupling is not negligible. The right part shows the experimental diagram superimposed by the half transparent fitting panel. Different color of the fitting panel represents different stable charge area. As can be seen, the transition lines between different charge area overlap well with the transconductance charge sensing lines. We use a tunnel coupling of $t_c = 100\mu eV$ in this fit. This tells us the tunnel coupling at this anticrossing is around $100\mu eV$. However, the electron temperature is not absolute zero which gives broadening to the charge transfer

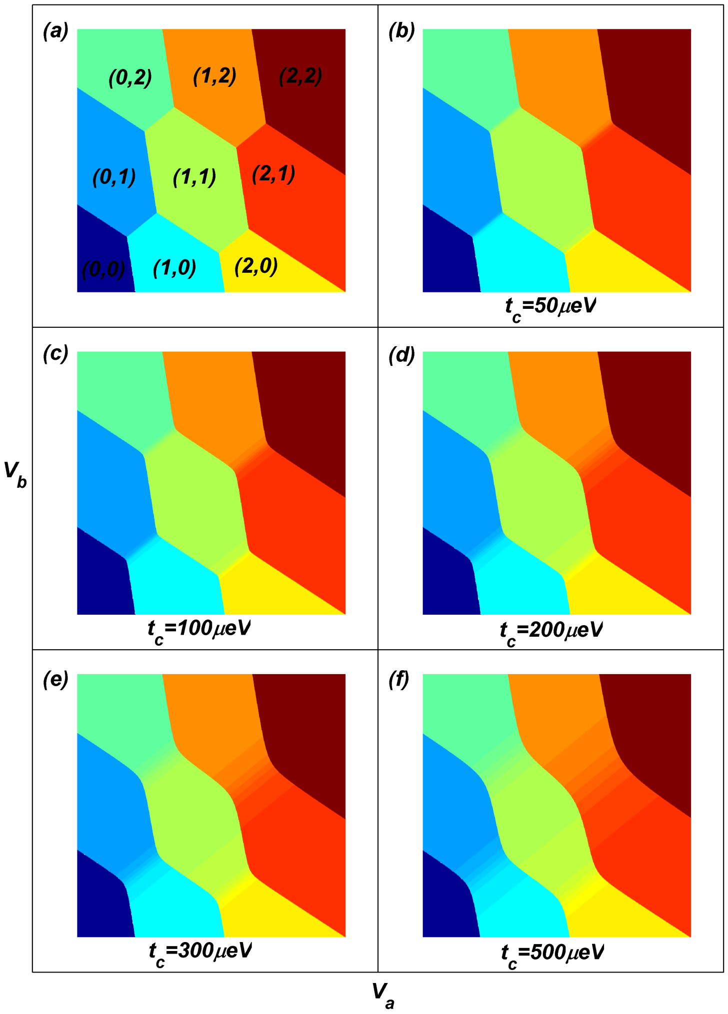

Figure 4.7: Calculated charge stability diagram based on Hubbard model for double quantum dot. Two voltage axis is in unit of mV. $U_1 = U_2 = 10meV, V_{12} = 3meV$. Charge numbers (N_1, N_2) are marked in (a). (a) $t_c = 0$; (b)-(f) t increases from $50\mu eV - 500\mu eV$. The tunnel coupling induced effect in only obvious when t_c is larger than $100\mu eV$.

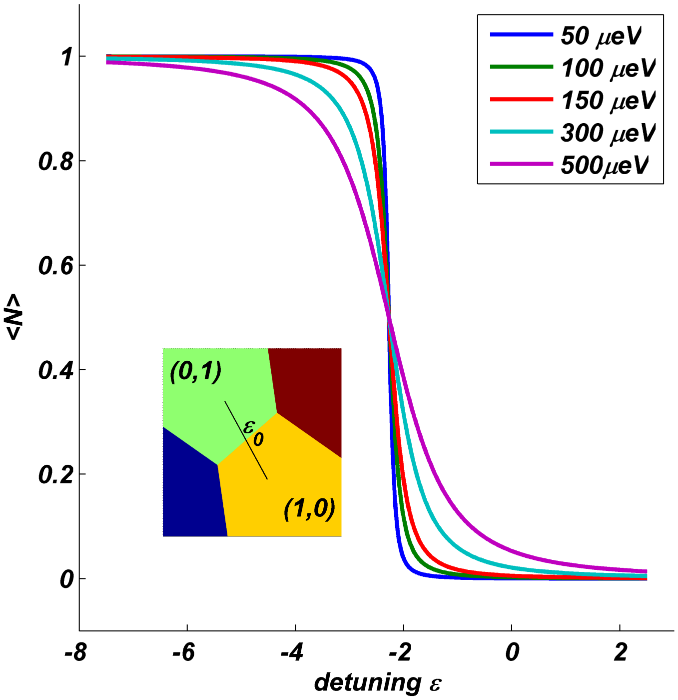

Figure 4.8: Probability of having excessive electron from (0,1) to (1,0) at different tunnel coupling. Inset: charge stability diagram at $t_c = 0$.

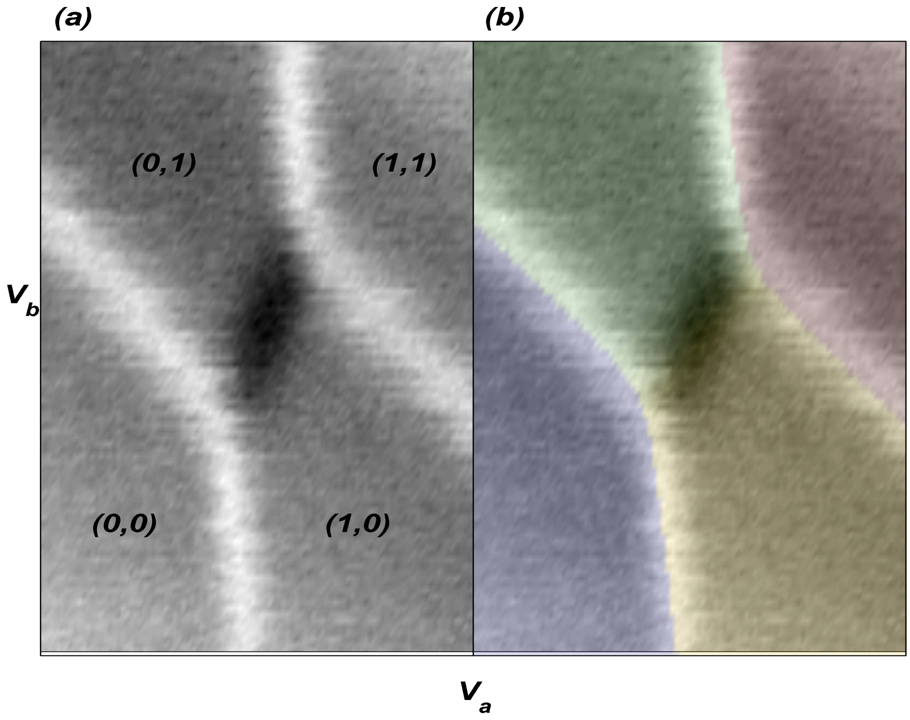

Figure 4.9: (a) Experimental stability diagram. (b) Experimental diagram superimposed with transparent fitting diagram calculated using Hubbard model with $t_c = 100\mu eV$. Charge number (N_1, N_2) is marked just for guildance.

regime. Thus we cannot give very precise tunnel coupling. For comparison, we also list the fitting with $50\mu eV$ in FIG.4.10. The left is the fitting from $100\mu eV$ while the right is using $50\mu eV$. It seems in the right one the fitting panel is less curved than the left one. This gives the tunnel coupling range of $50 \sim 100\mu eV$. The hubbard model gives us good estimation of the tunnel coupling range which is helpful. We also want to emphasize that the hopping term has the physics meaning of electron wave function overlap. In reality t is not a fix value and should change when the overal electrostatic potential changes due to external pluger gate voltage. However, at first level approximation, we assume it is a constant at the charge configuartion we studied. Thus this extraction is rough.

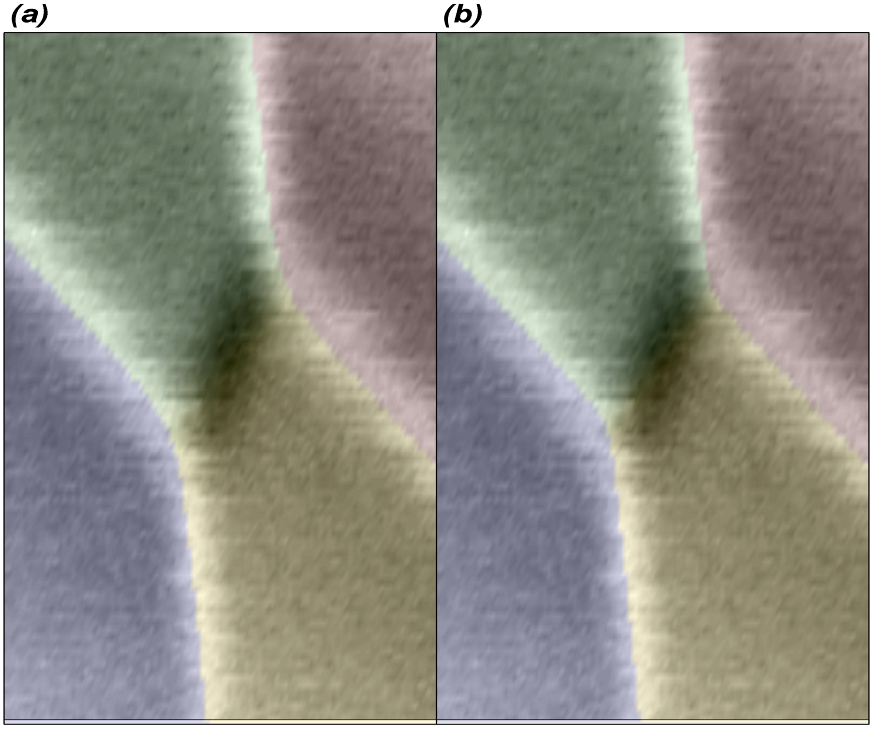

Figure 4.10: (a) Experimental diagram superimposed with fitting diagram calculated using Hubbard model with $t_c = 100\mu eV$;(b) fitted with $50\mu eV$

4.3 Hubbard model for triple quantum dot

In this section, we extend the hubbard model to triple quantum dot. The initial assumption are still kept. Now, we have three sites in the model and each site can host up to two electrons. The total charge configuration range we will study is from (0,0,0) to (2,2,2). The most important regime related with exchange only manipulation is (1,0,2), (1,1,1) and (2,0,1).

For triple hubbard model, the generalized hubbard model can still be written as follow:

$$H = \sum_{ij\sigma}(E_i\delta_{ij} + t_{ij})C^{+}_{i\sigma}C_{j\sigma} + \sum_{i} U_i n_{\uparrow i} n_{\downarrow i} + \sum_{i\neq j} V_{ij} n_i n_j n_l; \tag{4.12}$$

This Hamiltonian can still be blocked diagonized due to the total electron number and total spin. Ref. [KGH07] gives detail description for situations with different electron numbers. We calculate the total energy from the Hamiltonian and find out the maxium number of electrons the dot can host under certain pluger gate voltages. To increase visibity, we assign each charge cofiguration a number as QPC current.

We first want to verify our model to see if we can reproduce the capacitive model result when we set the hopping term zero. FIG. 4.11 (a) shows a two dimensional slide where we fix the middle dot pluger gate voltage. Different color magnifests different charge configuration. The detail parameter used to simulated this diagram can be found in the titile of FIG 4.11. We can see three sets of parallel transitions between different charging area which mean the loading of electron to dot 1, 2 and 3. When the tunnel coupling between neighboring dots are turned on, the anti crossing area become curved. To verify our simulation, we turn on t_{12}, t_{13}, t_{23} once at a time and in the simulation result only the corresponding anti cross shows charg state supperposition. For example in FIG. 4.11 (b), only t_{12} is on. Thus we only see interdot transition line broaden at (2,1,1) and (2,0,2). Similaly to double dot situation, the curvature and smooth change of QPC current reflects the magnitude of tunnel coupling, similar to that in double dot case.

Now we focus on the (1,1,1) regime. We try to see with the tunnel coupling included,

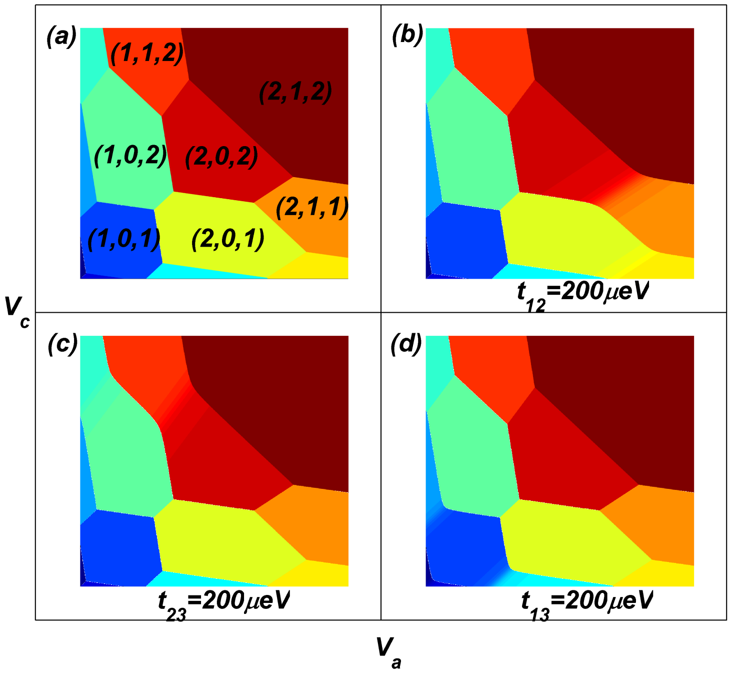

Figure 4.11: Calculated charge stability diagram based on Hubbard model for triple quantum dot. $U_1 = U_3 = 7meV, U_2 = 12meV, V_{12} = V_{23} = V_{13} = 2, V_b = 0V$. $(a)t_{12} = t_{13} = t_{23} = 0$. (b) $t_{12} = 200\mu eV$. (c) $t_{23} = 200\mu eV$. (d) $t_{13} = 200\mu eV$.

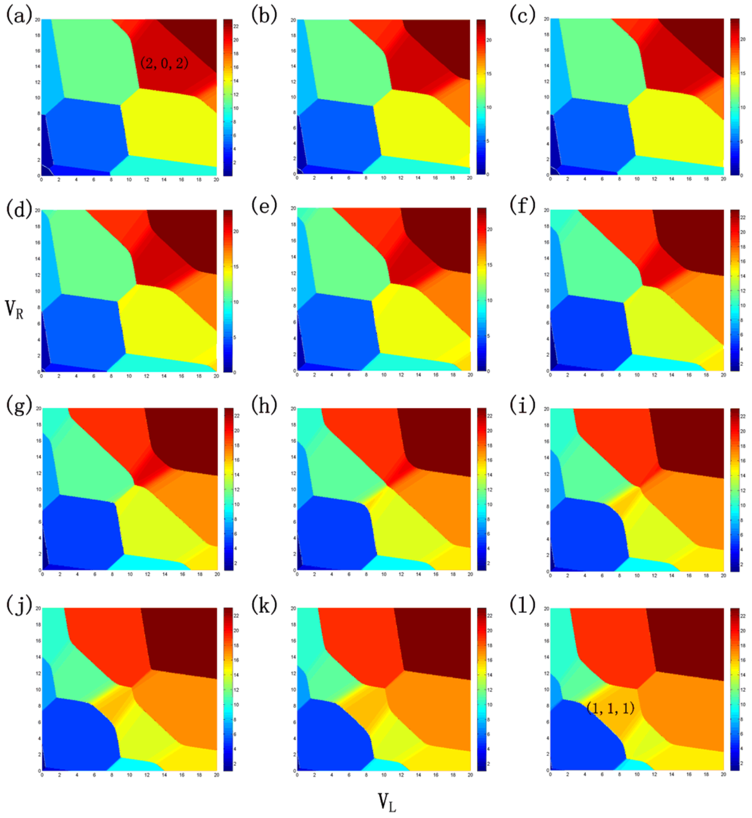

Figure 4.12: Evolution of triple dot stability diagram near charge configuration (1,0,2)-(1,1,1)-(2,0,1). Each graph is a stability diagram in voltage space of pluger gate on dot 1 and 3. (a)-(i) shows the evolution when the plunger gate voltage on dot 2 is gradually changed

how the stability diagram evolve when we change the middle gate voltage. FIG. 4.12 (a) is similar to FIG. 4.11 except tunnel coupling t_{12} and t_{23} is on. Same simulation parameters are used as in FIG. 4.11. From (a)-(i), V_b is gradually changed. And we see the (2,0,2) regime starts to shrink and when the (1,1,1) regime starts to come out. This sequence reproduces the experimental observation in Ref. [GGK10]. Due to the tunnel coupling, the qpc current is gradually changed which means the ground state of the system is not pure.

To summarize, we modified the constant interaction model shown in Ref. [WFE03] to include the cross capacitance. We studied how the cross capacitance would change the shape of the charge stability diagram. Following the hubbard model proposed in Ref. [YWS11], we revised the constant interaction model to accomodate the quantum fluctuation induced by interdot tunnel coupling. We used this model to fit the exeperimental diagram and extract the range of interdot tunnel coupling. Furthurmore, we follow the work in [KGH07] to develop the hubbard model for triple quantum dot and are able to reproduce the charge stability diagram. We also simulated the evolution of charge stability diagram in two dimensional voltage space by just changing the plunger gate voltage of the remaining dot. This is near the charge configuration (2,0,1)-(1,1,1)-(1,0,2). In Chapter 5, we will use the hubbard model to simulate the quadruple point tuning evolution.

Here, we only use the hubbard model to find the ground state under certain voltages settings. In the work of Ref. [KGH07], the author found that for a two electron filled case, the gap between the ground and first excited states, the singlet triplet splitting, is proportional to the single particle tunneling matrix element. For a four electron filled case, they predict a spin polarized ground state and a singlet triplet transition only by modifying the topology of the system. This gives us guildance of future experiment on this triple dot device.

More sophisticated model is covered in Ref.[KGH07, YWS11, SWY11]. They solve the Shrondiger equation and extract the chemical potential and tunnel coupling as a function of the applied depletion gate voltages. Our model is much simpler yet still able to reproduce most of the results from their calculations.

CHAPTER 5

Characterization of Si MOS based triple quantum dot device

In this chapter, we focus on the tuning of triple dot device HD5 in last few electron regime. We demonstrated the tunability of the device by achieving the quadruple points where all three dots are on resonance. The tuning evolution is shown to be consistent with a constant interaction model. Quantum cellular automana (QCA) is also identified near the quadruple point. We also include the hubbard model calculation to simulate the tuning evolution. The device SEM image and stability diagram can be seen Chapter 3.

5.1 Quadruple Points Tuning

One unique feature of TQD is the QP where four electron configurations have same energy so that one electron can tunnel serially through three dots. For DQD, similar resonance points are identified as triple points where charging lines (adding one electron into one dot from reservoir) for different fots meet each other. On a two dimensional stability diagram, the triple points is where two charging lines and one inter dot transfer line (electron tunnel between different dots whie not changing the total number of elelctrons in dots) meet. For TQD, the full stability digram extends into three dimensions, and charging lines evolves into planes. A quadruple point emerges where three charging planes are brough close to each other.

5.1.1 Quadruple points tuning

To follow the tridimensional nature, we follow the scheme in Ref. [GGK10]. FIG. 5.1 illustrates this strategy for achieving quadruplie point. We start with an arbitrary two dimensioanl scan of V_L and V_R as seen in FIG. 5.1 (a). We see charging lines from left, middle, and right dot, marked by green, magenta, and blue, respectively. Electron numbers are written in sequence of left, middle, and right. Two triple points associated with degeneracy between (2,1,3) and (2,2,2) and (2,1,3) and (1,2,3) charge states are marked by red and blue dots, respectively. Inter dot charge transfer lines are marked by black dashed lines for clarity. From FIG. 5.1 (b)-(e), V_{QR}, which controls the middle dot chemical potential , is steadlily increased and the two triple points are getting closer and closer and finally merge as one green point the quadruple point. At this point the four electron configurations (2,2,2), (2,1,3), (1,2,3), and (2,2,3) are energetically dengenerate. With V_{QR} increased more in FIG. 5.1 (f), this QP disappears beacuse these energy levels are mis matched again. In FIG. 5.1 (b), the black point where four lines cross is another QP. With increasing V_{QR}, this QP splits into another two triple points. Similar evolution has been observed beforein GaAs triple quantum dots. [GSS06]. The same evolution happened when we incrased the voltage on V_{QL} and keep V_{QR} constant.

5.1.2 Quantum cellular Automata (QCA) effect

Another interesting phenomenon near the quadruple points is the quantum cellular automata effect. [AOT99, TL01].The QCA process involves transferring one electron from a reservoir to one of the triple dots, which stimulates the TQD to reconfigure iteself automatically by pushing one electron from one dot to the third. In FIG.5.1(b), one can see two charge configurations: (1,2,2) and (2,1,3). Staring with (1,2,2) state one electron is added to the left dot. Instead of forming the (2,2,2) state, the system adjusts itself by pushing one electron in the middle dot into the right dot to reach the (2,1,3) state which has less energy. The pink separation lines which is intentiannly extended marking this transition has a differnt slope than the normal charging line (green dash) becaue crossing this line involves two charge transferring process.

In double dot, transport current can only happen at triple points if no DC bias is applied to source ohmic contact. Similarly, in triple quantum dot, current is expected to bee seen only at quadruple points. However, in some situation ,when cotunneling is strong, current can be seen at triple points in TQD system. Earlier, in another device, we observed this cotunneling. Interestingly, at places where we identified QCA effect through charge sensing signal, we find that the corresponding current distribution is stronger at "red" line position in FIG. 5.1 (b) than at triple points, shown in FIG. 5.2. This phenomenon has been previous reported in Ref. [SGG07]. QCA involes two charge transfer events. However it is different from normal cotunneling effects because the charge is not conserved. They refer it as QCA cotunnelig process. The stronger current at QCA lines suggests that the QCA cotunneling processes, with two particles simultaneously moving, resulting in a larger tunneling probability than regular second orde cotunneling processes, which can be explained in a one-particle picture. The origin of this phenomenon lies in the electrostatic interaction between two electrons tunneling simultaneously.

5.2 Constant interaction model simulation

To get furthur understanding of the QP evolution, we used the constant interaction model we developed in chapter 4. Here we showed the equivalent circuit model for reference in FIG. 5.3 (a). The capacitances are assigned as $C_{dot,dot}$ and $C_{gate,dot}$. Cross capacitance such as $C_{L,B}$ and $C_{R,A}$, are also considered (not shown in the diagram due to space limit). The stability diagram is calulated by finding the charge configuration (N_A, N_B, N_C) with minimum total energy E_{TQD} under certain voltage setting. The detail calculation has been discussed in Chapter 4. The model does not include quantum effects, suc as differnt orbital stats, tunnel coupling, nor exchange interactions. However, it gives a good qualitaie description of the system in linear regime. By carefully studying the experimental stability digram, we extract the ralactive value of capacitances. The distance between parllel charging lines gives the estimation of electron charging energy in differnt dot. The length of the charging transfer lines between two triple points represents the magnitude of the electrostatic coupling energies between two dots. The slope of the charging lines gives information about the cross capacitance. Combining all the information, we estimate dominant capacitances as follow: $C_{M,B} = 0.8C_{L,A} = 0.9_{R,C}$ and $C_{A,C} = 0.3C_{A,B} = 0.6C_{B,C}$. In this device, we found the gate R also affects chemical potential in the midle dot, resulting considerable cross capacitance $C_{R,B} = 0.6C_{R,C}$.

FIG. 5.3 (c) sows the numerical result of the constant interaction model. Here, the y and x axis correspind to the plunger gate voltages V_L and V_R. All other gate voltages are kept constant and constant energy offset is neglected in the simulation. Black lines marke borders of the stabile charge configurations (N_A, N_B, N_C). The simulation result reproduce most of the featurs of the experimental diagram in FIG. 5.3 (b). FIG. 5.3 (c)-(g) record stability diagram under same $V_L and V_R$ but with V_M increased in each frame as in the experimental data in FIG. 5.1. In FIG. FIG. 5.3(c), two triple points are marked as red and blue. With V_M increased in each frame, the two triple points get closer and closer and finally merge to one point in FIG. 5.3(f). This process shows the same evolution as in FIG. 5.1. In FIG. 5.3(f), pink like which overlaps the separation line between (2,1,3) and (1,2,2) has differrent slope from the left dot charging line nearby. This is thesame phenomenon, the QCA effect, as we described in FIG. 5.1. In the frame of constant interaction model, the coupling strenght between dots contributes to the total energy of the triple dot. The coupling strength depends on the coupling capacitance between dots, such as $C_{A,B}$ and $C_{B,C}$. When $C_{A,B} \neq C_{B,C}$, adding one more electron into the system might cause the rearrangement of electron configuration due to the asymmetry in inter-dot coupling energy. We extended our simulation to three dimensions in voltage space and found that close to the quadruple point, the QCA line extends into a plane which is not parallel to any other plane.

It should be noted that there are six quadruple points predicted for TQD in total. [GGK10]. In the regime we study above in this device, we only observe two QPs which correspond to the QP1 ad QP6 in Ref. [GGK10]. Part of the reason is that in this device, there is considerable cross capacitance between plunger gate V_R and middle dot while in Ref. [GGK10] the cross capacitance is much smaller. When we vary V_R, both the right dot and middle dot potential change considerably. This limits our ability to tune the three dots independently. Thus we did not observe six QPs in the voltage range we studied.

To futhur understand the system, we simulate the evolution using triple dot Hubbard model with tunneling coupling turned on. We extracted the simulation parameters from the experimental diagram FIG.5.1. The simulation result is displayed in FIG.5.4. Since the hubbard model only allowed two electron maximum in one dot, thus we subtract one electron from the right dot and only consider the ground state situation.

The result reproduce the constant interaction model pretty well. Additionally, it demonstrates that at when tunnel coupling is on, at quadruple points, the triple dot electron wave function is actually a superposition of three singlet dot level. [?] discussed the transport at quadruple points in a GaAs triple quantum dot. The bipolar spin blockade phenomena is a direct consequence of this superposition state.

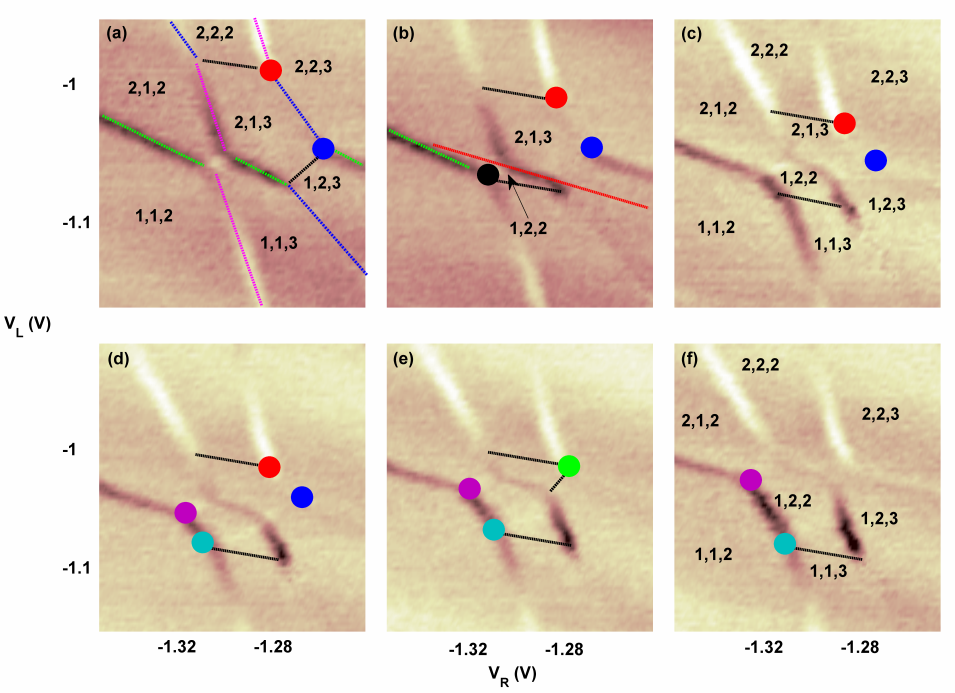

Figure 5.1: Evolution of achieving quadruple points. From (a)-(f), V_{QR} is increased by 3mV per frame. The transport channel is grouned to minimize noise. (a) Two triple points, where the middle and right dot (red) and left and right dot (blue) are on resonance. (b)A regime emerges which signifies the QCA effect. Crossing green line means electron number change by one in left dot. Crossing pink line (intentionally extended for compaison) involves addition of an electron onto left dot and tunneling of one electron from middle dot to the right dot. The red and green lines have different slope. (c), (d) Two triple points are brought together by adjusting V_{QR}. (e) Two charge transfer lines meet up at one point (green), achieving the quadruple point. (f) By adjusting V_{QR}, the three dots are off resonance again with triple points move apart.

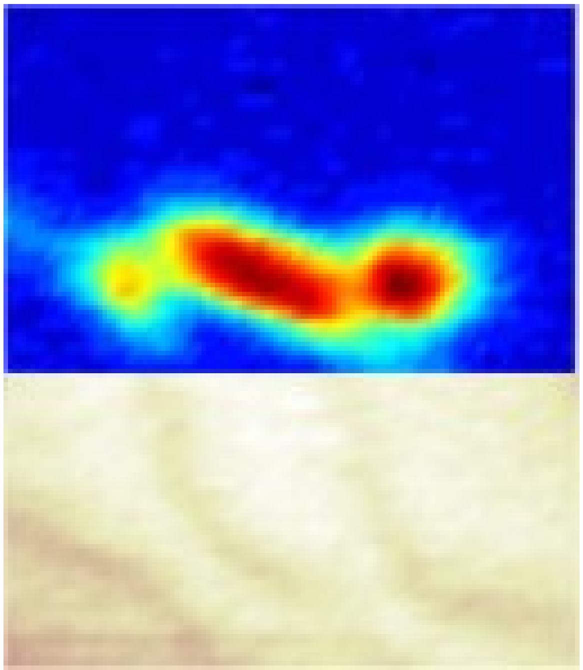

Figure 5.2: (a) Stability diagram showing regime where QCA effect takes places (b) Corrsponding transport data. Current at charge transfer line is larger than at triple points due to the higher order tunnelling process

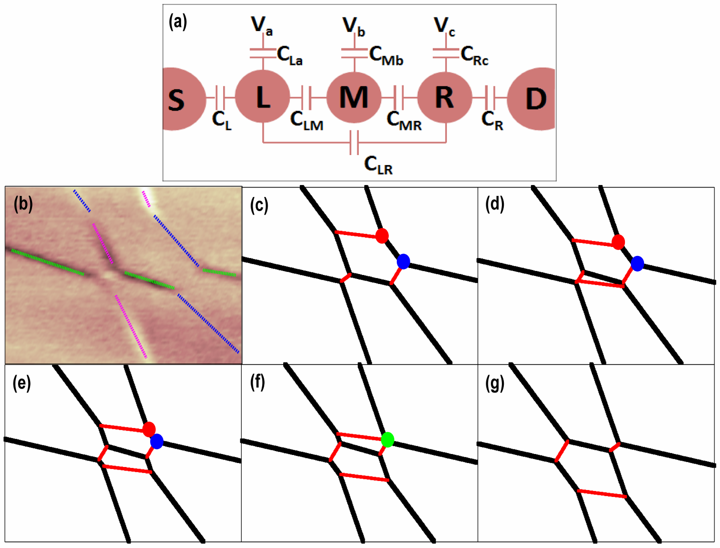

Figure 5.3: (a) Equivalent circuit model for a triple quantum dot. (b) Experimental stability diagram, green, blue, and magneta lines represent the charge transition of left, middle, and right dot, respectively. (c)-(g) Calculated stability diagram with increasing middle dot plunger gate potential in each frame. The evolution shows the same trend as in the experimental result in FIG. 5.1. (f) Pink line (intentionally extended) marks the places involving charge transition and reconfiguration. Its slope is different from the left dot charging line nearby.

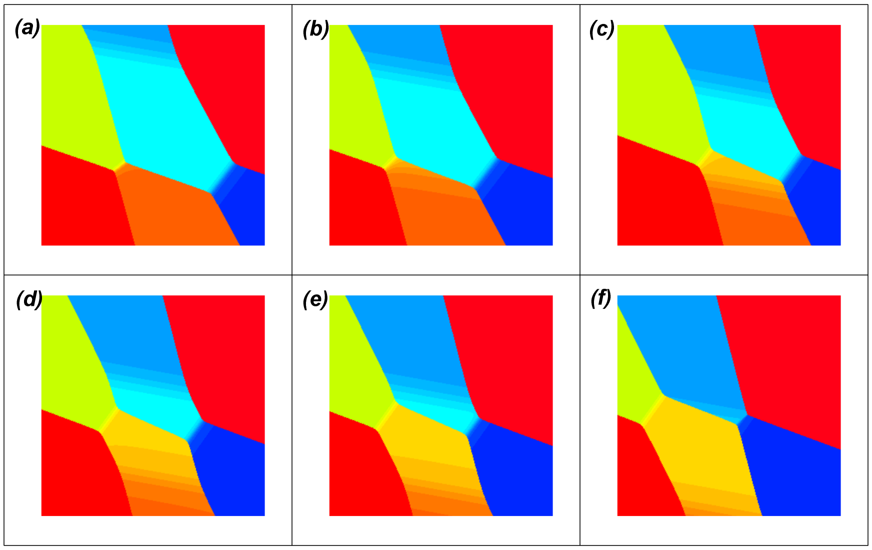

Figure 5.4: Hubbard model simulation of quadruple points tuning evolution. $U_1 = 7meV, U_2 = 12meV, U_3 = 7meV$, $V_{12} = 2meV, V_{23} = 4meV, V_{13} = 0.8meV$, $t_{12} = 0.04meV, t_{23} = 0.1meV, t_{13} = 0.02meV$.

CHAPTER 6

Theoretical implementation of single qubit manipulaton based on triple quantum dot

6.1 Single qubit realization in exchange coupled triple quantum dot

In Chapter 4, we have shown that the Hubbard model gives very good description of the triple quantum dot system including tunneling effect. The exchange only qubit is proposed in the configuration of three electrons. In this chapter, we will first review the physics of the triple dot system with three electrons using Heisenberg exchange hamiltonian. We then provide theorectical simulation of single qubit manipulation.

6.1.1 Heisenberg exchange model for triple quantum dot

Here, we first consider the case for linearly arranged triple quantum dot filled with three electrons as seen in FIG. 6.1 (a). Only tunnel coupling between neighboring dot, t_{12}, t_{23} is considered. $t_{13} = 0$. FIG. 6.1(b) shows the crossponding charge stability diagram. In the central area, electrons are singlely occupied. At the boundry between (1,1,1) and (2,0,1)/(1,0,2), the tunnel coupling cause the charge states hybridization.

The halmitonian including a magnetic field can be approximated as following:

$$H = J_{12}(S_1 \cdot S_2 - \frac{1}{4}) + J_{23}(S_2 \cdot S_3 - \frac{1}{4}) + E_z(S_1^z + S_2^z + S_3^z) \tag{6.1}$$

This halmitonian is only first order approximation. More accurate result can be refered to Ref.[SS05] which considers the higher order spin spin interaction. The halmitonian is a

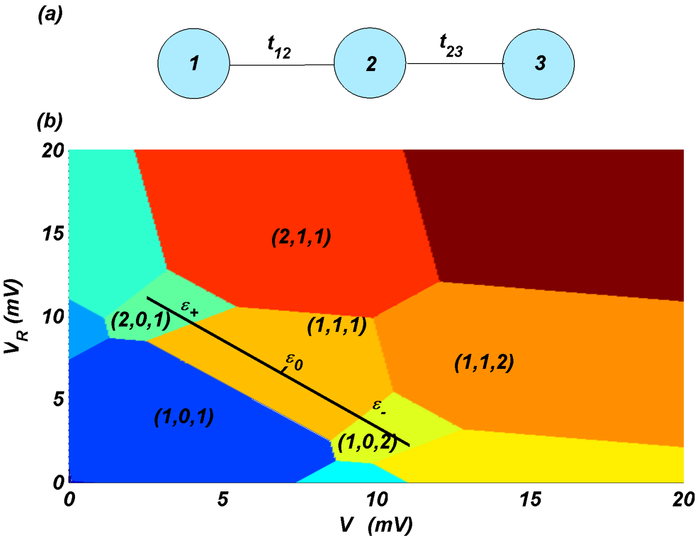

Figure 6.1: (a) Linear triple quantum dot. $t_{12}(t_{23})$ are the tunnel coupling between neighboring dots. (b) Charge stability diagram calculated using the Hubbard model. Electron numbers in each dot are marked. The detuning line is drawn as black across charge regime (2,0,1)-(1,1,1)-(1,0,2), which is parallel to the charge transfer line between (1,0,1) and (1,1,1). ϵ_0 is defined as the detuning zero point. $\epsilon_+(\epsilon_-)$ is the interdot transition point between the (2,0,1)/(1,0,2) and the (1,1,1) regime

8×8 matrix. It is easy to see that $[H, S_z] = 0$. The total spin in z direction S_z is a good quantum number. Thus the Halmitonian can be blocked diagonized in four groups with $S_z = \pm\frac{1}{2}, \pm\frac{3}{2}$. Thus $H = |\uparrow\uparrow\uparrow> \otimes |\downarrow\uparrow\uparrow>, |\uparrow\downarrow\uparrow>, |\uparrow\uparrow\downarrow> \otimes |\uparrow\downarrow\downarrow>, |\downarrow\uparrow\downarrow>, |\downarrow\downarrow\uparrow> \otimes |\downarrow\downarrow\downarrow>$. $|Q_{+3/2}>= |\uparrow\uparrow\uparrow>$ and $|Q_{-3/2}>= |\downarrow\downarrow\downarrow>$ are eigen states of H and the they have total spin $S = \frac{3}{2}$ with $S_z = \pm\frac{3}{2}$. $E_{Q_{\frac{3}{2}}} = -E_z S_z$. For group $|\downarrow\uparrow\uparrow>, |\uparrow\downarrow\uparrow>, |\uparrow\uparrow\downarrow>$, H can be written as follow:

$$H = \frac{1}{2}\begin{pmatrix} -g\mu_B B - J_{12} & J_{12} & 0 \\ J_{12} & -g\mu_B - J_{12} - J_{23} & J_{23} \\ 0 & J_{23} & -g\mu_B B - J_{23} \end{pmatrix} \tag{6.2}$$

By diagonizing this matrix we can get one quadruplet state $Q_{1/2}$ with $S_z = 1/2$ and two doublet states $|\Delta'_{1/2}>$ and $|\Delta_{1/2}>$.

$$\begin{gathered}
E_{Q_{\frac{1}{2}}} = -E_z S_z. \\
|Q_{1/2}>= \frac{1}{\sqrt{3}}(|\downarrow\uparrow\uparrow> + |\uparrow\downarrow\uparrow> + |\uparrow\uparrow\downarrow>) \\
E_{\Delta'_{1/2}} = -\frac{1}{2}(J_{12} + J_{23} + \Omega) - E_z S_z. \\
|\Delta'_{1/2}>= -\frac{1}{\sqrt{4\Omega^2 + 2\Omega(2J_{12} - J_{23})}}((-J_{12} + J_{23} - \Omega)|\downarrow\uparrow\uparrow> -(J_{12} + \Omega)|\uparrow\downarrow\uparrow> + J_{23}|\uparrow\uparrow\downarrow>) \\
E_{\Delta_{1/2}} = -\frac{1}{2}(J_{12} + J_{23} - \Omega) - E_z S_z. \\
|\Delta_{1/2}>= -\frac{1}{\sqrt{4\Omega^2 - 2\Omega(2J_{12} - J_{23})}}((-J_{12} + J_{23} + \Omega)|\downarrow\uparrow\uparrow> -(J_{12} - \Omega)|\uparrow\downarrow\uparrow> + J_{23}|\uparrow\uparrow\downarrow>) \\
\Omega = \sqrt{J_{12}^2 + J_{23}^2 - J_{12}J_{23}};
\end{gathered} \tag{6.3}$$

Similarly, for group $|\uparrow\downarrow\downarrow>, |\downarrow\uparrow\downarrow>, |\downarrow\downarrow\uparrow>$, we get another quadruplet state $Q_{-1/2}$ with $S_z = -1/2$ and two doublet states $|\Delta'_{-1/2}>$ and $|\Delta_{-1/2}>$.

$$H = \frac{1}{2}\begin{pmatrix} g\mu_B B - J_{12} & J_{12} & 0 \\ J_{12} & g\mu_B - J_{12} - J_{23} & J_{23} \\ 0 & J_{23} & g\mu_B B - J_{23} \end{pmatrix} \tag{6.4}$$

and eigenstates are as following:

$$\begin{aligned}
&E_{Q_{-\frac{1}{2}}} = -E_z S_z. \\
&|Q_{-1/2}> = \frac{1}{\sqrt{3}}(|\uparrow\downarrow\downarrow> + |\downarrow\uparrow\downarrow> + |\downarrow\downarrow\uparrow>) \\
&E_{\Delta'_{-1/2}} = -\frac{1}{2}(J_{12} + J_{23} + \Omega) - E_z S_z. \\
&|\Delta'_{-1/2}> = \frac{1}{\sqrt{4\Omega^2 + 2\Omega(2J_{12} - J_{23})}}((J_{12} - J_{23} + \Omega)|\uparrow\downarrow\downarrow> - (J_{12} + \Omega)|\downarrow\uparrow\downarrow> + J_{23}|\downarrow\downarrow\uparrow>) \\
&E_{\Delta_{-1/2}} = -\frac{1}{2}(J_{12} + J_{23} - \Omega) - E_z S_z. \\
&|\Delta_{-1/2}> = \frac{1}{\sqrt{4\Omega^2 - 2\Omega(2J_{12} - J_{23})}}((J_{12} - J_{23} - \Omega)|\uparrow\downarrow\downarrow> - (J_{12} - \Omega)|\downarrow\uparrow\downarrow> + J_{23}|\downarrow\downarrow\uparrow>) \\
&\Omega = \sqrt{J_{12}^2 + J_{23}^2 - J_{12}J_{23}};
\end{aligned} \tag{6.5}$$

When B=0, four quadruplet states are degenerate. The doublet states can be summarized in two groups $|\Delta'_{\pm 1/2}>$ and $|\Delta_{\pm 1/2}>$. Both are doublely degenrate. We define the detuning line as drawn in FIG. 6.1 (b). To fully characterize this system, we assume the (1,1,1) charge regime is sufficient large so that near charge transition (1,1,1) and (1,0,2), we can consider the right dot as two double dot very weakly coupled with the left dot. Thus we can approximate $J_{23}(\epsilon) = (\epsilon - \epsilon_+)/2 + \sqrt{(\epsilon - \epsilon_+)^2/4 + t_{23}^2}$. Similarly, $J_{12}(\epsilon) = (\epsilon_- - \epsilon)/2 + \sqrt{(\epsilon_- - \epsilon)^2/4 + t_{12}^2}$. $\epsilon_\pm$ are marked in FIG. 6.1. Thus we can calculate the energy spectrum along the detuning. One case for symmetric left and right interdot tunnel coupling is presented in FIG. 6.2. With magnetic field, the quadruplet states split into four. Near zero detuning, the dot is configured in (1,1,1). The states crossponding to $S_z = -\frac{1}{2}$ are $|Q_{-1/2}$,$|\Delta'_{-1/2}>$ and $|\Delta_{-1/2}>$. The energy difference between $|Q_{-1/2}$ and $|\Delta_{-1/2}>$ is actually half of that between two doublet states which is$J_{12}(\epsilon = 0)$. Increasing(decreasing) ϵ lowers the energy of doublet states $|\Delta'_{\pm 1/2}>$ by $J_{23}(J_{12})$. For $\epsilon > \epsilon_+$ and $\epsilon < \epsilon_-$, the doublet state correspond to the $|S_r>$ $(|S_l>)$.

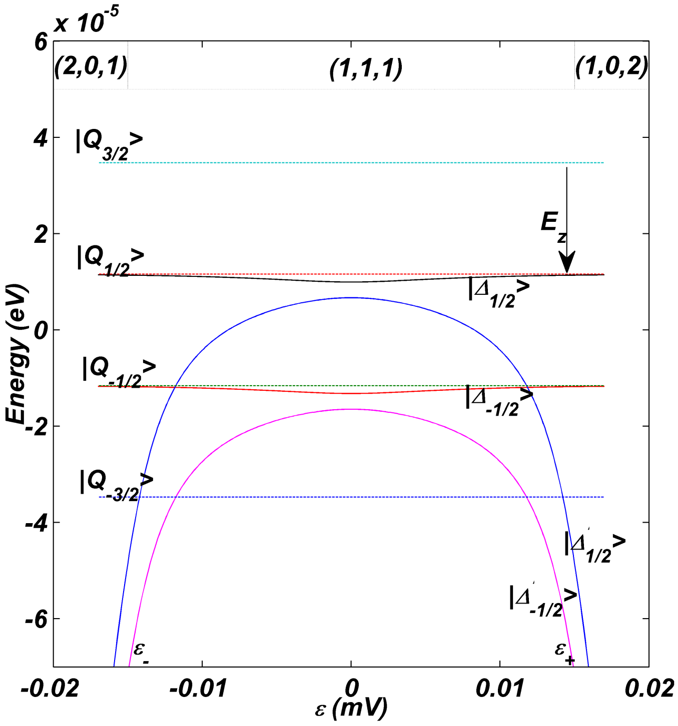

Figure 6.2: Three electron energy levels as a function of detuning ϵ drawn in FIG. 6.1 for a linearly arranged triple quantum dot. The plot shows the case for left and right inter-dot tunnel coupling. Near zero detuning, the dot is configured in (1,1,1) with negligible exchange; increasing(decreasing) ϵ lowers the energy ofdoublet states $|\Delta'_{\pm 1/2} >$ by $J_{23}(J_{12})$. For $\epsilon > \epsilon_+$ and $\epsilon < \epsilon_-$, the doublet state correspond to the $|S_r >$ $(|S_l >)$.

6.1.2 Divencenzo manipulation

From energy levels in upper case, we find that the subspace $|\Delta'_{1/2}>$ or $|\Delta_{1/2}>$ is suitable for realizing a qubit. They are separate from other states due to different S, S_z. The energy difference between the two states can be tuned by depletion gate voltages. Divincezo [DBK00] proposed creating a single qubit using this two level system. Here, we present the proposal in detail with coherent manipulation calculations. This two level system is also in the decoherence free subspace. Along the detuning line, when $J_{12}(\epsilon) = J_{23}(\epsilon) = J$, $|\Delta'_{1/2}>$ or $|\Delta_{1/2}>$ are simplified as :

$$\begin{aligned} |\Delta'_{1/2}> &= \frac{1}{\sqrt{6}}(|\downarrow\uparrow\uparrow> -2|\uparrow\downarrow\uparrow> +|\uparrow\uparrow\downarrow>) \\ |\Delta_{1/2}> &= \frac{1}{\sqrt{2}}(-|\downarrow\uparrow\uparrow> +|\uparrow\uparrow\downarrow>) \end{aligned} \tag{6.6}$$

We can define these two states as qubit state $|0>$ and $|1>$. We can plot them as the north pole and south pole on the bloch sphere as seen in FIG. 6.3. In the limit of $J_{12}/J_{23} \to 0$, corresponding to the charge regime (1,1,1)-(1,0,2). The doublet states $|\Delta'_{1/2}>$ or $|\Delta_{1/2}>$ becomes:

$$\begin{aligned} |\Delta'_{1/2}> &= \frac{1}{\sqrt{2}}(|\uparrow\uparrow\downarrow> -|\uparrow\downarrow\uparrow>) \\ |\Delta_{1/2}> &= \frac{1}{\sqrt{6}}(|\uparrow\downarrow\uparrow> +|\uparrow\uparrow\downarrow> -2|\downarrow\uparrow\uparrow>) \end{aligned} \tag{6.7}$$

$|\Delta'_{1/2}>$ is singlet like and also written as $|S_r>$.$|\Delta_{1/2}>$ can be written as a mixed triplet state of right two electrons times $|\uparrow>$. Thus we write it as $|T_r>$. Analogously, in the limit of $J_{23}/J_{12} \to 0$,

$$\begin{aligned} |S_l> &= \frac{1}{\sqrt{2}}(|\uparrow\downarrow\uparrow> -|\downarrow\uparrow\uparrow>) \\ |T_l> &= \frac{1}{\sqrt{6}}(|\downarrow\uparrow\uparrow> +|\uparrow\downarrow\uparrow> -2|\uparrow\uparrow\downarrow>) \end{aligned} \tag{6.8}$$

we can plot $|S_r>$ and $|S_l>$ in the same bloch sphere in FIG. 6.3. They are $\pi/3$ away from the z axis. The one qubit manipulation can be realized in the following sequence, seen in FIG. reffig:exchangequbit . The initial state can be prepared by set the system in (1,0,2) to form $|S_r>$ and then let the state evolve adibatically along the ground state.till reaching $|0>$. To realize single qubit flip, we can first pulse the prepared $|0>$ state to place near charge transition (2,0,1)-(1,1,1), where J_{12} is large, J_{23} is negligible. $|0>$ will rotate around axis J_{12} (also denoted as J_l), seen in FIG. 6.4 (a). When the state rotate to the x,y plane after time τ_1, we pulse it back to $\epsilon = 0$, where $J_{12} = J_{23}$. Now the rotation axis is along the z axis. we let the state evolve in x,y plane for time τ_2, FIG. 6.4 (b) and then pulse back to (2,0,1)-(1,1,1), the state will evolve to $|1>$ in the south pole in FIG. 6.4 (c). Now we have successfully realize single qubit flip in four steps including the initialization. τ_1, τ_2 and τ_3 can be accurately calculated once $J_{12}(\epsilon)$ and $J_{23}(\epsilon)$ is known. J_{12} and J_{23} can be extracted using spin funnel experiments and has been demonstrated in GaAs triple quantum dot [GGK12]. The single qubit flip in bloch sphere requires σ_x in Halmitonian. In singlet triplet qubit proposed in double quantum dot, the exchange interaction between singlet and triplet can only provide σ_z. The current coherent demonstration relies on the randome fluctuating nuclear field surrounding the double dot which provide σ_x. This σ_x is small and uncontrollable. In the exchange-only qubit, the two exchange interaction J_{12} and J_{23} are 120° apart, thus they are sufficient to provide rotation to any state on the bloch sphere by carefully designing the pulse sequence using classical Euler angle construction. Furthurmore, the exchange magnitude is a function of tunnel coupling which is tunable. This will provide much faster rotation in less than nano second. The time scale is much shorter than the qubit dephasing time from hyperfine interaction.

Coherent manipulation of electron spin using exchange interaction can be demonstrated in the following way. We prepare state $|S_l>$ near ϵ_- and then pulse the system to more positive detuning ϵ_s in (1,1,1) area. After time τ, we pulse it back to ϵ_-. The probability of retuning to $|S_r>$ is $P =< S_l|e^{-iH_j(\epsilon_s)\tau_s/\hbar}|S_l>$. The rotation halmitonian at ϵ_s can be written as:

$$H(\epsilon) = J_l(\epsilon)\sigma_l + J_r(\epsilon)\sigma_r; \sigma_l = (\sqrt{3}\sigma_x - \sigma_z)/4, \sigma_r = (-\sqrt{3}\sigma_x - \sigma_z)/4 \tag{6.9}$$

$J_l(\epsilon)$ and $J_r(\epsilon)$ in total determine the rotation axis. Thus we shall see P oscillating as a function of detuning ϵ_s and pulse duration τ_s. FIG. 6.5 shows the simulation result. Parameters used in this simulation can be found in figure caption.

The propability P can be calculated analytically. In bloch sphere representation.$|S_l>$ can be written as $S_0 = (-\sqrt{3}/2, 1/2)$. At any ϵ_s, we can decompose $J_{12}(\epsilon_s)$ and $J_{23}(\epsilon_s)$ in z and x direction. We name $J = (J_{12} + J_{23})/2$ and $j = \sqrt{3}(J_{23} - J_{12})/2$. The rotating angle is $\alpha = \sqrt{J^2 + j^2}\tau_s/\hbar$. The rotation matrix in bloch sphere representation can be written :

$$R = \begin{pmatrix} cos(\alpha/2) - icos(\theta)sin(\alpha/2) & -isin(\alpha/2)sin(\theta)e^{-i\phi} \\ -isin(\alpha/2)sin(\theta)e^{i\phi} & cos(\alpha/2) + icos(\theta)sin(\alpha/2) \end{pmatrix} \tag{6.10}$$

θ and ϕ are the direction of the rotation axis at ϵ_s. The resulting state $S' = R \times S_0$. P is easily calculated. At negative detuning, the rotation axis is always pointing the negative portion of north hemisphere resulting P slightly oscillating near 1. At zero detuning , the rotation axis is along z axis. And J_{12} and J_{23} are both small thus the oscillation period is much longer than other place. The bloch sphere diagrams at different situation are shown in FIG. 6.6. Same phenomena will be seen if we start at $|S_r>$. The measurement of probability is based on the spin blockade in (2, 0, 1) regime. Where the singlet like $|\Delta'_{1/2}>$ (1,1,1) states will tunnel back to (2, 0, 1) while the triplet like $|\Delta_{1/2}>$ will remain unchanged. The difference in charge configuration is detected by a nearby charge sensing channel similar to double quantum dot singlet triplet qubit. In GaAs linear triple quantum dot, Medford [MBT13a] has successfully demonstrated this manipulation. There is no major difference between quantum dot in GaAs and Si-MOSFET except g factor. while g factor will only affect energy difference between states with different S_z, it is very promising we would see similar oscillation in our system.

6.1.3 Asymmetrically coupled case

In the discussion above, we consider the dea case where $t_{12} = t_{23}$. In reality, we settle in asymmetric case for most of the time. FIG.6.7 shows the oscillations for the same pulse sequence in FIG. 6.5 with different t_{12} and t_{23}. We see that the main feature of pattern does not change. The slow oscillation seen at $\epsilon = 0$ in FIG.6.7 now shifts to other place where $J_{12}(\epsilon) = J_{23}(\epsilon)$. The only problem will be that if the aymmetric is large thus our initial assumption of having $|S_l>$ and $|S_r>$ lying 120○ will not be valid. Because at $\epsilon_+(\epsilon_-)$, the wave function cannot be written as a product of the left(right) two electrons state times the right(left) electron. The calculation will be adjusted. If the angle between the two axis is less than 90°, we can no longer realize the single qubit flip.

6.2 Physics of triple quantum dot in general case

In more generalized situation, t_{13} is not zero. If t_{13} is present. The Heisenberg Halmitonian is written as:

$$H = J_{12}(S_1 \cdot S_2 - \frac{1}{4}) + J_{23}(S_2 \cdot S_3 - \frac{1}{4}) + J_{13}(S_1 \cdot S_3 - \frac{1}{4}) + E_z(S_1^z + S_2^z + S_3^z) \tag{6.11}$$

This halmitonian can be diagonized in similar fashion as we did before. If we define $\Omega = \sqrt{J_{12}^2 + J_{23}^2 + J_{13}^2 - J_{12}J_{13} - J_{12}J_{23} - J_{13}J_{23}}$. We can get the Doublets eigen states are as following.

$$\begin{aligned}
&E_{\Delta'_{S_z}} = -\frac{1}{2}(J_{12} + J_{23} + J_{13} + \Omega) - E_z S_z.\\
&|\Delta'_{1/2}> = \frac{1}{\sqrt{4\Omega^2 + 2\Omega(2J_{23} - J_{12} - J_{13})}} \times\\
&((J_{23} - J_{12} + \Omega)|\uparrow\uparrow\downarrow> - (J_{13} - J_{23} - \Omega)|\uparrow\downarrow\uparrow> + (J_{12} - J_{13})|\downarrow\uparrow\uparrow>)\\
&E_{\Delta_{S_z}} = -\frac{1}{2}(J_{12} + J_{23} + J_{13} - \Omega) - E_z S_z.\\
&|\Delta_{1/2}> = \frac{1}{\sqrt{4\Omega^2 - 2\Omega(2J_{23} - J_{12} - J_{13})}} \times\\
&((J_{23} - J_{12} - \Omega)|\uparrow\uparrow\downarrow> - (J_{13} - J_{23} + \Omega)|\uparrow\downarrow\uparrow> + (J_{12} - J_{13})|\downarrow\uparrow\uparrow>)
\end{aligned} \tag{6.12}$$

The energy differece between As expected, the new state $|\Delta'_{1/2}>$ and $|\Delta_{1/2}>$ still belongs to the same subgroup of $|S_l>$ and$|T_l$. It is easy to verify that $<\Delta'_{1/2}|\Delta_{1/2}> = 0$. At $J_{12}(\epsilon_0) = J_{13}(\epsilon_0) = J$ and $J > J_{13}(\epsilon_0)$, we can still get the state:

$$\begin{aligned}
|0> = |\Delta'_{1/2}> &= \frac{1}{\sqrt{6}}(|\downarrow\uparrow\uparrow> - 2|\uparrow\downarrow\uparrow> + |\uparrow\uparrow\downarrow>)\\
|1> = |\Delta_{1/2}> &= \frac{1}{\sqrt{2}}(-|\downarrow\uparrow\uparrow> + |\uparrow\uparrow\downarrow>)
\end{aligned} \tag{6.13}$$

If we expand $\Delta_{1/2}>$ and $|\Delta'_{1/2}>$ in the representation of $|S_l>, |T_l>$. And the direction of the new state can be written as following:

$$\begin{aligned} r_{\Delta'_{1/2}}^{\rightarrow} &= (-\frac{\sqrt{3}}{2}\frac{J_{12}-J_{13}}{\Omega}, 0, -\frac{(J_{12}+J_{13}-2J_{23})}{2\Omega}) \\ r_{\Delta_{1/2}}^{\rightarrow} &= (\frac{\sqrt{3}}{2}\frac{J_{12}-J_{13}}{\Omega}, 0, \frac{(J_{12}+J_{13}-2J_{23})}{2\Omega}) \end{aligned} \tag{6.14}$$

We can get rotating axis as:

$$H_\epsilon(J_{12}, J_{23}, J_{13}) = -\frac{\sqrt{3}}{4}(J_{12}-J_{13})\sigma_x + \frac{J_{12}+J_{13}-2J_{23}}{4}\sigma_z \tag{6.15}$$

In the limit of ϵ_+ and ϵ_-, we can found that $|\Delta'_{1/2}>$ off from $|S_l>$ and $|S_r>$ by small amount depending on the ration of $J_{13}(\epsilon_-)/J_{23}(\epsilon_-)$ and $J_{13}(\epsilon_+)/J_{12}(\epsilon_+)$. The new angle between two rotating axis is less than 120°. FIG. 6.8 gives an example. However, as long as the angle between the two rotating axis is larger than pi/2, the exchange only qubit proposal is still be valid.

6.2.1 Hubbard model discription of three electrons

We can also get similar informaton from Hubbard model we discussed in last chapter. Similary, for singlely occupied states. There are in total 8 electron spin configuration. We consider the subgroup with $S_z = 1/2$ which is$|\downarrow\uparrow\uparrow>, |\uparrow\downarrow\uparrow>, |\uparrow\uparrow\downarrow>$. Ref.[KGH07] gives full Hubbard Halmitonian for this case $|\downarrow\uparrow\uparrow>$, due to tunnel coupling and spin conservation during tunneling, (1,1,1) is coupled with (0,2,1) and (0, 1,2) charge state and we can construct the Halmitonian matrix. In total, the matrix is 9×9. Along the detuning line ploted in FIG. 6.1 (b), we can get the energy spectrum and the eigenstates. FIG.6.9 (b) presents the results with $t_{12} = t_{23} = 20\mu eV$ and varying t_{13}. For the case of $t_{13} = 50\mu eV$, we get the ground state at detuning zero from simulation as $|g>= 0.7118|\downarrow\uparrow\uparrow> -0.7013|\uparrow\uparrow\downarrow>$; which is actually -$|1>$ of linear triple dot qubit.

When $t_{13} = 0$ is small, we get similar curve to the Heisenberg model. From Hubbard model, we see that t_{13} gives extra tunability of energy gap between ground state and first excited state. However, even $t_{13} = 5t_{12}$, the energy diagram does not change drametically.

Thus we can still use the Divencenzo type exchange only qubit proposal. Ref.[HK05] proposed a realization of the three spin coded qubit in this type of triple quantum dot. In their proposal, the gate voltage will result change in single particle wave function in the dots, and the electron-elelctron interaction translate these changes into manipulation of coded qubits.

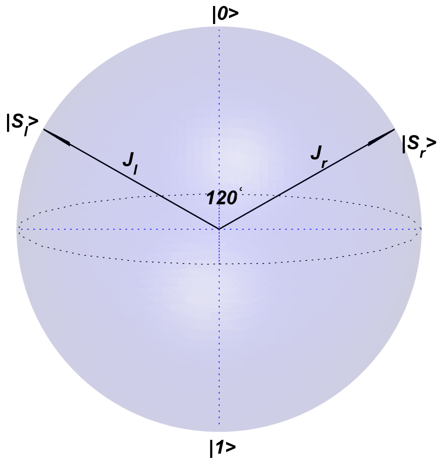

Figure 6.3: Bloch sphere defined in the subspace of the doublet states $|\Delta'_{1/2}>$ and $|\Delta_{1/2}>$. The $|0>$ and $|1>$ is defined to be $|0>=\frac{1}{\sqrt{6}}(|\downarrow\uparrow\uparrow> -2|\uparrow\downarrow\uparrow> +|\uparrow\uparrow\downarrow>)$ and $|1>=\frac{1}{\sqrt{2}}(-|\downarrow\uparrow\uparrow> +|\uparrow\uparrow\downarrow>)$. In the limit of $J_{12}/J_{23}(J_{23}/J_{12}) \rightarrow 0$, the doublet states $|\Delta'_{1/2}>$ corresponds to $|S_r>$ ($|S_l>$). They are 120° apart in the Bloch sphere.

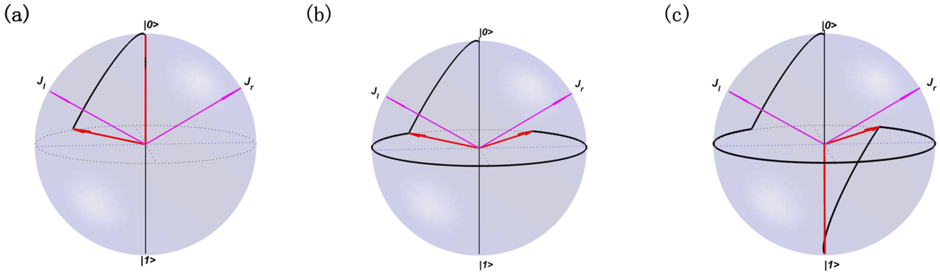

Figure 6.4: Implementation of exchange only qubit proposed by Divencenzo[**?**].The Bloch sphere is defined in the qubit formed by $|0>$ and $|1>$. The magneta arrow mark the rotation axes of J_l and J_r. First the qubit is initialized to $|0>$. (a) Then qubit was pulsed to near detuning ϵ_+ where only J_l is on. $|0>$ will rotate around J_l till fall over the xy plane after a time τ_1. (b) The device is then pulsed back to zero detuning where $J_l \times cos(\pi/3) = J_r \times cos(\pi/3)$. The total exchange gives a σ_z rotation. The state rotates around z axis in the xy plane for a time τ_2. (c) Finnaly, the device is pulsed to ϵ_+ again, similar to step (a), the state rotates with J_l and reach south pole $|1>$ after a time τ_3. The red arrow mark the initial state and final state during each step in the bloch sphere. The black curve plots the trajectory during each step. $J_l(J_r)$ is also dennoted as $J_{12}(J_{23})$.

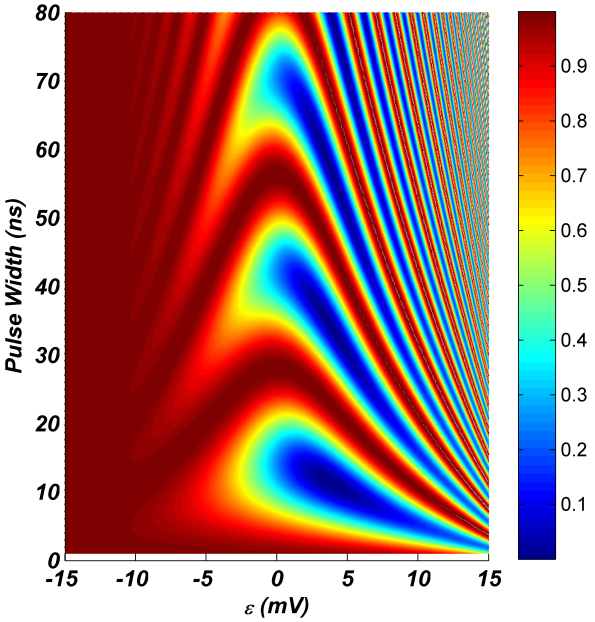

Figure 6.5: Numerical simulation of coherent manipulaton using exchange interactions. State $|S_l>$ is prepared first at charge regime (2, 0, 1), then is pulsed to ϵ_s along the detuning line in charge regime (1, 1, 1). After a time τ_s, state is brought back to (2, 0, 1) for measurement. The color bar shows the propability of retuning to the $|S_l>$ state after pulse sequence. Parameters used in this simulation is as follow: $\epsilon_{\pm} = \pm 18mV$, level arm $\alpha = 0.04$. $t_{12} = t_{23} = 30\mu eV$. The function for expanding J_{12} and J_{23} in terms of ϵ and tunnel coupling can be found in the supplementary material of Ref. [MBT13a].

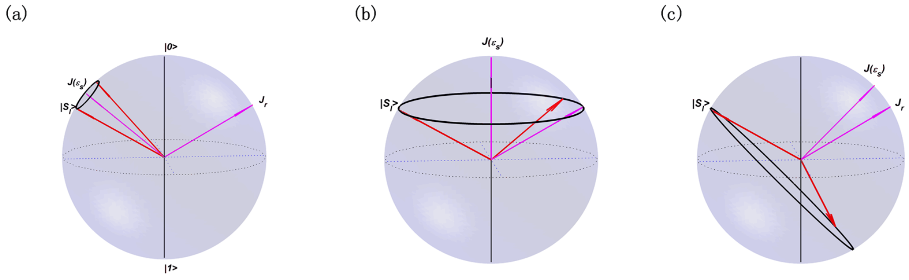

Figure 6.6: Bloch sphere representation for the numerical simulation in FIG. 6.5. Red arrow marked the state, the black curve denotes the evolution trajectory at different detunings. (a) Less negative detuning when pulse height is small . (b) Zero detuning (c) Positive detuning

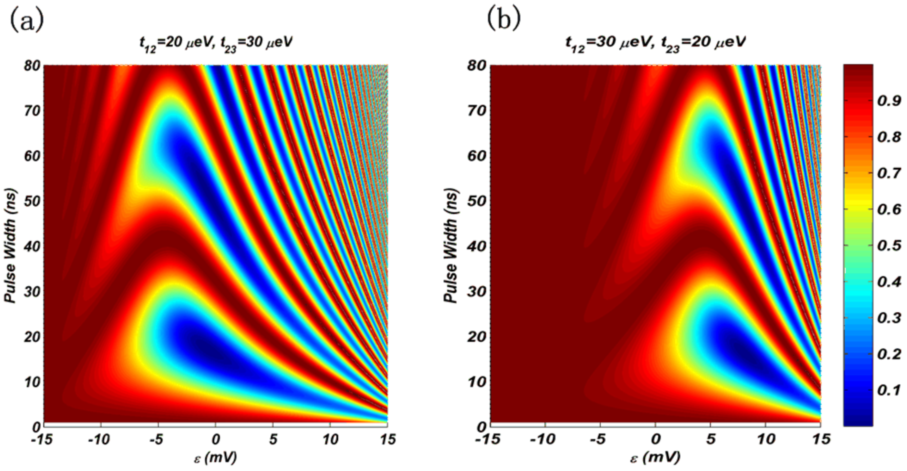

Figure 6.7: Numerical simulation of coherent manipulaton using exchange interactions for asymmetrical tunnel couplings. Same pulse sequence as used in FIG. 6.5. (a) $t_{23} < t_{12}$. (b) $t_{12} > t_{23}$.

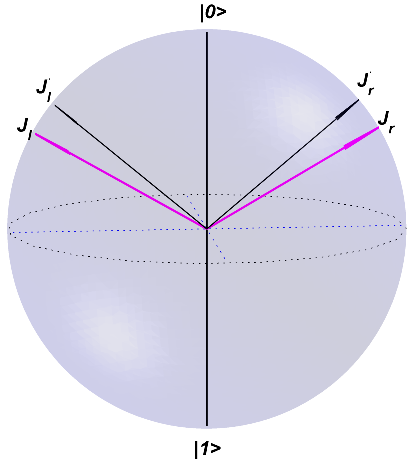

Figure 6.8: Plot of rotation axis with J_{13} present. The black arrows mark the direction for the new rotating axis $J_l'(J_r')$. $J_l(J_r)$ is plotted for comparison.

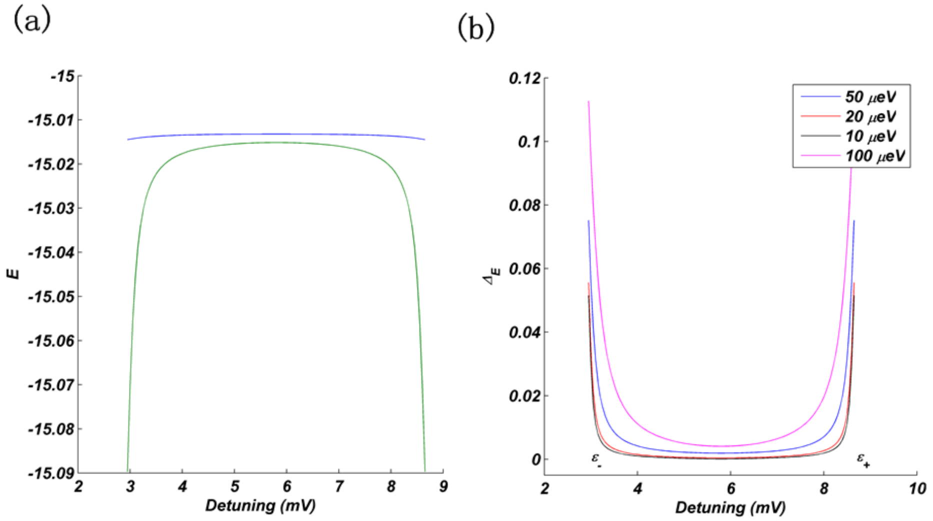

Figure 6.9: Calculation of ground and first excited state energy along the detuning line. (a) Energy calculated with t_{12} and $t_{13} = 20\mu eV, t_{13} = 50\mu eV$, $U_1 = U_2 = U_3 = 7meV, V_{12} = V_{13} = V_{23} = 2meV$. (b) Energy difference between ground state and first excited at different t_{13}.

CHAPTER 7

Time resolved electron spin and charge dynamics in coupled triple quantum dot by pulsed-gate technique

7.1 Device description and Pulse sequence for spin dynamics

We wil first quickly describe the triple quantum dot device we will use in this chapter. Then we will present our effort of using various pulse sequence for detecting the spin dynamics related for exchane-only qubit and discuss the experimental results.

7.1.1 Device stability diagram

The device has the same structure of the device of HD5, the one we did quadruple tuning experiments.TWe name it as OB1. SEM diagram can be referred to Chapter 2. The device is cooled in the Janis500 Dilution fridge. Depleton gate V_L is connected to the coax cable B while V_R is connected to coax D with cold biastee inserted. FIG.7.1 shows the stability diagram as a function of depletion gate voltage of V_L and V_R using the modulation charge sensing method. We can identify three sets of lines. The blue dash line markes the charge transition in left dot. The red dash line strongly couple with the gree dash line which we believe belongs two right dot and middle dot respectively. Unfortunately, we are unable to tune the coupling between middle and right dot from strong to weak. However, we found depletion gate V_T can be used to tune the coupling between middle/right dot and left dot. Another special charging line is marked by magneta arrow. This line has slightly different slope from the left dot charging line. And it move with different speed from the left dot charging line when we tune V_T. We suspect this line comes from the left side but close to

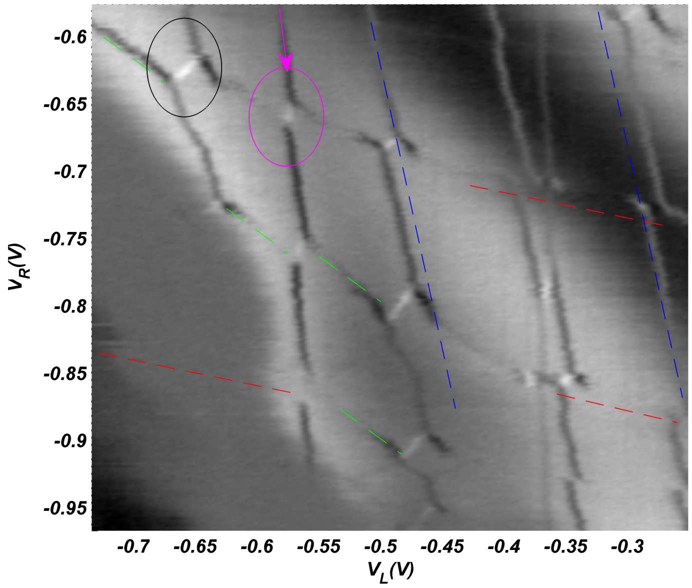

Figure 7.1: Charge stability diagram in voltage space of V_L and V_R. The blue dashed lines mark the left dot charging line. The red dashed lines that strongly couple with the green dash line mark the position for right dot and middle dot respectively. The line labeled by the arrow belongs to a dot between left dot and the left barrier.

the left barrier. We call it the "Pleft" dot. Based on the charging line slope, we estimated the locations of these dots as seen in FIG. 7.2.

From the spacing of the charging line, we estimate the charging energy of the left and right dot to be $3 \sim 5$ meV. That of the "Pleft" and middle are even larger. This suggests that we are near the last few electron regime. The electron numbers in each dot are less than ten.

We also observe white interdot transition lines. We will discuss some very interesting phenomena near the interdot transition circled by black and magneta ring, which we name as spot A and spot B.

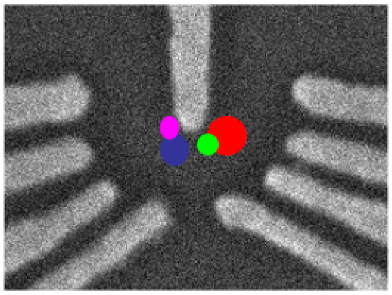

Figure 7.2: Possible dots configuration respect to the charging lines in FIG.7.1. The color of the dot corresponds to the charging line with same color

7.1.2 Pulse sequence studying tunneling rates

At roome temperature, the cooner wires are tested to have a bandwidth of 50MHz while the coax cable B and D can supply pulses up to 10GHz. However, at low temperature, we found the coax line equipped with cold bias tee does not have good conduction for high frequency. Thus for most of our experiment below 1GHz, we add pulse to gate BR instead of R. It doesn't affect most of the experimental results. The consequence is discussed in detail in the context.

With the aim of developing electron spin and charge manipulation techniques towards the full qubit control, we first try to study the various pulse effect on stability diagram. The area we are interested is marked by the black circle in FIG. 7.1. We name it as Spot A. This anticrossing involves mixing of energy levels from left and middle dot. The electron numer is just an estimation and for illustration purpose.

We use Tektronics Arbitrary waveform generator model 520. It has two output channels. The maximum clockrate is 1GHz. By connect both channel to two plunger gate through coax cable, we can realize any pulse direction in the voltage space of V_L and V_R. It also comes with the function generator mode, which supplies the common sine, square and pulse mode.

FIG. 7.3 (a) shows the stability diagram with a square pulse added along the detuning

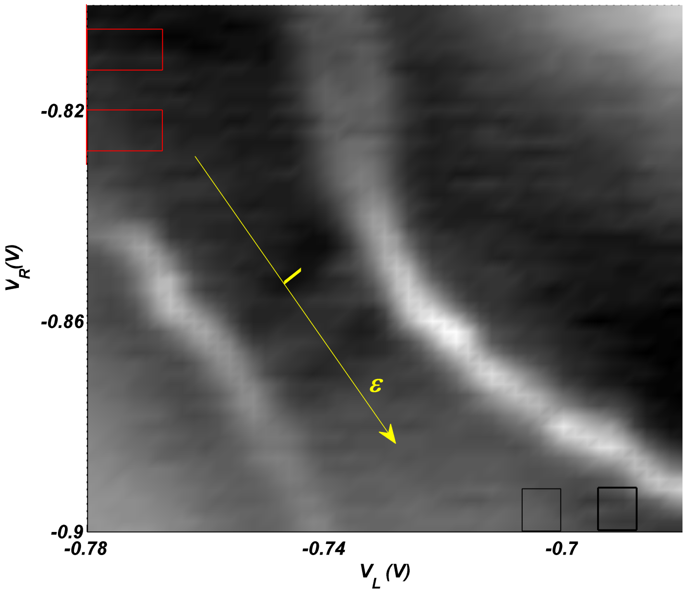

Figure 7.3: Stability diagram of spot A with 100kHz square pulse added in the detuning direction. The black square pulse is added onto V_L and the red square pulse added onto V_{BR}

direction. The pulse form on different channel is illustrated as black and red square wave along the axis of V_L and V_{BR} respectively.The pulse height for V_{BR} is twice of that on V_L. The pulse frequency is 100 kHz. We see the original interdot transition line now has a copy vertical to the detuning direction. The distance between the center of the two interdot transition line is $\Delta V_{BR} = 0.014V$ and $\Delta V_L = 0.007V$ which is exactly the pulse height added divded by a 30dB attenuator. We repeat this experiment up to 5MHz and still see clear split. This demsontrated that the cooner wire and coax B works well at least up to 5MHz.

7.1.3 Pulse sequence used for detecting electron spin related dynamics

We follow the literature [JPT05, MBH12], using the triangle pulse to detect the spin blockade area. The triangle is defined by three points: M, P and S. M sits in the (N,0,2) regime. The pulse sequence starts with pulse from M point to P point. The system will undergo charge configuration from (2, 0, N) to (1, 0, N) by pushing one electron out. The time duration for this pulse period is determined by the tunneling rates which is normally around few MHz. Then we pulse from point P to point S, (1,1,N) and stay at S for some time. This time should be longer enough for one electron to tunnel in while much shorter compare to the hyperfine mixing time. During this initilization process, the system will have three quarters of probability loading into a triplet state with left one quarters probability of forming a singlet state. Finally we pulse back to M and stay there for around 80% of the pulse cycle for measurement. The singlet state will tunnels to singlet (2, 0, N) state while the triplet (1, 1, N) will get stuck due to Pauli exclusiton principle. This charge configuration difference will be detected by the charge sensing channel nearby. The pulse cycle should be smaller than the triplet singlet relaxation time. We are recording the differential conductance of the QPC channel with a time constant normmaly set at $100 \sim 300ms$, thus the result is an averaging of hundreds of thousands of pulse cylces. FIG. 7.4 (b) plots the pulse waveform applied onto the plunger gate V_L and V_{BR} respectively.

We turned on the triangle pulse and scan the stability diagram. If there is spin blockade, we should be able to see either a triangle regime or a trapzoid area on the (2, 0, N) side

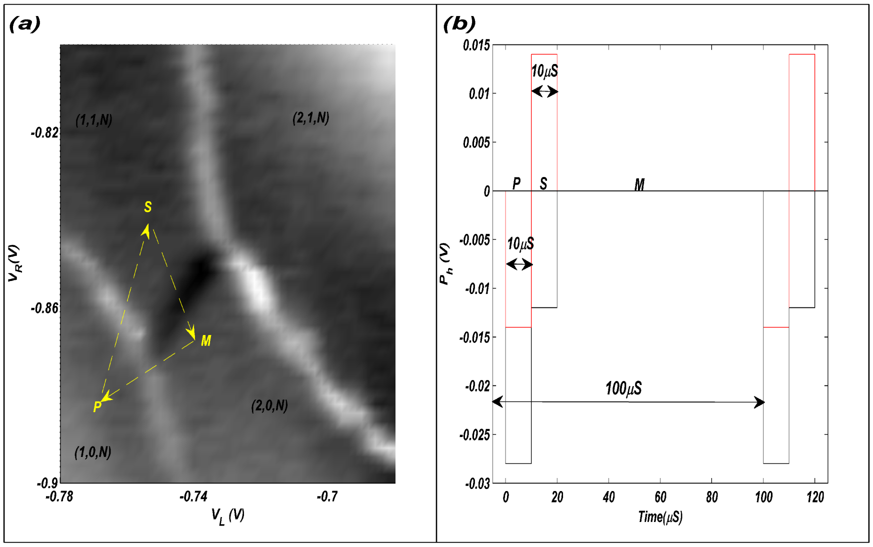

Figure 7.4: (a) Interdot transition area between left and middle dot. M, P and S define a triangle which used for identify spin blockade regime. (b) AWG two channel pulse direction

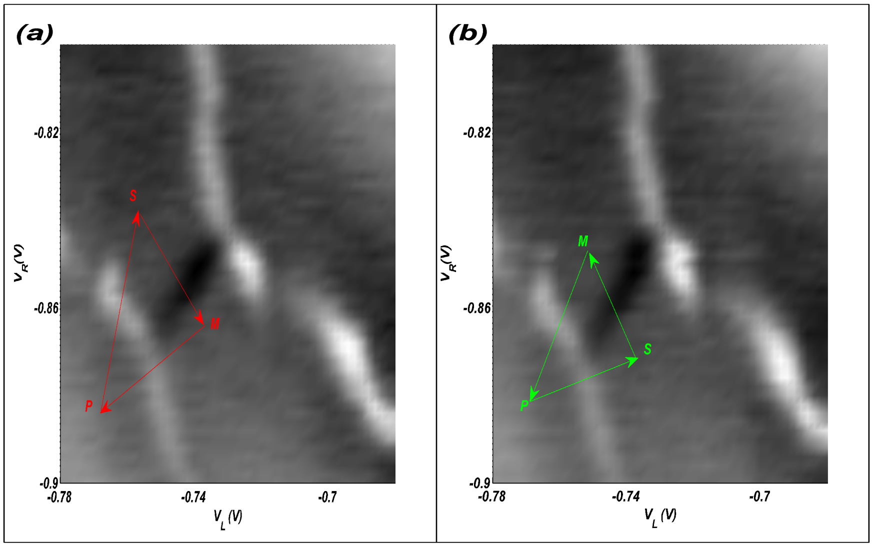

Figure 7.5: (a)Stability diagram with triangle pulse in clockwise direction. (b) Stability diagram with triangle pulse in anticlockwise direction.

as seen in [JPT05, MBH12]. Since we are not in last few electron regime and there is no conclusive argument about the spinblockade. We tried triangle pulse in both clockwise and anticlockwise direction. FIG.7.5 displays the experimental result at both conditions.

We didn't find any signature of spin blockade at this anticrossing area. It could be this area is not spin sensitive or our pulse parameters are not right. However, we do observe some pulse induced effect in FIG.7.5. The middle dot charging line splits into two. This is quite interesting since for the triangle pulse, the device will spent more than 80% of the time at M point. We suspect this phenomena might be electron charge dyanmics induced by short pulse and asymmetric tunneling barrier. Studying this effect is quite importantl for us to undertand this dynamics of the system.

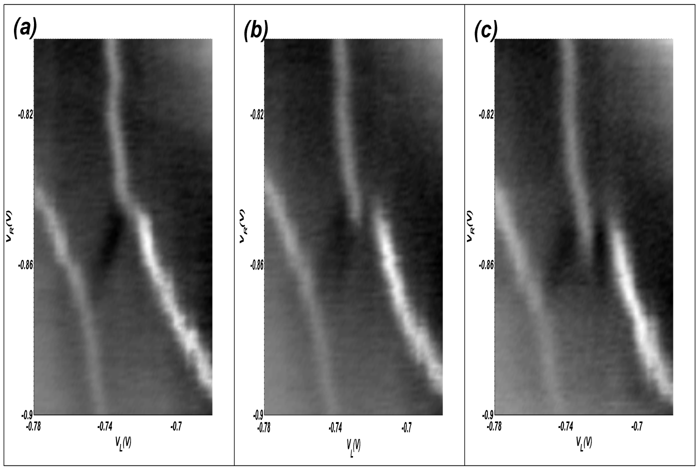

Figure 7.6: Stability diagram with pulse in diagonal direction. The pulse width is 5ns and the repetition rate is 20MHz. The pulse height on V_L is 6mV, 12mV and 18mV respectively in (a), (b) and (c)

7.2 Electron charge dynamics

7.2.1 Electron charge dynamics in incoherent limit

To understand the charging line split effect, we first simplify our pulse from triangle to diagonal pulse. This can be easily done by chaning the pulse duty cycle in the square pulse used in FIG. 7.3 from 50% to 10% with vairous repetition rate. No obvious pulse effect has been seen for repetition rate of 100kHz. However, clear split is seen when we increase the repetetion rate to 20MHz, FIG. 7.7. To verify this split, we first study the pulse height dependence as seen in FIG.7.7.

This split can be understood as illustrated in FIG.7.7. The background stability diagram is the same one as in FIG.7.7 (c). The charge number in each dot is marked for illustration only. Solid color lines mark the position of original charging line. When the pulse is turned on, from right to left, at the dash red and yellow lines, the device is pulsed temporarily to

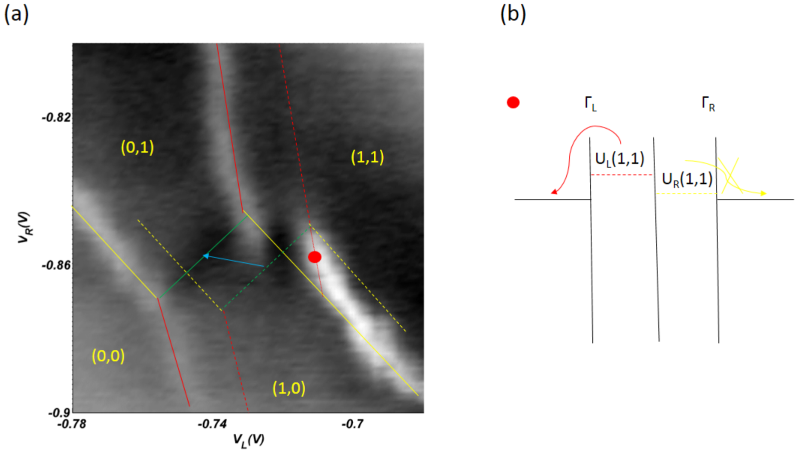

Figure 7.7: (a) Stability diagram with pulse on. Solid color lines mark the position of original charging line without pulse. The dashed color lines mark the charging line during pulse. (b) Energy level at red spot.

solid line position. If the tunneling rates is high enough, one electron will be pushed out from the quantum dot. the QPC current is a time ensemble averaging. Thus we don't see the pulsed induced copy of charging lines. In our system, the tunnel rate Γ_L for the left dot(red line) is much higher than the middle dot(yellow line, Γ_R). At the red point, the system will jump from (1,1) state to (0,1) because the left tunnel barrier is much more transparent than the right barrier. Thus we see dotted red line. However, eventually, the electron from the right dot will tunnel into the left dot and form the more stable state, thus why we see the portion of the green dash line. We found that the arrow which connecting the center of the two interdot transition line is not aligning the programed pulse direction. This is due to the larger attenuation of cooner wire at high frequency limit.

At this pulse width range, one might expect to see charge qubit oscillation depending on the decoherence and relaxation rate of the charge qubit. Thus we also tried to decrease the pulse width to 1ns. However, the split starts to fall off. This could be due to various reasons. One is that the tunnel coupling is very large at this place which we deduce from the width of the interdot transition line and curvature of the charging line near anticrossing. The possible oscillation frequency is much higher than the resolution of the AWG520 output. Second is the large attenuation from the cooner wire as expected and it is hard to synchronized two channels at short time scale. Third the visibility is not good enough. Thus what we obeseved here is probably in the incoherent limit of charge dynamics. Similar data has been seen in [HMT10].

7.2.2 Coherent Oscillation in MHz range

As stated in Chapter 1, the charge qubit oscillation frequency is determined by tunnel coupling magnitude. In order to detect charge oscillation in the limit of current labortory facility, we try to first look for place with very weakly tunnel coupling. We suspected spot B in FIG. 7.1 has highest possibility. The short interdot transition line suggests small interdot coulomb repulsion and the sharp anticrossing suggests weak tunnel coupling. The hubbard model fitting suggests a upper bound of tunnel coupling of $40\mu eV$, equvalent to 10GHz.

We first study the slow dynamics. FIG. 7.8 displays the stability diagram with a diagonal pulse along the detuning line from lower right to upper left, marked by the red arrow. The pulse has a duty cycle of 5% with a repetetion rate of 50kHz. We see similar splitting as in spot A. The tunneling rates of right side dot is known to be small. It suggests that the physics here might be the same as in spot A.

We next studied the pulse width dependence of this pulse induced feature. We record the differential conductance of the QPC along the detuning line as a function of applied pulse width with 50kHz repetition rate. Supprisingly, we see the pulse induced charging line oscillate with pulse width up to $3\mu S$, FIG.7.9(a). FIG. 7.9(b) plots out the pulse width dependence along the black dash line in FIG.7.9 (a). This trace is after 20 times averaging.

Close look at the oscillations reveals two oscillation frequencies. One is the slow oscillation in the time scale of $.5 \sim 3\mu S$. The other one is much faster oscillation below $1\mu S$. Fourier transform shows two dominant frequency of 2MHz and 7MHZ. We zoom in the time scale

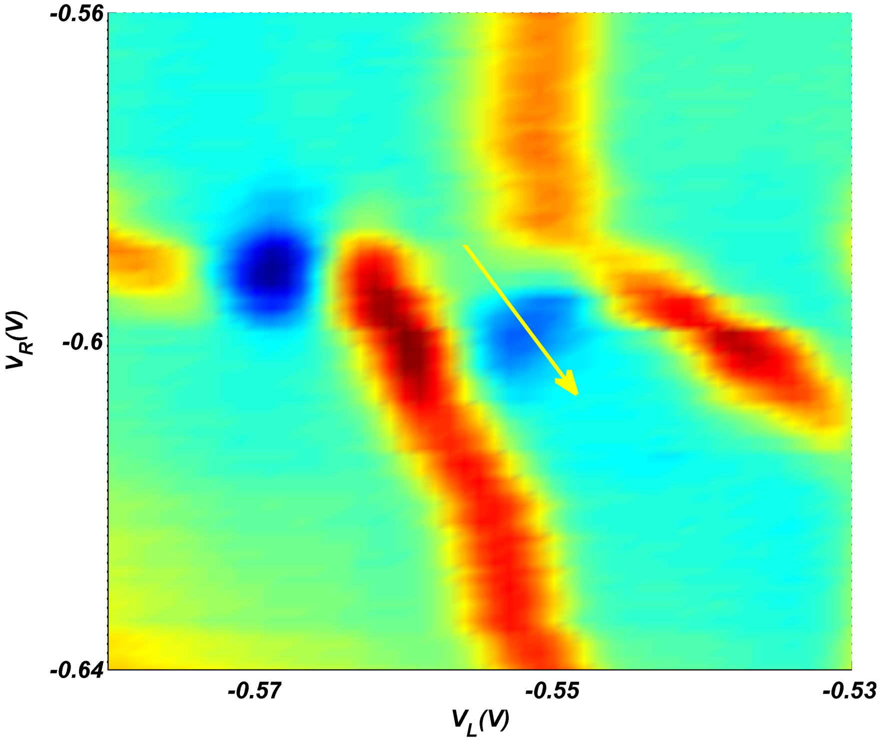

Figure 7.8: Stability diagram with pulse added along detuning direction. Pulse direction is marked by the yellow arrow. The pulse width is 1μs and the repetition rate is 50kHz. The pulse height on V_L is 18mV

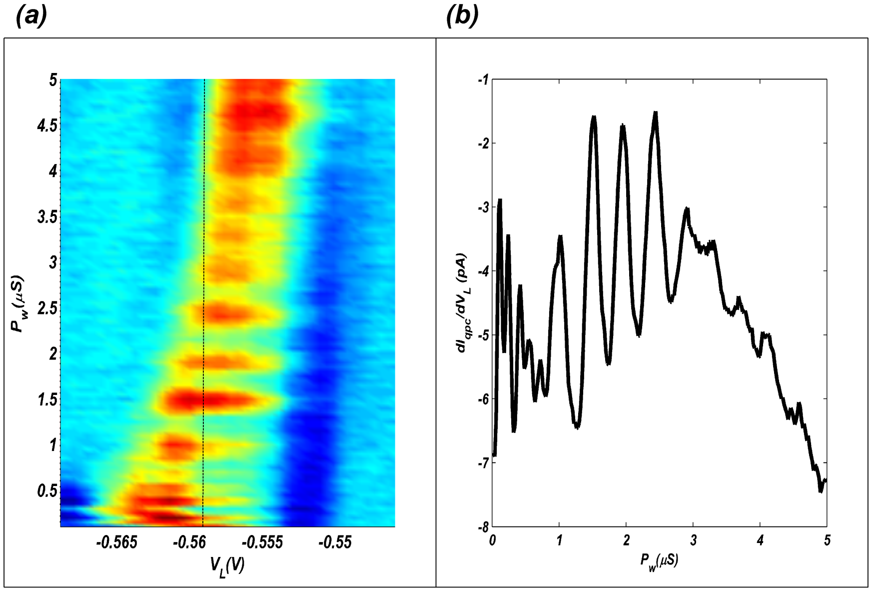

Figure 7.9: (a) Oscillation of the pulse induced charging line as a function of pulse width along detuning. Pulse height is 7.5mV on V_L and 15mV on V_{BR}. Repetition rate is 50kHz. (b) Single oscillation trace as a function of pulse width at the black dash line on (a).

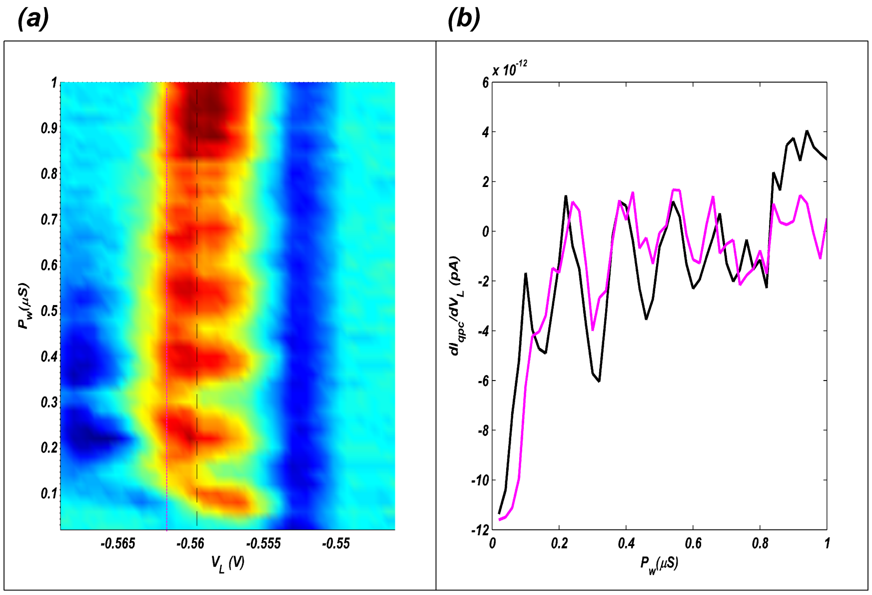

Figure 7.10: (a) Oscillation of the pulse induced charging line as a function of pulse width near detuning. Pulse height is 7.5mV on V_L and 15mV on V_{BR} . Repetition rate is 50kHz. (b) Single oscillation trace as a function of pulse width at the black and magneta cut on (a).

of $100ns \sim 1\mu S$ and retake the pulse width dependence diagram seen in FIG. 7.10.

We see very clean oscillations of the pulse induced charging line and the second interdot transition line. The oscillation repeats the fast oscillation of FIG. 7.9. Both of these oscillations cannot be simply explained by charge qubit oscillation. Previous study in charge qubit in Si/SiGe double quantum dot has shown the coherence time $T_2^* \sim 2.1ns$ near detuning zero point, which is much shorter than our observation. We're not certian the origin about these oscillations at this moment. We suspect this strong oscillations is related with electron spin dynamics. We temporarily consider only two dots, the "pleft" and right dot, are involved here. FIG. 7.11 (a) illustrates the stability diagram at spot B. The electron number is for illustration purpose only. The black arrow marks the pulse direction, pulsing from red dot to light blue dot. At the proposed configuration, we are pulsing from (0,2) singlet state to

(1,1) regime (light blue dot). At blue dot, the rotation axis is determined by the exchange interaction and the hyperfine interaction. The state will evolve like in FIG. 7.11. After the pulse cycle, the system is brought back to red dot. FIG. 7.12 illustrates the possible readout scheme. If the system is in S(1,1) state, the electron on the left dot will tunnel to right dot and form the ground S(0,2) state. If the system is in T(1,1) state, it cannot tunnel to S(0,2). At this voltage setting, the chemical potential level of (1,1) state is close to the Fermi level of reservoir. The electron of left dot easily tunnels to the reservoir and form a (0,1) state. The right barrier of the dots is very opaque. It is hard for the electron to tunnel to the right dot and form (0,2) state. Thus instead of seeing QPC current difference of (1,1) and (0,2) state, we see oscillations between (0,1) and (0,2) state. It has to be note that the oscillation signal we observe here is much stronger than the raw data of similar oscillation in Ref. [MBH12]. The asymmetry tunnel barrier might provide a new way of readout spin states.

The above argument might explain the observed fast oscillations at short pulse duration. The double dot physics cannot explain the 2MHz oscillations. We suspect the observed oscillations of two frequencies might be related with triple dot physics. Detail study and analysis is defintely needed in the future.

7.2.3 Coherent charge oscillation

Now we try to explore if this place is good for charge qubit manipulation experiment. It is unlikely to synchronize two pulses at high frequency. Thus we apply pulse to one gate in the following experiment. The clockrate of AWG520, 1GHZ, limit us from study possible oscillation with much higher frequency. Thus we switch the signal generator to Agilent 81134A pulse generator. When we consider two quantum dot coupled together, the Hamiltonian can be describe as follwing.

$$H = \begin{pmatrix} \epsilon/2 & t_c \\ t_c & -\epsilon/2 \end{pmatrix} \tag{7.1}$$

FIG. 7.13 illustrates the energy diagram and corresponding qubit in bloch spere. Here (1,0) and (0,1) is just for simlicity. In general, it is valid for interdot transition between (N+1,M)

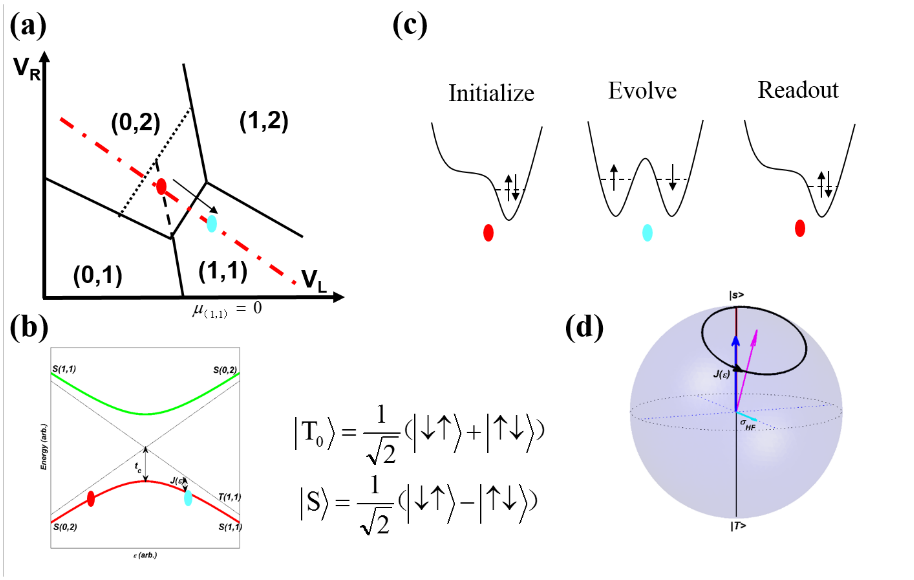

Figure 7.11: (a) Schematic stability diagram in the regime of (0,1)-(1,1)-(0,2). Black arrow marks the position of pulse direction. Red dot dashed line is the detuning line. The black dashed line is the extension of the left dot charging line. The distance between the original interdot transition line and the black dotted line is defined by the pulse height. (b) Energy diagram of a singlet triplet qubit near transition of (1,1) and (0,2). (c) Schematic diagram of dot potential profile during pulse cylce. (d) State evolution on the Bloch sphere with exchange interaction and nuclear field both present.

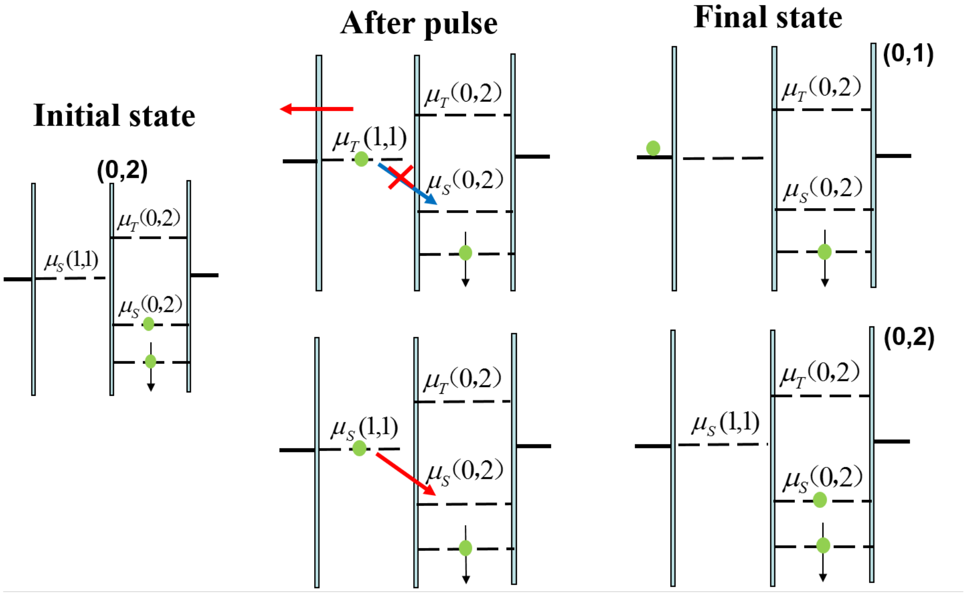

Figure 7.12: Energy diagram of a double dot in the pulse cycle. The system is initialized in S(0,2) state, and then pulsed to the (1,1) configuration. After pulse duration, it can be either in T(1,1) or S(1,1) state. The S(1,1) state tunnels to S(0,2) state. The T(1,1) state becomes (0,1) state with the electron in the left dot tunnelling quickly to the reservoir while the electron does not have enough time to tunnel to the right dot.

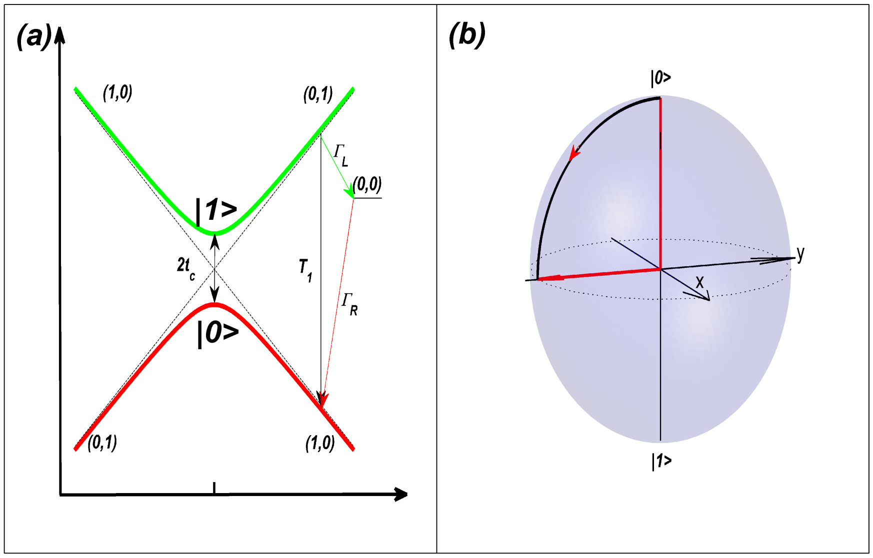

Figure 7.13: (a) Energy levels near the interdot transition line ($\epsilon = 0$). The tunnel coupling induced symmetric ground state and antisymmetric excited states are defined as the $|0>$ and $|1>$ of the charge qubit. (b) Charge qubit in Bloch sphere representation. t_c defines the x-axis rotation.

and (N,M+1) as long as the energy gap is large enough.

In the bloch sphere repersentation, the tunnel coupling will provide x axis rotation. If we initialize the state in (1,0) and then pulse near the $\epsilon = 0$, the (1,0) is nolonger the ground state and will evolve under the new halmitonian at $\epsilon = 0$. The state will be a superposition of (1,0) and (0,1) with time dependent coefficient. When we pulse the system back, the difference will be captured by the charge sensing channel. The QPC signal is doing time ensenble averaging. The signal visibility highly depends whether every pulse start with a pure (1,0) state. This is determined by the relaxation time,T_1, of the system. In GaAs charge qubit, T_1 is measured to be 16ns [PPL10]. In a Si/SiGe charge qubit [SSW13], the author used 40MHz as the repetition rate.

As stated earlier, the coax connecting gate R doesn't have good connection. We added a

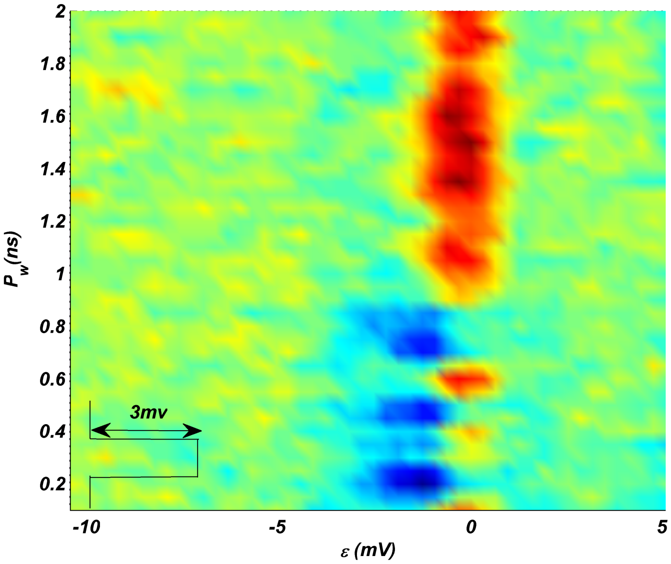

Figure 7.14: Fast oscillation seen near the red detuning line. A 3mV short pulse is added to gate L.The repetition rate is 10MHz.

3mV fast pulse to gate L FIG. 7.14 presents the experimental result. Differential conductance of QPC channel is recored along the detuning line as a function of pulse width from 100ps to ns. Pulse width step is 20ps. At every pulse width, the 1D scan is averaged 10 times. We found that without averating, the signal is totally smeared out by noise. The modulation signal for charge sensing is also reduced from 2mV to .25mV.

This oscillation strongly suggests the possibility of forming a charge qubit at this interdot transition. When we increase the pulse height to 5mV, the oscillation is hardly seen. This is because, we can no longer pulse to the detuning line. The strong decoherence away $\epsilon = 0$ might prevent us from seeing the oscillations. In the future, we will fix the bad connection induced by the cold bias tee and repeat experiment by adding pulse to gate R which has much large play room. Thus we can perform the two dimensional scan in the space of pulse width and pulse height. Echo experiment can also be done as in [SSW13]. We should be able to deduce the T_2^* of the charge qubit in silicon MOS quantum dot system.

CHAPTER 8

Conclusion and Future Plan

the past decade has been a very productive period for solid state quantum information. Since the proposal of Loss and Divincenzo in 1998 to use spin states of electrons confined in semiconductor quantum dots as a basis for information processing, rapid progress has been made in fabricating single, double, triple and even two coupled double dots and coherent manipulation of electron charge and spin states. Up to now, the proposed Loss-DiVincenzo qubit utilizing single electron spin zeeman splitting has been successfully realized in GaAs quantum dots. Relaxation time $T_1$and decoherence time T_2^* are characterized. Lots of experimental work and theoretical work have been done to understand various qubit decoherence channel. This stimulates the research in Si based system, in which T_2^* is predicted to be much longer due to much less spin-orbit coupling and hyperfine interaction and no piezoelectric electron-phonon interaction. Now several groups have reported fabricating well controlled single and double quantum dots. More excitingly, coherent manipulation of charge qubit and singlet triple qubit in Si/SiGe based double quantum dot has been demonstrated by different groups last year. The measured coherence time T_2^* of the singlet triplet qubit is 360ns which is much longer compared with 10ns in GaAs quantum dot. This largely enhanced the confidence of the whole community. About five years ago, researchers from several groups start to develop triple quantum dot with the aim of making a exchange only qubit. The merit of exchange only qubit is that it depends purely on the exchange interaction of electron spins so that it benefits from the long coherece time of electron spin compare to charge. Additionally, all the proposed qubit operation can be done electrostatically. Earlier this year, research group at Havard University reported the first experimental demonstration of coherent oscillation in a GaAs triple quantum dot. Later, they announced the new type of operation which they called the resonant qubit which they using RF microwave instead of short pulse to do the coherent manipulation.

The goal of combining the advantage of full electrical pulse control and long decoherence time of Silicon base material is the origin of this thesis. The goal of this project is to first develop and fabricate a triple quantum dot device which can reach last few electron regime on silicon metal-oxide-semiconductor (MOS) material. The second is to demonstrate coherent manipulation tuned by exchange interaction. For the past five years, our research group has been focused on developing and studying quantum dots based on Si MOS. M. Xiao first demonstrated a few electron single electron and developed a high yield fabrication recipe [**?**]. Subsequently, M. G. House fabricated the double quantum dot. These demonstrate that Si MOS quantum dots, even with unique fabrication challenges, are able to confine and control electrons in much the same way of a GaAs quantum dot. Lots of time was spent designing and testing the depletion gate layout with goal of producing most controllable few electron triple quantum dot. And for all the device we tested at 200mK, the ring like structure we showed in Chapter 2 produces the most repeatable charge stability diagram.

The tunnel coupling between quantum dots determines the energy scale and qubit coherent manipulation frequency. We performed the tunnel coupling measurement in both double and triple dot. The experimental result shows we can realize strong and weak coupling in our dots. We also developed hubbard model for both double dot and triple dots. The hubbard model natually includes the electron hopping term which help us to extract the tunnel coupling by fitting the experimental charge stability diagram.

The coherent oscillations demonstrated in GaAs triple quantum dot is for very idea case considering only neighboring exchange interactions. We implement the original DiVincenzo proposal and consider a more general case with three exchange interaction all on. We numerically calculated the energy spectrum and find out that the proposal should be valid in a large range of exchange interaction magnitude.

For the perpose of performing coherent oscillation and minimizing noise in our measurement set up, we spent quite amount of time setting up the Janis500 Dilution fridge. We installed four coax cables and 32 cooner wires into the fridge, providing the possibility of testing two device within one cool down. This minimize the risk of faliure. We also designed various kinds of chip holder for the purpose of minimizing cross talk, transfer risk, and pulse attenuation induced by intrinsic parasitic capacitance. All these lead to the success of observing the coherent oscillations shown in Chapter 7.

Charge impurity and interface defects have been long term problem in nano scale device especially in quantum dots. The existance of impurity can some times completely change the depletion gate behavior. Active defect provide source for charge noise. We developed bias cooling technique to minimizing the difference in local electrostatic field induced by different cool down. We believe this method should be thoroughly studied and should provide more control over our device.

In summary, we've developed quite stable fabrication procedure that produces stable few electron triple quantum dot on Si MOS. We also demonstrate our ability of performing coherent oscillation in a triple quantum dot device. Eventhough we are still several steps away of realizing the exchange-only qubit manipulation, we are very confident about the future.

In the near future, we first want to get better control of our device. The new lab members already started trying new recipies of squeeze the size of our current quantum dot and higher possibility of reaching last few electron. Another approach is to take new wafers with much thinner SiO_2. This in principle will decrease the screening from top gate and increase the field strength from the depeltion gates to the 2DEG. We are hoping combining these two approaches, we will greatly increase the quality of our device in terms of forming a well controlled triple quantum dot

Once we have a device with better control, the next step is to realize the two axis control of an exchange only qubit. And furthurmore, coupling two triple quantum dot together and study the two qubits operation.

We should acknowlege that the study of solid state qubit system has been moving rapidly. There is every reason to believe that progress will continue into the future. The ability of direct prepare, maipulate and measure quantum superposition or entangled states will also motivates other scientific study.

Last, I want to emphasize that the triple quantum dot device itself provides a good platform for studying various kinds of basic physics principles, such as the QCA effect we discussed in Chapter 5. Furthur more, the unique valley degree of freedom of silicon should provides much interesting physics.

APPENDIX A

Fabrication recipes

Here is a summary of fabrication procedures in detail and a recipe. Common problems during fabrication are also discussed.

A.1 Si MOS quantum dot fabrication procedures

Si MOS based quantum dot has been developed in our lab for quite few years following the pioneering work from Dr. Ming Xiao and has been successfully transferred to different generations of graduate student. Following we will discuss the procedure of fabricating triple quantum dot device in detail.

We first started by patterning markers on clean Si/SiO_2 wafer. The Si/SiO_2 used in our lab is made by Wafer World, InC. with different diameters. These wafers have a 300um boron doped silicon layer followed by 50 nm thermally grown SiO_2. Both 3.5 inch and 2 inch wafer has been used in fabrication process. The doping level of these two wafers are $10^{16}cm^{-3}$ and $10^{15}cm^{-3}$ respectively resulting in resistivity difference. It has been shown recently that the more highly doped wafer give better device stability. No conclusive result has been obtained that why the 3.5 inch wafer performs better. It has been suspected that the lightly doped wafer has more charge impurity which make the wafer less uniform. This leads to the variance in device performance.

Wafer is first cleaned by ultrasound in solvents TCE/ ACE /IPA for 1 mins each. Then square aligned markers are patterned by double layer photoresist, normally AZ5214. The patterned wafer is etched in NH4F:HF (buffered oxide etchant/ BOE) for 60 secs. Each device area is typically designed to be $3.5mm \times 4mm$. Double or triple layer photoresist pattern are used here to avoid any pinhole in non-marker area.

Next, another photolithography is done to open windows for ion implantation of the ohmic contacts. These ohmic contacts are heavily doped with phosphorus donors so that the doped area are degenerate and will conduct even at low temperatures. The dosage used is $2 \times 10^15cm^{-2}$ at a kinetic energy of 40KeV. After ion implantation, wafer is cleaned thoroughly and then transfered to high vacuum oven and annealed at $950°C$ for 35mins to repair implantation damage and activate the dopants. The oven vacuum is crucial in this step. Poor vacuum will result in partially or even full conducting wafer that cannot be used. Normally, the vacuum will sustain above 5×10^{-5} torr at $950°C$. The oven needs to be pre-heated at least twice if not been used in two weeks. Rubber plug has to be replaced after being used for half or one year. The oven cannot be cleaned with acetone. Acetone can easily diffuse into the annealing tube at room temperature and evaporate at high temperature thus contaminate the system.

After the ohmic contacts are activated, the depletion gates are patterned. Normally, the depletion gates are patterned in two steps, the larger area are done by photolithography then followed by depositing Ti/Au or Cr/Au (5nm/45nm). Then the wafer are soaked in acetone to lift off unwanted metals. The left inner $100 \times 100um^2$ area are patterned using electron beam lithography (EBL). The EBL can be done in house. The EBL system in our lab is Hitachi S-3000H scanning electron microscope, equipped with Nano-Pattern Generation System. The resist used in our lab is PMMA C2. The depletion gates line width are both determined by EBL system and resist that is used. In our lab, the minimum line width weve ever achieved is 30nm. The line width is of great importance because it determines the field strength according to simple electromagnetism. EBL is also followed by depositing Ti/Au or Cr/Au. The deposition can be done either by thermal evaporator in house or CHA e-gun evaporator in Nanolab at UCLA. The later one gives better vacuum of evaporation chamber and film quality. However, it has also been suspected that the e-gun evaporation will generate x-ray that will damage the SiO_2 layer. So far, no detrimental result has been seen. The depletion gates can also be made once by EBL which requires longer writing time and has been tested successfully both in house and in ISNC vistec machine. However, it is controversial whether the long writing hour will result in more charge impurities in the oxide layer thus affect the device. One has to be aware that the vistec in ISNC facility gives 50nm line width with PMMA A4. To reach smaller line width, double layer PMMA lithography might be used. To remove the residual PMMA, PG remover is used. Detail instruction is included in Appendix. This step is also important because, the cleanness of the SiO_2 surface determines the quality of Al_2O_3 grown in the next step.

After the depletion gates are patterned, the 100nm Al_2O_3 is grown by atomic layer deposition in Cambridge NanoTech, Inc. Savannach-100 ALD system. The cleaned sample is placed on the edge of the chamber with 1 torr flowing high purity N_2 at 20 sccm and 200C. Small amount of H_2O vapor and tri-methyl alumiminum (TMA) are pulsed to the sample surface alternatively which will react with the surface and form Al_2O_3. The final thickness of the oxide usually is about 1.1 angstrom cycle so that 1000 cycles will result in 110nm. The pump connected to the chamber needs to be cleaned every half or one year to maintain the pumping speed so that the exhaust after each cycle will be pumped away completely.

Before we put on the top gate, we needs to open window for depletion gate wire bonding pads and ohmic contacts. The Al_2O_3 is removed by etching in heated Transetch-N etchant solution. The H_3PO_4 inside Transetch_N will etch Al_2O_3 but not Au or SiO_2. The wafer is dipped into the $195°C$ etchant for 5 sec and then rinsed with DI water. This process is repeated twice for complete removal ofAl_2O_3. Rinse in DI water will prevent overbake of photoresist. Then SiO_2 are etched away by BOE at Ohmic contacts window. The original recipe requires this etching step to be done in total dark because light will degrade the ohmic contact quality. However, the previous graduate student Matthew House found it doesn't matter whether the light is on or off.

Last but not least, the sample is annealed in 380 torr of 15% H2 forming gas at $430°C$ for 30 minutes. This annealing step serves several purposes. One is to improve the quality of the Al_2O_3 by removing dangling bonds. Second is to remove the positive charge impurity inside the Oxide layer which is introduced during the e-beam lithography step. It has been found that the annealing will lowering the threshold voltage about 1V. However, there is no obvious difference of quantum dot device performance between annealed and non annealed devices. The annealing step has a couple of drawbacks. The Ti/Au depletion gates tends to become resistive after annealing. This limit the bandwidth of high frequency signals that can be used for coherent manipulation experiments. Annealing can also damage softer metal parts such as aluminum since aluminum has a melting point of $530°C$. The home made oven quality degraded after several years of use. The temperature is unknown. Recently, we added power controller to the system and 80% power has been shown to be perfect. Higher power might result in temperatures higher than $500°C$.

Finally, the top gate is patterned using photolithography followed by thermal evaporation of 300nm Al or Ti/Au. Aluminum deposition requires less power. It is less likely that the photoresist will be overbaked. While the Ti/Au requires much higher power, which is not recommended if using the thermal evaporator in lab. The reason of using Ti/Au is for wire bonding purpose. Wire bonding on top gate can sometimes damage the SiO_2 underearth thus causing leakage. Ti/Au top gate can be connected to chip holder using silver epoxy.

The wafers were diced by hand into single device. Ohmic contacts are made by paste small amount of pure indium onto the contact area using a fine-tip soldering iron. The indium contact is very reliable. The hot iron tip will destroy any unwanted SiO_2 residue. Another way to make ohmic contact is to evaporate Al after etching away the SiO_2 on contact window and the forming gas anneal will help form good ohmic contact.

Then the device was mounted onto a 16-pin chip carrier (Spectrum Semiconductor model number CSB01651). Either A4 superglue or EPOTEK H20E silver epoxy was used to secure the chip to chip carrier. A4 superglue is used so that the the device can be take out easily after soaking in Acetone for an hour if needed. Silver epoxy might give better thermal conduction. The depletion gates contacts and ohmic contacts are wire bonded to the chip carrier using Al wire. One important thing during wire bonding is that one needs to make sure the chip carrier is grounded to the stage.

The recipe presented above is universal in making Si MOS based quantum dot devices.

A.2 Si MOS triple quantum dots fabrication recipe

Following is the standard fabrication recipe for double-gated Si MOS quantum dot devices with Cr/Au metallization for the depletion gates.

1. Etch SiO_2 for ohmic contact windows and alignment markers
    (a) Photolithography to define etch windows (AZ5214 positive recipe), double layer of photoresist
    (b) bake wafer at home hotplate at $120°C$ for 2 mins
    (c) Etch SiO_2 with BOE 1:6, 60 seconds
    (d) Remove photoresist by 20 minutes soak in acetone followed by ultrasound cleaning step
2. Define n^+ doped regions for ohmic contacts to 2DEG by ion implantation
    (a) Photolithography to define implantation windows (AZ5214 positive), double layer of photoresisit
    (b) Implantation of phosphorus ions, $2 \cdot 10^{15}$ cm^2 dosage at 40 keV (Performed by Leonard Kroko, Inc., 2822-D Walnut Ave., Tustin CA 92780).
    (c) Remove photoresist by 20 minutes soak in acetone, followed by O^2 plasma etching 4mins then ultrasound cleaning
    (d) Anneal in high vacuum oven, 35 minutes at 950 °C. Oven needs pre-heated twice in advance
3. Metallization 1: depletion gate leads, SEM alignment marks
    (a) Photolithography to define lift-off windows (AZ5214, positive)

    (b) Deposit 5 nm Cr + 50 nm Au by thermal evaporation or CHA E-gun evaporation
    (c) Lift-off in acetone

4. Metallization 2: quantum dot depletion gates
    (a) E-beam lithography (PMMA 950 C2) to define depletion gates
    (b) Deposit 5 nm Cr + 50 nm Au by thermal evaporation
    (c) Lift-off in PG remover, soaked overnight at 70 °C on home hotplate.

5. Aluminum oxide layer
    (a) Deposit 100 nm Al_2O_3 by ALD, 910 layers
    (b) Photolithography to define Al_2O_3 etch windows (AZ5214, positive), double layer of photoresist
    (c) Etch in Transene Transetch-N @ 195 °C. (hotplate temperature), two dunks in etchant, 5 sec. each
    (d) Remove photoresist by 20 minute soak in acetone

6. Anneal for Al_2O_3 in forming gas (15% H_2, pressure 15" Hg) for 30 minutes in home made small oven, set power regulator to be 80%. Check oven vacuum frequently. This step is not necessary.

7. Metallization 3: top gate
    (a) Photolithography to open lift-off windows (AZ5214, positive)
    (b) Deposit 300 nm Al by thermal evaporation
    (c) Lift-off in acetone

8. ohmic contact: heat clearn indium and paste it onto the ohmic contact window slowly

9. Dice, mount, and bond sample to chip carrier

Note:

APPENDIX B

Common problems in fabrication process

Even though the device fabrication process has been demonstrated very robust. Every member in the lab experience different difficulties while learning and making their own devices. Here, I want to list several common problems that I have seen and provide some suggestions to improve the yield of the process.

B.1 Leakage

Leakage is the most detrimental problem. It has three kinds: top gate leak to contacts, top gate leak to side gate, side gate leak to contacts. The main reason for leakage is due to poor quality of Al_2O_3 and SiO_2. The pinholes of SiO_2 is normally introduced during the BOE etching step. It is recommended to clean the photo lithography mask so that it does not has dust or photoresist residue left. Another possible reason is damage during wire bonding to the top gate. The wire bonding needle is very sharp and can easily cause damage to the SiO_2 underneath. Sometimes, if leakage is found from top to contact. One can gently remove the original wire bonded area of top gate and try to wire bond to other places. This type of cause is very rare in reality. Poor quality of Al_2O_3 is more common during my fabrication. And this is mainly due to not welled cleaned wafer surface before ALD. The common step for cleaning after lift off depletion gates is O_2 plasma, TCE/ACE/IPA/ DI water. Later, I found the DI water step causes most of the problem. Thus I changed the order to ACE/IPA followed by 4 mins O_2 plasma. This helps a lot. Another lesson I learned in the later years of my Ph.D is that cleaning sometimes introduce more contaminations to the wafer. Especially our lab is not cleanroom. Thus minimizing the cleaning steps is actually better than increasing them in terms of to getting clean surface.

B.2 Unresponsive depletion gates

The second common problem is unresponsive depletion gates. Usually, at 4.2K, once the device is turned on, the depletion gate will shut off transport channel around -1.5V. If the gate cannot pinch off the current even at -3V, then the gate is defined as weak gate. In extreme situations, gate might have no response at all. There could be multiple reasons. The simplist one to rule out is bad e-beam lithography. The dosage of e -beam lithography is very sensitive to the PMMA that is been used. After being used for half a year or so, the PMMA tends to become more dense. Also the stigma and focus of SEM affect the lithography a lot. The forming gas during the low temperature annealing step can also cause problem. It has been found the oven sometimes can reach very high temperature, $500°C$. The surface of the annealing stage is not quite uniform after years of usage. This can also result in extreme high temperature at certain places of the wafer. The last cause that is controversial in our group is the high temperature annealing step. It is known that if the vacuum is not good or the annealing tube is contaminated, the wafer will become slightly conducting after 900C anneal. It is suggested to replace the ceramic annealing tube and rubber plug after one year. Pre heat the oven twice and monitor the vacuum during the process. One way to identify if the silicon substrate is conducting is to make two contacts on the back of the wafer and check the resistance between the two contacts. The resistance should increase exponentially and reach infinity if the wafer is cooled from room temperature to 4.2K. More precise result can be acquired through Van der Pauw measurement.

B.3 Unstable Device

This only happened once during all my fabrication years. The device has normal threshold voltage for turn-on. All the depletion gates are good at 4.2k except that the current has large fluctuation, roughly 10%. When the device is cooled to 300mk, the current is jumping crazily. It is suspected, that the random jumping current measured between ohmic contacts is not due to the confinement from the quantum dot but rather the charge traps either at the silicon silicon oxide interface or in silicon substate. The symptom is similar to Na^+ doped Si_MOSFET. However, there is no clue in which step did the wafer get contaminated.

APPENDIX C

Others

C.1 pulse sequence script of arbitrary waveform generator

Various pulse sequences are used to detect and manipulate spin dynamics in triple quantum dot. We adopted the same pulse sequence used in early work in GaAs [JPT05]. Modifications are done based on system difference. We use Tektronics arbitrary waveform generator model 520 for all the pulses. For the experiment we did in Chapter 7, the output channel 1 of AWG520 is connected to depletion gate R while channel 2 to gate L. FIG. 7.4 illustrates the triangle pulse sequence. Following script describe how we generate triangle pulse.

```
function AWG_Triangle(t1,t2,Mx,My,Px,Py,Sx,Sy,clockrate,rep_rate,folder,FilePrefix,serie
%% generate triangle pulse for detectinig spin blockade;
%% t1 is the time spent for initialization at point P;\\ t2 is the time spent for loadin
%% configure pulse parameters  %%
   a1=33/2;  % attenuation on CH2
   b1=33/2;
       N_T2=1;

ch2p=(Px-Mx)*a1;
ch2s=(Sx-Mx)*b1;
ch1p=(Py-My)*a1;
ch1s=(Sy-My)*b1;
%% Save pulse parameters %%
```

```
filenote=strcat(folder,FilePrefix,'_','note','.txt');
fid = fopen(filenote, 'wt');
t_1=num2str(t1);
t_2=num2str(t2);
clockrate1=int2str(clockrate*1e-6);
rep_rate1=int2str(rep_rate*1e-3);
clock_rate=strcat('ClockRate is ',clockrate1,'MHz;');
Rep_rate=strcat('Rep_rate is ', rep_rate1,'KHz;');
t_P=strcat('Time for initialization is', t_1);
t_S=strcat('Time at 1,1 is',t_2);
Series=num2str(series);
SSeries=strcat('Data points are based on Serie',Series);
%%record coordinates
MX=num2str(Mx);
MY=num2str(My);
PX=num2str(Px);
PY=num2str(Py);
SX=num2str(Sx);
SY=num2str(Sy);

fprintf(fid,SSeries);
fprintf(fid, '\n');
M=strcat('M', '(',MX,',' ,MY,')',';');
S=strcat('S', '(',SX, ',',SY,')',';');
P=strcat('P', '(',PX,',', PY,')',';');

fprintf(fid, clock_rate);
fprintf(fid, '\n');
```

```
fprintf(fid, Rep_rate);
fprintf(fid, '\n');

fprintf(fid,  M);
fprintf(fid, '\n');
fprintf(fid,  P);
fprintf(fid, '\n');
fprintf(fid, S);

fprintf(fid, '\n');
fprintf(fid,  t_P);
fprintf(fid, '\n');
fprintf(fid,  t_S);
fprintf(fid, '\n');
fclose(fid);
%%  generate file for CH2 and CH1 for AWG



for i=1:N_T1;
    T1Num=fileNamenumber(i);
    T_1(N_T1)=t1;
    for j=1:N_T2;
    T2Num=fileNamenumber(j);
    T_2(N_T2)=t2;

    file1=strcat(folder,FilePrefix,'_CH2','_',T1Num,'_',T2Num,'.wfm');
    file2=strcat(folder,FilePrefix,'_CH1','_',T1Num,'_',T2Num,'.wfm');
    voltage1=voltage_awg_triangle(T_1(i),T_2(j),ch2p,ch2s,clockrate,rep_rate,file1);
```

```
    write_wfm(voltage1,file1,clockrate*1e-9)  % generate waveform for ch2,AUX6;
    voltage2=voltage_awg_triangle(T_1(i),T_2(j),ch1p,ch1s,clockrate,rep_rate,file2);
    write_wfm(voltage2,file2,clockrate*1e-9)  % generate waveform for ch1, AUX1;

    end;
end;
%%%%%%%%%%%%%%%%%%%%%%%%%%%%%%%%%%
function voltage=voltage_awg_triangle(t1,t2,v1,v2,clockrate,freq,FileName)
%% generate voltage vector
rem(1/freq,1/clockrate);
if rem(1/freq,1/clockrate)~=0
   c=rem(1/freq,1/clockrate);
    clockrate=(1/freq-c)*freq*clockrate;
end;
    N=clockrate/freq;
    N1=round(t1*clockrate);
    N2=round((t2+t1)*clockrate);

        voltage(1:N1)=v1;
        voltage(N1+1:N2)=v2;
        voltage(N2+1:N)=0;
        voltage1=voltage;
    fid = fopen(FileName, 'w');
    fprintf(fid, '%6.2f %12.8f\n', voltage1);
    fclose(fid);

%%%%%%%%%%%%%%%%%%%%%%%%%%%%%%%%%%
function write_wfm(voltage, file, freq, marker)
```

```
% write voltage vector 'voltage' to binary file 'file' in AGW wfm format
% Ref: AWG610_Programmer_Mannual
%                      Page 2-130 : Data Transfer
%                                 -> About Waveform and Pattern Files
% $Id: write_wfm.m,v 1.6 2012/03/07 18:55:45 aday Exp $

char_CR = 13; % character <CR>
char_LF = 10; % character <LF>
char_number = 35; % character #

if ~exist('voltage', 'var')
    return;
end

if ~exist('freq', 'var')
    freq = 2.6;
end

if ~exist('file', 'var')
    file = 'test';
end

length_v = length(voltage);
length_lv = length(num2str(length_v*5));

if ~exist('marker', 'var')
    marker = zeros(length_v, 2);
end
```

```
fid = fopen(file, ’w’);

% write <head> -- ’MAGIC 1000<CR><LF>#’
fwrite(fid, ’MAGIC 1000’, ’uchar’);
fwrite(fid, [char_CR char_LF char_number], ’uint8’);

% write data information -- <Number_Digits><Number_Bytes>
fwrite(fid, num2str(length_lv), ’uchar’);
fwrite(fid, num2str(length_v*5), ’uchar’);

% write <Data(i)><Marker(i,1)><Marker(i,2)> (4+1/2+1/2 bytes)
for i = 1:length_v
    fwrite(fid, voltage(i), ’real*4’);
    fwrite(fid, marker(i, 1)+marker(i, 2)*2, ’uint8’);
end

% write <trailer> -- ’CLOCK<freq><CR><LF>’
fwrite(fid, num2str(freq*1e9, ’CLOCK%.10E’), ’uchar’);
fwrite(fid, [char_CR char_LF], ’uint8’);

fclose(fid);
end
```

C.2 Comsol simulation

To obtain the electrostatic field distribution of a triple quantum dot shown in Chapter 2, we loaded the actual CAD file to the comsol program. We set the dielectric constant to be that of SiO_2. We set gate BL, BR, TL, TR to be -2V while setting other gates to be -0.5V. The field distribution is the calculation result on the surface of SiO_2. The actual field strength at the interface of Si/SiO_2 would be much smaller depending on the thickness of SiO_2. Notherless the general conclusion of three potential minima would not change.

C.3 Hubbard model

For the hubbard model calculation of double dot, the block diagonalization of the 16×16 matrix can be referred to this online tutorial: http://nerdwisdom.com/tutorials/the-hubbard-model/.

References

[AOT99] I. Amlani, A. O. Orlov, G. Toth, G. H. Bernstein, C. S. Lent, and G. L. Snider. "Digital logic gate using quantum-dot cellular automata." *Science*, **284**:289, 1999.

[BCJ99] G. Brennen, C. Caves, P. Jessen, and I. Deutsch. "Quantum logic gates in optical lattices." *Phys. Rev. Lett.*, **82**:1060–1063, 1999.

[BcR12] S. Blanvillain, J. I. colless, D. J. Reilly, H. Lu, and A. C. Gossard. "Suppressing on chip electromagnetic crosstalk for spin qubit device." *J. Appl. Phys.*, **112**:064315, 2012.

[BEC11] M. G. Borselli, K. Eng, E. T. Croke, B. M. Maune, B. Huang, R. S. Ross, A. A. Kiselev, P. W. Deelman, I. Alvarado-Rodriguez, A. E. Schmitz, M. Sokolich, K. S. Holabird, T. M. Hazard, M. F. Gyure, and A. T. Hunter. "Pauli spin blockade in undoped Si/SiGe two electron double quantum dots." *Appl. Phys. Lett*, **99**:063109, 2011.

[BGG13] M. Busl, G. Granger, L. Gaudreau, R. Sanchez, A. Kam, M. Pioro-Ladriere, S. A. Studenikin, P. Zawadzki, Z. R. Wasilewski, A. S. Sachrajda, and G. Platero. "Biopolar spin blockade and coherent state superpositions in a triple quantum dot." *Nature. Nanotechnology*, **8**:261–265, 2013.

[CGK98] I. Chuang, N. Gershenfld, and M. Kubinec. "Experimental Implemenation of Fast Quantum Searching." *Phys. Rev. Lett.*, **80**:3408–3411, 1998.

[CHS09] D. Culcer, X. Hu, and S. Das Sarma. "Dephasing of Si spin quits due to charge noise." *Appl. Phys. Lett*, **05**:073102, 2009.

[CLS04] J. Chiaverini, D. Leifried, T. Schaetz, M. Barrett, R. Blakestad, J. Britton, W. Itano, J. Jost, E. Knill, and C. Langer. "Realization of quantum error correction." *Nature*, **432**:602–605, 2004.

[CR12] J. I. Colless and D. J. Reilly. "Cryogenic high-frequency readout and control platform for spin qubits." *Rev. Sci. Instrum.*, **83**:023902, 2012.

[CZ95] J. Cirac and P. Zoller. "Quantum Computations with Cold Trapped ions." *Phys. Rev. Lett.*, **74**:4091–4094, 1995.

[DBK00] D. P. DiVincenzo, D. Bacon, J. Kempe, G. Burkard, and K. B. Whaley. "Universal quantum computation with the exchange interaction." *Nature*, **408**:339, 2000.

[DLJ04] L. Dicarlo, H. J. Lynch, A. C. Johnson, L. I. Childress, K. Crockett, C. M. Marcus, M. P. Hanson, and A. C. Gossard. "Differential charge sensing and charge delocalization in a tunable double quantum dot." *Phys. Rev. Lett.*, **92**:226801, 2004.

[EHB] J. M. Elzerman, R. Hanson, L. H. Willems van Bereven, B. Witkamp, L. M. K. Vandersypen, and L. P. Kowenhoven.

[Fey82] Richard P. Feynman. "Simulating physics with computers." *Int. J. Thero. Phys*, **21**:467–488, 1982.

[FGB06] T. Ferrus, R. George, C. H. W. Barnes, N. Lumpkin, D. J. Paul, and M. Pepper. "Evidence for multiple impurity bands in sodium-doped silicon MOSFETs." *Appl. Phys. Lett*, **73**:041304(R), 2006.

[GGK10] G. Granger, L. Gaudreau, A. Kam, M. Pioro-Ladriere, S. A. Studenikin, Z. R. Wasilewski, P. Zawadzki, and A. S. Sachrajda. "The 3D transport diagram of a triple quantum dot." *Phys. Rev. B*, **82**:075304, 2010.

[GGK12] L. Gaudreau, G. Granger, A. Kam, G. C. Aers, S. A. Studenikin, P. Zawadzki, M. Pioro-Ladriere, Z. R. Wasilewski, and A. S. Sachrajda. "Coherent control of three-spin states in a triple quanutm dot." *Nat. Phys.*, **8**:54–58, 2012.

[GKG09] L. Gaudreau, A. Kam, G. Granger, S. A. Studenikin, P. Zawadzki, and A. S. Sachrajda. "A tunable few electron triple quantum dot." *Appl. Phys. Lett*, **95**:193101, 2009.

[GSS06] L. Gaudreau, S. Studenikin, A. Sachrajda, P. Zawadzki, A. Kam, J. Lapointe, M. Korkusinski, and P. Hawrylak. "Stability diagram of a few electron triple dot." *Phys. Rev. Lett.*, **97**:036807, 2006.

[Hah50] E. L. Hahn. "Spin echoes." *Phys. Rev.*, **80**:580, 1950.

[HBV05] R. Hanson, L. H. W. van Beveren, I. T. Vink, J. M. Elzerman, W. J. M. Naber, F. H. L. Koppens, L. P. Kouwemhoven, and L. M. K. Vandersypen. "Single-shot readout of electron spin states in a quantum dot using spin dependent tunnel rates." *Phys. Rev. Lett.*, **94**(19), 2005.

[HFC03] T. Hayashi, T. Fujisawa, H. D. Cheong, Y. H. Jeong, and Y. Hirayama. "Coherent manipulation of electronic states in a double quantum dot." *Phys. Rev. Lett.*, **91**(22):226804, 2003.

[HHR05] H. Haffner, W. Hansel, C. Roos, J. Benhelm, D. Chek al Kar, M. Chwalla, T. Korber, U. Rapol, M. Riebe, and P. Schmidt. "Scalable multiparticle entanglement of trapped ions." *Nature*, **438**:643–646, 2005.

[HK05] P. Hawrylak and M. Korkusinski. "Voltage-controlled coded qubit based on electron spin." *Solid State Commun*, **136**:508, 2005.

[HMT10] D. Harbusch, S. Manus, H. P. Tranitz, W. Wegscheider, and S. Ludwig. "Radio frequency pulsed-gate charge spectroscopy on coupled quantum dots." *Phys. Rev. B*, **82**:195310, 2010.

[HOS] W. Hensinger, S. Olmschenk, D. Stick, D. Hucul, M. Yeo, M. Acton, L. Deslauriers, C. Montoe, and J. Rabchuk.

[Hou12] M. G. House. *Lateral quantum dots for quantum information processing.* PhD thesis, University of California, Los angeles, June 2012.

[HPX11] M. G. House, H. Pan, M. Xiao, and H. W. Jiang. "Non-equilibrium charge stability diagrams of a silicon double quantum dot." *Appl. Phys. Lett*, **99**:112116, 2011.

[HSS] X. Hu, R. de Sousa, and S. Das Sarma. "Decoherence and dephasing in spin-based solid state quantum computers." *arXiv.org/cond-mat/0108339.*

[HST05] T. Hatano, M. Stopa, and S. Tarucha. "Single-Electron delocalization in hybrid vertical lateral double quantum dots." *Science*, **309**:268, 2005.

[IAB99] A. Imamoglu, D. D. Awschalom, G. Burkard, D. P. DiVicenzo, D. Loss, M. Sherwin, and A. Small. "Quantum information processing using quantum dot spins and cavity QED." *Phys. Rev. Lett.*, **83**:4204–4207, 1999.

[JGP04] F. Jelezko, T. Gaebel, I. Popa, A. Gruber, and J. Wrachtrup. "Observation of coherent oscillations in a single electron spin." *Phys. Rev. Lett.*, **92**:076401, 2004.

[JPM05] A. C. Johnson, J. R. Petta, C. M. Marcus, M. P. Hanson, and A. C. Gossard. "Singlet-triplet spin blockade and charge sensing in a few-electron double quantum dot." *Phys. Rev. B*, **72**:165308, 2005.

[JPT05] A. C. Johnson, J. R. Petta, J. M .Taylor, A. Yacoby, M. D. Lukin, C. M. Marcus, M. P. Hanson, and A. C. Gossard. "Triplet-singlet spin relaxation via nuclei in a double quantum dot." *Nature*, **435**:925, 2005.

[Kan98] B. E. Kane. "A silicon-based nulcear spin quantum computer." *Nature*, **393**:133, 1998.

[KBT06] F. H. L. Koppens, C. Buizert, K. J. Tielrooij, I. T. Vink, K. C. Nowack, T. Meunier, L. P. Kowenhoven, and L. M. K. Vandersypen. "Driven coherent oscillations of a single electron spin in a quantum dot." *Nature*, **442**:766–771, 2006.

[KFE05] F. H. L. Koppens, J. A. Folk, J. M. Elzerman, R. Hanson, L. H. Willems van Beveren, I. T. Vink, H. P. Tranitz, W. Wegscheider, L. P. Kowenhoven, and L. M. K. Vandersypen. "Control and detection of singlet triplet mixing in a random nuclear field." *Science*, **309**:1346, 2005.

[KGH07] M. Korkusinski, I. P. Gimenez, P. Hawrylak, L. Gaudreau, S. A. Studenikin, and A. S. Sachrajda. "Topological hunds rules and the electronic properties of a triple lateral quantum dot." *Phys. Rev. B*, **75**:115301, 2007.

[KLM] E. Knill, R. Laflamme, and G. Milburnm. "A scheme for efficient quantum computation with linear optics." *Nature*.

[KNV08] F. H. L. Koppens, K. C. Nowack, and L. M. K. Vandersypen. "Spin echo of a single electron spin in a quantum dot." *Phys. Rev. Lett.*, **100**:236802, 2008.

[Kop08] F. H. L. Koppens. *Coherent and control of a single electron spin in a quantum dot.* PhD thesis, Technische Universiteit Delft, October 2008.

[Lad12] T. D. Ladd. "Hyperfine induced decay in triple quantum dots." *Phys. Rev. B*, **86**:161409, 2012.

[LD98] D. Loss and D. P. DiVincenzo. "Quantum computation with quantum dots." *Phys. Rev. A*, **57**:120, 1998.

[Lev02] J. Levy. "Universal quantum computation with spin 1/2 pairs and heisenberg exchange." *Phys. Rev. Lett.*, **89**(14):147902, 2002.

[LLY11] N. S. Lai, W. H. Lim, C. H. Yang, F. A. Zwanenburg, W. A. Coish, F. Qassemi, A. Morello, and A. S. Dzurak. "Pauli Spin Blockade in a highly tunable silicon double quantum dot." *Scientific Reports*, 2011.

[LTD10] E. A. Laird, J. M. Taylor, D. P. DiVincenzo, C. M. Marcus, M. P. Hanson, , and A. C. Gossard. "Coherent spin manipulation in an exchange-only qubit." *Phys. Rev. B*, **82**:075403, 2010.

[LZH09] W. H. Lim, F. A. Zwanenburg, H. Huebl, M. Mottonen, K. W. Chan, A. Mrello, and A. S. Dzurak. "Observation of the single-electron regime in a highly tunable silicon quantum dot." *Appl. Phys. Lett*, **95**, 2009.

[MBH12] B. M. Maune, M. G. Borselli, B. Huang, T. D. Ladd, P. W. Deelman, K. S. Holabird, A. A. Kiselev, I. Alvarado-Rodriguez, R. S. Ross, A. E. Schmitz, M. Sokolich, C. A. Watson, M. F. Gyure, and A. T. Hunter. "Coherent singlet-triplet oscillations in a silicon-based double quantum dot." *Nature*, **481**:344–347, 2012.

[MBT13a] J. Medford, J. Beil, J. M. Taylor, S. D. Bartlett, A. C. Doherty, E. I. Rashba, D. P. DiVincenzo, H. Lu, A. C. Gossard, and C. M. Marcus. "Self-consistent measurement and state tomography if an exchange-only spin qubit." *arXiv.org/cond-mat/1302.1933*, 2013.

[MBT13b] J. Medford, J. Beil, J. M. Taylor, H. Lu, A. C. Gossard, and C. M. Marcus. "Quantum-Dot-Based resonant exchange qubit." *Phys. Rev. Lett.*, **111**:050501, 2013.

[MD] S. Mehl and D. P. DiVicenzo. “Noise-Protected gate for six electron double dot qubit.” *arXiv.org/cond-mat/1305.0749*.

[MOL99] J. Mooij, T. Orlando, L. Levitov, L. Tian, C. Van del Wall, and S. Lloyd. “Joshphson Persistent- Current Qubit.” *Science*, **285**:1036–1039, 1999.

[MPZ] A. Morello, J. J. Pla, F. A. Zwanenburg, K. W. Chan, H. Huebl, M. Mottonen, C. D. Nugroho, C. Yang, J. A. van Donkelaar, A. D. C. Alves, D. N. JAmieson, C. C. Escott, L. C. L. Hollenberg, R. G. Clark, and A. S. Dzurak. “Single-shot readout of an electron spin in silicon.” *Nature*.

[NKL98] M. A. Neilsen, E. Knill, and R. Laflamme. “Complete quantum teleportation using nuclear magnetic resonance.” *Nature*, **396**:52, 1998.

[NSL11] K. C. Nowack, M. Shafiei, M Laforest, G. Prawiroatmodjo, L. R. Schreiber, C. Reichl, W. Wegscheider, and L. M. K. Vandersypen. “single-shot correlations and two-qubit gate of solid state spins.” *Science*, **333**:1269–1272, 2011.

[OPT10] T. Obata, M. Pioro-Ladriere, Y. Tokura, Y. S. Shin, T. Kubo, K. Yoshida, T. Taniyama, and S. Tarucha. “Coherent manipulation of individual electron spin in a double quantum dot integrated with a micromagnet.” *Phys. Rev. B*, **81**(8):085317, 2010.

[PGK02] V. M. Pudalov, M. E. Gershenson, and H. Kojima. “Memory effects in electron transport in Si inversion layers in the dilute regime: individuality versus universality.” *arXiv.org/cond-mat/0201001*, 2002.

[PJM04] J. R. Petta, A. C. Johnson, C. M. Marcus, M. P. Hanson, and A. C. Gossard. “Manipulation of a single charge in a double quantum dot.” *Phys. Rev. Lett.*, **93**:186802, 2004.

[PJT05] J. R. Petta, A. C. Johnson, J. M. Taylor, E. A. Laird, A. Yacoby, M. D. Lukin, C. M. Marcus, M. P. Hanson, and A. C. Gossard. “Coherent manipulation of coupled electron spins in semiconductor quantum dots.” *Science*, **309**(5744):2180–2184, 2005.

[PLG10] J. R. Petta, H. Lu, and A. C. Gossard. “A coherent beam splitter for electronic spin states.” *Science*, **327**:669, 2010.

[POT07] M. Pioro-Ladriere, T. Obata, Y. Tokura, T. Kubo, and S. Tarucha. “Micromagnets for coherent control of spin-charge qubit in lateral quantum dots.” *Appl. Phys. Lett*, **90**(2):024105, 2007.

[POT08] M. Pioro-Ladriere, T. Obata, Y. Tokura, Y. S. shin, K. Yoshiba T. Kubo, T. Taniyama, and S. Tarucha. “Electrically driven single electron spin resonance in a slanting zeeman field.” *Nat. Phys.*, **4**:776, 2008.

[PPL10] K. D. Petersson, J. R. Petta, H. Lu, and A. C. Gossard. “Quantum coherence in a one-electron semiconductor charge qubit.” *Phys. Rev. Lett.*, **105**:246804, 2010.

[SGG07] D. Schroer, A. D. Greentree, L. Gaudreau, K. Eberl, L. C. L. Hollenberg, J. P. Kothaus, and S. Ludwig. “Electrostatically defined serial triple quantum dot charged with few electrons.” *Phys. Rev. B*, **76**:075306, 2007.

[Sho96] P. W. Shor. “Fault-tolerant quantum computation.” *Proceedings of 37th annual symposium in foundations of computer science, IEEE PRess*, pp. 56–67, 1996.

[SJP12] M. D. Schroer, M. Jung, K. D. Petersson, and J. R. Petta. “Radio frequency charge parity meter.” *Phys. Rev. Lett.*, **109**:166804, 2012.

[SS05] V. W. Scarola and S. Das Sarma. “Exchange gate in solid-state spin-quantum computation: the applicability of the Heisenberg.” *Phys. Rev. A*, **71**:032340, 2005.

[SSW13] Zhan Shi, C. B. Simmons, Daniel R. Ward, J. R. Prance, R. T. Mohr, Teck Seng Koh, ohn King Gamble, Xian Wu, D. E. Savage, M. G. Lagally, Mark Friesen, S. N. Coppersmith, and M. A. Eriksson. “Coherent quantm oscillations and echo measurements of a Si charge qubit.” *Phys. Rev. B*, **88**:075416, 2013.

[STR09] C. B. Simmons, M. Thalakulam, B. M. Rosemeyer, B. J. Van Bael, E. K. Sackmann, D. E. Savage, M. G. Lagally, R. Joynt, M. Friesen, S. N. Coppersmith, and M. A. Eriksson. “Charge sensing and controllable tunnel coupling in a Si/SiGe double quantum dot.” *Nano Lett*, **9**(9):3234–3238, 2009.

[SWY11] S. Das Sarma, X. Wang, and S. Yang. “Hubbard model description of silicon spin qubits: charge stablity diagram and tunnel coupling in si double quantum dots.” *Phys. Rev. B*, **83**:235314, 2011.

[THL95] Q. A. Turchette, C. J. Hood, W. Lange, H. Mabuchi, and H. J. Kimble. “Measurement of conditional base shifts for quantum logic.” *Phys. Rev. Lett.*, **75**:4710–4713, 1995.

[TL01] G. Toth and C. S. Lent. “Quantum computing with quantum-dot cellular automata.” *Phys. Rev. A*, **63**:052315, 2001.

[TN] Yuan Taur and Tak H. Ning. *Fundamentals of Modern VLSI Devices.* Cambridge University Press.

[TNY10] L. A. Tracy, E. P. Norberg, R. W. Young, C. Borras Pinilla, H. L. Stalford, G. A. Teneyck, K. Eng, K. D. Childs, J. Stevens, M. P. Lilly, M. A. Eriksson, and M. S. Carroll. “Double quantum dot with tunable coupling in an enhancment-mode silicon metal-oxide semiconductor device with lateral geometry.” *Appl. Phys. Lett*, **97**:192110, 2010.

[TPJ07] J. M. Taylor, J. R. Petta, A. C. Johnson, A. Yacoby, C. M. Marcus, and M. D. Lukin. "Relaxation, dephasing and quantum control of electron spins in double quantum dots." *Phys. Rev. B*, **76**:035315, 2007.

[TPO10] T. Takakura, M. Pioro-Ladriere, T. Obata, Y.-S.shin, R. Bruner, K. Yoshida, T. Taniyama, and S. Tarucha. "Triple quantum dot device designed for three spin qubits." *Appl. Phys. Lett*, **97**:212104, 2010.

[TSM13] J. M. Taylor, V. Srinivasa, and J. Medford. "Electrically protected resonant exchange qubits in triple quantum dots." *Phys. Rev. Lett.*, **111**:050502, 2013.

[VSB01] L. M. K. Vandersypen, M. Steffen, G. Breyta, C. Yannoni, M. H. Sherwood, and I. L. Chuang. "Experimental realization of Shor's quantum factoring algorithm using nuclear magnetic resonance." *Nature*, pp. 883–887, 2001.

[VYW00] R. Vrijen, E. Yblonovitch, K. Wang, H. W. Jiang, A. Balandin, V. Roychowdhury, T. Mor, and D. P. Divicenzo. "Electron-spin-resonance transistors for quantum computing in silicon-germanium heterostructures." *Phys. Rev. A*, **62**:012306, 2000.

[WFE03] W. G. van der Wiel, S. De Franceschi, J. E. Elzerman, T. Fujisawa, S. Tarucha, and L. P. Kowenhoven. "Electron transport through double quanutm dots." *Rev. Mod. Phys.*, **75**(1):1–22, 2003.

[XHJ10] M. Xiao, M. G. House, and H. W. Jiang. "Parallel spin filling and energy spectroscopy in few-electron Si metal-on-semiconductor-based quantum dots." *Appl. Phys. Lett*, **97**:032103, 2010.

[Xia04] M. Xiao. *Single electron spin measurements in submcron Si field effect transistors.* PhD thesis, University of California, Los Angeles, 2004.

[YWS11] S. Yang, X. Wang, and S. Das Sarma. "Generaic Hubbard model description of semiconductor quantum-dot spin qubits." *Phys. Rev. B*, **83**:161301(R), 2011.

[ZDM13] F. A. Zwanenburg, A. S. Dzurak, A. Morello, M. Y. Simmons, L. C. L. Hollenberg, G. Klimeck, S. Roggo, S. N. Coppersmith, , and M. A. Erricksson. "Silicon quantum electronics." *Rev. Mod. Phys.*, **85**:961–1019, 2013.